Micro/Nano Patterning on Solid Surface

a thesis submitted

in partial fulfillment of the requirements

for the degree of

Doctor of Philosophy

by

Mr. Kaniska Murmu

Department of Chemical Engineering

Indian Institute of Technology Guwahati

December 2022

C E R T I F I C A T E

It is certified that the works contained in this thesis entitled **"Micro/Nano Patterning on Solid Surface"**, by Mr. Kaniska Murmu, have been carried out under my supervision and have not been submitted as a thesis elsewhere for a Ph.D degree.

Thesis supervisor

Dr. Partho Sarathi Gooh Pattader
Associate Professor
Department of Chemical Engineering, Centre for Nanotechnology &
School of Health Sicences and Technology
Indian Institute of Technology Guwahati

December, 2022

ACKNOWLEDGEMENT

The journey undertaken for the completion of this thesis has been one of the most amazing experiences of my life, which would have been impossible without these people.

First and foremost, I would like to thank my thesis supervisor **Dr. Partho Sarathi Gooh Pattader** for giving me the opportunity to work in a very interesting area of research. I am very grateful to him for his continuous guidance, important advices and stimulating discussions. In spite of his busy schedule, he was always happy to dedicate his time to analyze the problems and give necessary suggestions for the betterment of my work. I am certain that the experience of working under his supervision will have far-reaching influences on my life. His devotion towards his work, his untiring zeal to achieve perfection, and his patience in guiding novice researchers, will always inspire me. I consider it an honor to have been guided by him. I wish to thank my doctoral committee members, **Prof. Tapas Kumar Mandal** and **Prof. Ashok Kumar Dasmahapatra** Department of Chemical Engineering, **Prof. Dobbidi Pamu** Department of Physics, for their valuable suggestions and efforts during my thesis work. I would like to thank the panel member of doctoral viva voce, **Prof. Nageswara Rao Peela** Department of Chemical Engineering, and **Prof. Akshai Kumar Alape Seetharam** Department of Chemistry, for their valuable suggestions. I wish to thank also to the examiners of my thesis, **Prof. Giridhar U Kulkarni**, Jawaharlal Nehru Centre for Advanced Scientific Research, Bangalore, India, and **Prof. Faquian Yang**, University of Kentucky, United States, for reviewing my thesis and also for their valuable suggestions.

My sincere thanks to the senior lab-mates, **Dr. Pritam Roy**, **Dr. Ankur Pandey and Dr. Sunil Kumar Singh,** for their unhesitating assistance and continuous encouragement throughout my PhD tenure. I also wish to extend my gratitude to lab-mates, **Miss. Prerona Gogoi and Mr. Aniruddha Deb**, for their support in experiments and preparation of my thesis. Also, I am particularly grateful to **Mr. Krishna Pradeep Burgula** for his support in experiments.

I am also thankful to all the members of our research group, **Dr. Nayanmani Das, Dr. Dhrubajyoti Roy, Dr. Abir Ghosh, Dr. Mitradip Bhattacharjee, Dr. Nilanjan Mandal, Dr. Bolleddu Ravi, Dr. Tamanna Bhuyan, Dr. Nirmal Roy, Dr. Rupam Sinha, Dr. Seim Timung, Dr. Surjendu Maity, Dr. Shirsendu Mitra, Mr. Ayush Sharma, Ms. Ashita**

Gupta, Ms. Vaibhavi Bindlish, Mr. Chintak K. Parashar, Mr. Saikat Biswas, Ms. Mitali Basak, Mr. Vinod Babasaheb Vanarse, Mr. Jiwajyoti Mahanta, Mr. Shrikant Kashyap, Mr. Purushotam Shivshakti Mahan, Mr. Ravula Rajasekhar, Dr. Siddharth Thakur, Ms. Tanusree Ghoshal, Mr. Nayanjyoti Kakati and last but not the least **Mr. Sagnik Midda.**

I cannot forget to thank my friends and colleagues **Dr. Awadh Kishor Kumar, Dr. Pankaj Jha, Dr. Dharmalingam K, Dr. Vimal Kumar Singh Yadav, Dr. Prince Kumar Baranwal, Dr. Barnali Bhui, Mr. Pradeep Sahu, Mr. Sekhar Jyoti Pathak, Dr. Bitang Kwrung Tripura, Mr. Nabendu Paul, Mr. Anweshan Ghosh, Dr. Piyal Mondal, Mrs. Nilanjana Chakraborty, Mr. Nirmal Mallick, Mr. Trilokpati Tribedi, Mr. Ponnala Rambabu,** and last but not the least **Mrs. Anushikha Roy** for their role in making my stay at IIT Guwahati memorable.

My special thanks to all the **faculties** and **staff members** of **Department of Chemical Engineering, Centre for Nanotechnology**, and **Central Instruments Facility**, **IIT Guwahati**, for their supports and co-operations during all this time. I also acknowledge the support from the Analytical Laboratory in Chemical Engineering, Centre for Nanotechnology, and Central Instruments Facility, IIT Guwahati for characterization facilities.

Above all, I wish to thank my **parents, elder sister, in-laws** and **family members** for their love and support throughout everything, as always. Most importantly, I would like to express gratitude to my wife, **Mrs. Sarmistha Chakraborty,** for her much-needed support.

Kaniska Murmu.

KANISKA MURMU

This thesis is dedicated to my family

For their endless love, support and encouragement

SYNOPSIS

Micro/Nano Patterning on Solid Surface

Chapter 1: Introduction

Miniaturization of past technology is the key of revolution of modern technology, and this is one of the reasons that the researchers are driven to this field for more than last three decades. The greatest example of this outcome is modern computers and smart phones which are being evolved day by day to make the life very much easier. Micro/nano featured ordered patterning on solid surface plays the primary role in this regard, where the surface to volume ratio is the key factor. Above these all creations, nature has inspired us from the very beginning by expressing the benefits for our human society of these micro/nano featured patterned surfaces for example, superhydrophobic surface or self-cleaning surface of Lotus leaf, stack of micro-lenses of insects, water-harvesting micro patterned surface of insects and plants, structural color of Peacock feathers, etc. Thus, we have also followed the nature by mimicking the structures for our own various purposes like self-cleaning surfaces, smart adhesives like gecko feet, anti-reflection coating, micro-lenses, structural colors, advanced storage devices, hydrophilic/hydrophobic surface, micro/nano perovskite structures for photovoltaic cell, fuel cell, lithium-ion battery, sensors in various fields, etc.

There are mainly two categories of fabrication method, first is top-down approach and second is bottom-up approach. The top-down approach includes photolithography, e-beam lithography, nanoimprinting lithography, capillary force lithography etc. and bottom-up approach implicates dip-coating lithography, self-assembled deposition, physico-chemical temple guided or without guided deposition, electric field induced self-assembly, etc. Among all of the above, photolithography and e-beam lithography is popular and mainstay

conventional lithography processes for fabricating micro/nano pattern on a solid surface. But, due to the high cost and restricted to their resolution, other methods are in focus now. Among them, self-assemble method is capable of fabricating such type of meso to nanoscale structures like, self-assembled micro/nano particles as a hexagonal pattern, complex micro/nano structures, perovskite structures, structure with large area containing multiple polymers, formation of multilayers of multiple polymers in a single entity, etc., which are comparatively difficult to fabricate by conventional lithography processes.

After having the above discussions, this thesis offers a broad view over self-assemble method and deposited morphological features of polymers from a dynamics of contact line of a clear polymer solution. And also, it offers the benefits of the deposited features to the application point of view. The third chapter represents regarding self-assembled deposition of homopolymers by dynamic contact line lithography (DCLL) and a brief study about the fabricated morphologies. The fourth chapter presents the formation of Janus micro-threads and Janus micro/nanodroplets from a blend polymer solution of PS/PMMA by DCLL method. Fifth chapter, represents cost effective solvent vapor induced patterning of in-situ PS/PMMA blend polymer after combining of two methods, spin coating and DCLL. Sixth chapter, demonstrates that the DCLL can be used to fabricate energy harvesting device where, polyvinylidene fluoride (PVDF) is treated by comparatively lower magnitude of electric field during contact line deposition (DCLL) in order to fabricate β-phase crystalline morphology.

Chapter 2: Literature Review

In chapter 2, a brief discussion about literature review is reported in this thesis.

Chapter 3: Dynamic Contact Line Lithography: Template-less Complex Meso-Patterning with Polystyrene and Poly(methyl methacrylate)

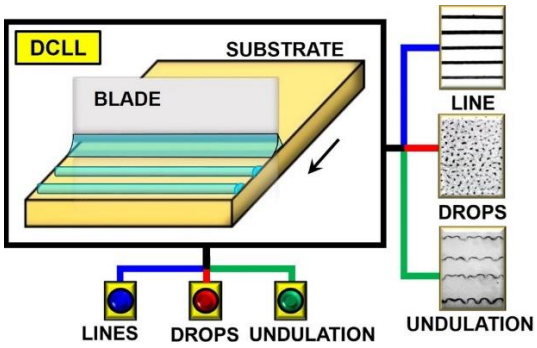

Figure 1. depicts the schematic diagram of dynamic contact line lithography and its accessories by which mainly three types of deposited morphologies are observed of polymer, like straight line, drops, and undulated lines. The arrow (in black) represents the direction of stage movement.

The objective of this work is to study and demonstrate the versatility of dynamic contact line lithography (DCLL) in the area of polymer patterning on a solid surface into the range from meso to nano-scale. The DCLL is performed by a customized arrangement where the meniscus of solution is mainly dragged by a capillary force. A priori, the solid substrate is placed on a customized unidirectional stage and simultaneously a stainless-steel blade is placed vertically above the substrate by keeping a narrow gap of ~ 200 µm. The polymer solution of 20 µl is dispensed into the gap and it holds the solution perfectly due to the capillary force. Once the stage starts to move at a certain velocity, the contact line also moves to the opposite direction at a same magnitude and simultaneously, the meniscus deposits the phase separated polymer morphology at the contact line. A range of various types of deposited morphologies are demonstrated here and its direct effect to the modification of overall surface energy, which is associated with the hydrophilicity and hydrophobicity of the substrate, is also demonstrated.

Summary:

The beauty of this work is that the fabrication method (DCLL) is generic in nature. Any polymer solution can be used to fabricate micro/nano feature on solid surface. The deposited morphologies comprise with mainly straight lines, undulated lines and micro/nanodrops. Here, concentration of the homopolymer and contact line velocity are the only variable parameters.

Therefore, depending upon the various combinations of these two parameters a broad range of deposited morphologies are demonstrated of polystyrene (PS) and poly(methyl methacrylate) (PMMA) separately. Two phase-diagrams are also reported separately of both polymers and, this acts as a guidance to fabricate a particular pattern on the Si substrate. We have also shown that how deposited morphologies with different wavelengths change the overall surface roughness, which complements to the change of water contact angle on the Si substrate. A complex structured pattern is also shown here, where two different polymers (here, PS and PMMA) are deposited separately on a single substrate.

Chapter 4: Janus Micro-thread to Micro-nanodroplets Using Dynamic Contact Line Lithography

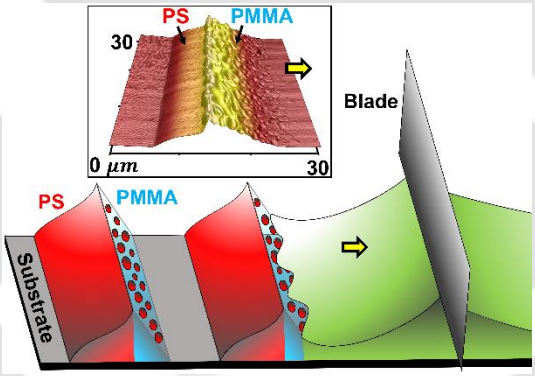

Figure 2. depicts the schematic representation of deposited Janus micro thread from a PS/PMMA blend polymer solution by DCLL method. The arrow (in yellow) represents the direction of the contact line.

In this chapter, we have taken a further step using DCLL method as a fabrication tool. Here, we have fabricated Janus micro-thread and Janus micro/nanodroplets, where two different components (PS/PMMA blend polymer) are deposited at once as a single entity on the Si substrate, from a solution of common solvent. The PS is deposited as smooth at the front side of the thread and PMMA is deposited as labyrinth-type at the rear side of the thread from a solution of toluene. Fabrication of micro-thread is accomplished by the help of the phase

diagram from chapter 1. We have also shown the effect after changing the ratio of the PS/PMMA blend polymer composition. And, this shows that the higher PS composition than the PMMA, leads to the random arrangement of the polymers into the structure. Where, higher PMMA composition shows prominent Janus micro-thread. These similar observations are also demonstrated in case of undulated micro-thread which are formed after reducing the overall blend polymer concentration and keeping the contact line velocity as constant. In case of micro/nano droplets, we have observed multiple arrangements of PS and PMMA, like Janus structure, formation of multilayers and core-shell morphology, with respect to the different PS/PMMA composition. These micro/nano droplets are formed by reducing further of overall blend polymer concentration.

Summary:

Here, the phase separated Janus morphology is developed due to the different solubility of the polymers into the common solvent. So, the more soluble component is likely dragged faster towards the contact line to replenish due to the evaporative loss of the solvent. And, this deposits the polymer at the front side and less soluble polymer at the rear side of respective features. This phenomenon has been confirmed by other way around, where PMMA has been deposited to the front side and PS to the rear side of the deposited feature from a solution of ethyl acetate. Because, here PMMA is more soluble into ethyl acetate than PS.

Chapter 5: Solvent Assisted Dewetting of PMMA Thin Film and PS Micro-thread: Fabricated by Dynamic Contact Line Lithography

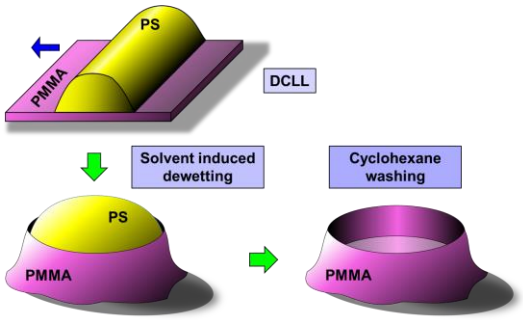

Figure 3. depicts the schematic flow diagram of solvent vapor induced dewetting of in-situ polymer blend to fabricate complex structure by using the combination of spin coating and DCLL method.

In this chapter, we have shown that the DCLL process can be compatible with other fabrication process like spin coating, to fabricate cost effective semi-ordered complex structures of two different polymers, PS and PMMA. Here, two polymers are introduced to each other separately. At first, PMMA is spin coated on a glass substrate and then PS micro-threads are deposited above PMMA thin film. Later, thermal and solvent vapor assisted dewetting are allowed to happen for 12 h. Different dewetted morphologies are demonstrated with respect to the medium of treatment. The thermal treatment allows to dewet faster of PMMA thin film as a random dewetted morphology and PS experiences the initial phase of dewetting within the given time span. Selective solvent vapor treatment only dewets the respective polymers. And, common solvent vapor treatment dewets both the polymers and arranges the features as a semi-ordered pattern, where PS micro-threads region exhibits an ordered dewetted meso/microdroplets and PMMA thin film region shows random dewetted microdroplets. These droplets comprise with both the polymers and this is confirmed after washing with a selective solvent.

Summary:

In conclusion, we can say that this is a new approach to fabricate semi-ordered complex structure by solvent vapor treatment combined with spin coating and DCLL methods. Here, in-situ blend polymer system during common solvent vapor treatment takes the advantage to form

the complex structure and the PS micro-threads act as structure-directing component during dewetting, to form the ordered complex structure. On the other hand, dewetting of selective polymer region by selective solvent vapor treatment, might be interested for particular applications also. Overall, this process is very cost effective to fabricate complex semi-ordered structures, rather than the any other conventional lithography process (i.e. photolithography, electron beam lithography) where they are limited to their operation, resolution and fabricated length-scale.

Chapter 6. Self-assembled PVDF Micro-thread with β-phase Crystallinity; Induced by Dynamic Contact Line Lithography Coupled with Electric Field

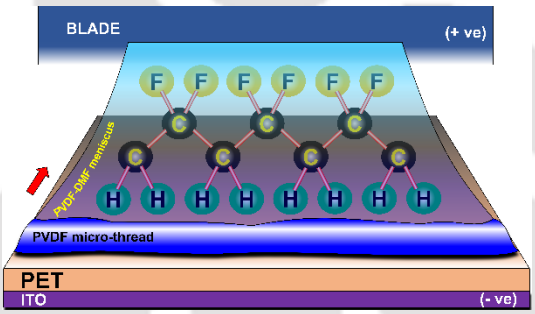

Figure 4. represents a schematic diagram of deposition process of PVDF from a moving contact line of PVDF-DMF solution in the presence of an applied voltage across the solution. The arrow represents the direction of moving contact line.

In this chapter, we have successfully demonstrated that DCLL method in presence of very less electric field can be used to deposit PVDF micro-threads with β-polymorph on a flexible surface like, ITO coated PET sheet. Here, PVDF micro-threads are deposited on the bare PET side as straight lines by the help of the phase diagram of PMMA of chapter 3. Though, the evaporation rate of DMF is much lower than the toluene or cyclohexane therefore, an external heat is provided to inhibit the evaporation rate of DMF close to toluene. The deposition process in presence of electric field might align the molecules of PVDF very easily in favour of β-phase crystallinity which shows better piezoelectric behaviour. With this vision, we have

maintained the gap in between stainless-steel blade and PET, as small as possible, $\sim 50-70$ μm and have varied the voltage across the solution from 0 V to 1000 V. The outcomes are satisfactory after achieving β-phase crystallinity where higher voltage, at 1000 V shows almost double amount of β-phase than α-phase. After depositing the micro-threads on PET sheet, the sample is used as the test sample for further characterization. A Multimeter is connected across the micro-threads to monitor the magnitude of the voltage against an applied stress on the PVDF micro-threads. A 500 V treated sample is used to demonstrate the above-mentioned experiment and it shows satisfactory result. We believe that the 200 V treated sample also is capable of showing some electrical potential against an applied stress.

Summary:

We have demonstrated a novel approach to fabricate PVDF micro-threads with β-phase crystalline structure by DCLL method when a very less electric field, ~ 7 V/μm, is applied across the solution. The process is not only cost effective as very less electric field intensity is required but also, it is an innovative way which can be applied to fabricate individual PVDF micro-thread for various field of applications like, sensor, energy harvester etc. The method also allows us to fabricate satellite PVDF micro/nanodrops with β-phase crystalline structure which might be beneficial in different applications.

Chapter 7: Summary and Future Scope

The Chapter 7 concludes with the thesis summary and a brief discussion on the future prospects of microfluidic reactor discussed in this thesis work.

List of Figures

List of Tables

Contents

Topic **Page No.**

Chapter 1

Introduction to Micro/nano Patterning

This page is left blank intentionally

1.1 The Canvas of Micro/nano Patterning

Miniaturized patterned structures find great importance in various fields of applications with specific purposes such as self-cleaning,[1] or frictionless surfaces,[2] anti-reflection coating on the lens,[3] photovoltaic applications,[4–6] sensors,[7,8] etc. Also, the development and innovations in modern technology and science are considerably influenced by the microfabrication technique. The first-ever, a miniaturized 2D hybrid integrated circuit with transistors was reported in 1952 by Jay W. Lathrop and James R. Nall, who were notably impressed by the application of photoresist.[9] Since then, different lithography processes have been introduced to microelectronic applications.

1.2 Micro/nano and Nature

With the vision of a better human society in the future, many inspirations are acquired from mother nature, and micro/nano-architecture is one of them. There are myriad examples of micro/nano-featured surfaces in nature for various requirements. A few of them are micro/nano-structured surfaces of lotus leaves for self-cleaning purpose,[1] micro/nano-hairy structures on gecko feet for climbing wall, [10,11] micro-lenses of insects,[12] hairy legs of water-strider for keeping them above water body,[13] structured back surface of dessert beetle to collect dew drops from the air,[14] and structural color of butterfly wings,[12] or peacock feather,[12] etc. In lotus leaf, the featured structures help the waterdrop to roll away by picking up the micro/nanoscopic dust particles from the surface. This well-known phenomenon was studied for the first time by Wilhelm Barthlott and Ehler in 1977. They termed this as the "Lotus effect". The feet of geckos have several specializations. On its feet, many hairy structures are made of β-keratine (protien), called setae. Every setae contains thousands of isosceles triangle-shaped structure, known as spatula.[15,16] These micro/nanoscopic hierarchy structured pattern provides Van der Waals forces between gecko feet and another surface that

helps them to walk almost on every wall. These few examples of the potential of micro/nano structured surfaces are the inspiration to modern science and technology. Researchers have also fabricated similar biomimetic micro/nano-structured surfaces for various applications like self-cleaning,[1] smart adhesive,[11,17] micro-lense arrays to improve the efficiency of LED,[18] optofluidics,[19] solar cell,[20] and biomedical applications,[21–24] etc.

1.3 Micro/nano Structure and Lithography

Lithography is very much crucial in the current times because it is an essential part of most of the device fabrication process. Lithography was invented by a Bavarian actor and playwright, Alois Senefelder, in 1796 in German. He duplicated his writing with greasy crayon on the slabs of limestones. Later, in 1826, Nicéphore Niépce invented the photographic process by using the world's first photoresist Bitumen Judea, a natural asphalt.[25] In 1940, Oskar developed positive a photoresist by diazonaphthoquinone, which worked as a negative manner.[26] Later, more photoresists were designed according to the purposes.

As time rolled down, different lithography processes were developed by researchers. Every lithography process has its limitations and advantages, which makes them unique. In terms of processing methods, lithography is categorized into two parts, first is the top-down approach, and the second is bottom-up approach. Top-down approaches are namely photolithography,[27–33] electron beam lithography (EBL/e-beam lithography),[34–39] and focused ion beam lithography,[40–45] etc. And, on the other hand, bottom-up approaches are stereolithography,[46–49] nano-imprint lithography,[50–56] self-assembly method,[57–60] dynamic contact line deposition,[18] dip pen nanolithography,[61–67] and electric field induced lithography,[68–71] etc.

1.3.1 Top-Down Approach

1.3.1.1 Photolithography

Photolithography is also known as optical lithography or UV lithography.[27–33] It is a process to fabricate or transfer micro/nano-geometric structures on a solid surface using a direct writing method or using a mask, treated under UV laser beam or light, respectively. Initially, the fabricated structures are made of photoresist (chemical substance), which is spin-coated as a thin film on the surface and then it is exposed under focused UV beam or UV light. Depending upon the nature of the photoresist, during the developing process, either the exposed region (in case of positive photoresist) or the unexposed area (in case of negative photoresist) dissolves into the developer, leaving only the micro/nano-architecture of the photoresist onto the solid surface. The resolution of the fabricated structure may be as less as 500 nm to 1 μm.

1.3.1.2 Electron Beam Lithography

In this method, highly accelerated (~ 30 kV) electrons are used to expose e-beam resist to fabricate a fine structure with a resolution of as low as ~ 5 nm to 10 nm.[34–39] Here, generally poly methyl methacrylate (PMMA) is used as both positive and negative tone e-beam resist. Other processes are similar like the photolithography process.

E-beam lithography and photolithography, both have excellent repeatability for a particular structure, making them as mainstay lithography processes in modern fabrication technology.

1.3.1.3 Focused Ion Beam Lithography

A focused ion beam (FIB) lithography is also used for patterning by direct-write method.[40–45] FIB is similar to photolithography and e-beam lithography; however, for patterning FIB mill a sample surface that is exposed to the high ion beam current. In FIB milling, a gallium (Ga) ion beam is primarily used to hit the sample surface and sputters away a small amount of material. At high current, the materials of the sample can be removed precisely so that the feature size of less than 1 μm is achievable.

1.3.2 Bottom-Up Approach

1.3.2.1 Stereolithography

The stereolithography method is an advanced 3D printing process to fabricate structure layer by layer.[46–49] The process continues with a focused laser beam on a free surface that polymerizes a photosensitive polymer solution into a solid structure. The resolution of features can go less than 1 μm.

1.3.2.2 Nano-imprint Lithography

This method was coined in 1996 by Prof. Stephen Chou, although hot thermoplastic embossing had been mentioned in the patent literature few years before.[50–56] In this method, the structures are directly imprinted on the polymer surface by applying pressure when thermal treatment is also subjected to the process. The fabricated structures on the polymer surface are the opposite replica of the primary structures, which makes this process facile to mimic any structure.

1.3.2.3 Dip Pen Nanolithography

Dip pen nanolithography involves a tip of an Atomic Force Microscopy (AFM) tip to deposit a variety of inks on a solid surface for fabricating patterns.[61–67] The working principle is associated with dipping the AFM tip into an ink droplet, where the ink molecules are transferred to the tip. Later, the AFM tip moves the ink molecules to the surface by contact mode. The feature resolution can be varied from μm to nm.

1.3.2.4 Electric Field Induced Lithography

Electric field induced lithography involves two electrodes separated by a very narrow distance, a few μm,[69,71] to nm,[71] and the substrate on which the micro/nano features are grown is placed between two electrodes.[68–71] The applied voltage across the electrodes creates

instability on a soft surface, which eventually rearranges the molecules of the soft material in a particular order. Sometimes, this method is also used to grow nanowires on the semiconductor surface.

1.3.2.5 Self-assembly

Self-assembly is a naturally occurred phenomenon, where colloid particles or dissolved polymer molecules self-arrange themselves and deposit on a surface during solvent evaporation.[57–60] Further, this process has been discussed later in detail.

1.3.2.5.1 Colloidal Lithography

Colloidal lithography is referred to that process, where a self-assembled, close-packed monolayer of micro/nanoparticles is deposited by natural evaporation of solvent on a surface.[72] This method was first used by Fischer and Zingsheim in 1981 to fabricate a mask for the deposition of platinum.[73] Soon after, this method was extended by Deckman and co-workers for large-area patterning. They termed it "natural lithography."[74–77]

1.4 Introduction to Self-assembly

The rapid development of nanotechnology since decades and an understanding of nature are empowering our lifestyle at every step. Fabrication of highly efficient micro-nano devices that help us not only to do the work efficiently but also in a sophisticated manner with less time consumption, reducing the overall operating cost. However, a long way to go for the best out of it concerning to fabrication process. There are several applications based on nanotechnology are currently in demand, like micro/nanopatterned surfaces, fabrication of reactors, micro-channels, miniaturization of instruments (MEMS, NEMS) etc. This work mainly, focuses on fabricating patterned surface with thin polymer film and its sensor-based application.

Two-dimensional ordered structures existing in nature have been discovered, and various intriguing surface properties have been widely evaluated. [78,79] Series of artificial patterned surfaces inspired by lotus leaves,[80] gecko feet,[10] insect compound eyes,[81] spider silks,[82–84] etc. have been successfully fabricated and used for self-cleaning, antifogging, anti-reflection, water-oil separation, and so on.[85–90] Highly ordered hierarchical structures from micro to nanoscale make the artificial patterned surfaces well inherited and integrated unique functionalities of the natural biological surfaces, such as controllable supra wetting, anisotropic wetting, oriented adhesion, and other optical properties.[7,91] And much work has been done to fabricate patterned surfaces, constructed by micro- or nanoscale structure arrays with multiple functions with the help of new insights and fabrication rules provided by the patterned surface existing naturally.[8,15,51,92–98] Based on this background, researchers turned their attention to using the patterned surfaces as biomaterials for biological applications, such as biosensing, controllable bio-adhesion and bio-patterning, and tissue engineering in vitro, since the patterned surfaces can provide more reaction sites, assured anchor points and oriented directions, feature structures for adhesion than that of the non-patterned surfaces.[99–101] There are few methods that are used in modern times. These are photolithography,[102] colloidal lithography,[103] electron beam lithography,[104] nanoimprinting lithography,[105] micro-contact printing,[106] dip-pen lithography,[61] etc. Among these methods, we are going focus only on colloidal lithography as it is the simplest one among all.

1.4.1 History of Self-assembly

Self-assembly was first noticed in 1935 by Langmuir and Blodgett during the famous Langmuir-Blodgett experiment on the formation of close-packed arrangements of amphiphilic molecules on a liquid and a solid surface. Later, in 1946, Bigelow et al. also observed long chain alkylamines from a densely packed monolayer on the surface of platinum. In 1983, Nuzzo and Allara contacted the gold surface with alkyl disulfide and discovered that they

formed close-packed monolayers of chemisorbed alkanethiolate molecules, called as self-assembled monolayers (SAMs). After more than a decade, in 1997, Deegan et al.[107,108] discovered contact line deposition by capillary force from a colloidal drying solution of coffee drop, a way to modify the surface topography without knowing the chemical nature of the liquid, solute or substrate. They termed this as "coffee stain effect." They have shown how uniformly distributed solute particles inside the drop have been deposited distinctly to the edge of the drop footprint after liquid is evaporated.[108] They also discovered how solute particle transportation occurs when the drop is evaporated. Due to contact line pinning, there is a radial flow inside the bubble. That flow carries most of the particle to the edge and helps to deposit on the surface. Studies have shown this stain effect with any type of colloidal suspension like ink, paint, salty water and blood.[109,110]

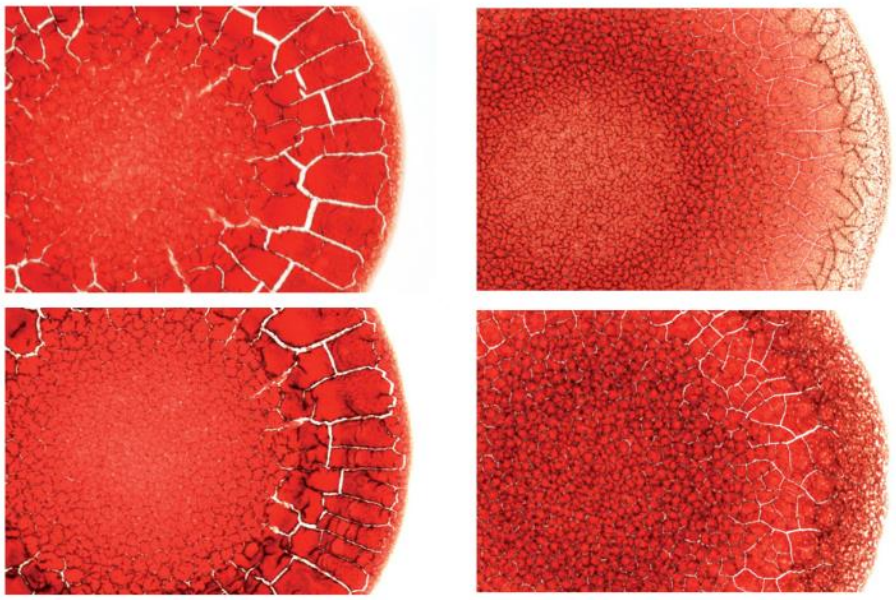

Figure 1.1: Four drops of blood: (a) sample from a 27-year-old woman in good health, (b) a person with anaemia, (c) sample from a 31-year-old man in good health and (d) a person with hyperlipidaemia.[109]

Now these days' the stain effect is pretty much in the limelight for its simple process of forming distinct stain patterns with evaporation-driven flow. Only disadvantage is that the stain

tends to be developed to the contact line. Therefore, particle concentration decreases towards the center. This problem is faced in the coating and printing industry. Analysis of DNA and proteins in microarrays is also tricky with the ring-stain patterns. If the particles are not uniformly distributed that leads to change in signal intensity.[111–113] Researchers have reported some different methods to overcome these problems by applying external forces like electric field, Mechanical vibration. These external forces drive the suspended particles and prevent from moving toward the contact line. A Homogeneous deposition is likely expected, but it is very difficult to achieve as microscale manipulation is nearly impossible.[114–116] There are several effects that influence the movement of the contact line, and that leads to unpredictable pattern formation. A proper explanation is still unresolved.

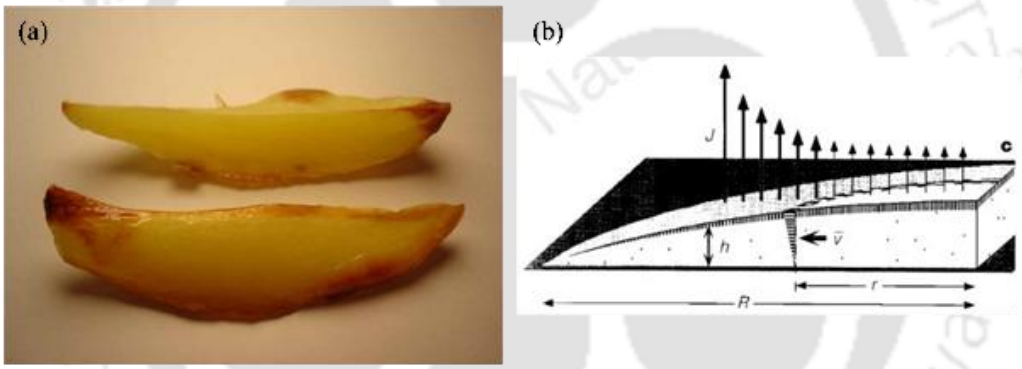

Figure 1.2: (a) Rapid dehydration from sharp edges causes potato wedges to burn at the edges first.[117] (b) The arrows indicate the non-uniform evaporative flux from the surface of the drop, at the periphery evaporative flux is higher than the away from the periphery.[68]

1.4.2 Evaporation-induced Self-assembly

Evaporation-induced self-assembly refers to that process where the phase separation of solute particles from a solution at the three-phase contact line of an evaporation driven liquid meniscus is exploited. Due to its versatile, simplistic, generic, and inexpensive characteristics, this technology will find its application in many smart industries and scientific quest where meso-patterning is the cynosure.

1.4.3 Physics Behind Evaporation

Let's Discuss the simple evaporation process that occurs in every liquid. A sphere cap shape is secured with a certain contact angle 'θ' after placing a drop on the surface. Liquid starts evaporating from the outer surface of the meniscus. Evaporation is driven by a gradient of concentration of the liquid with surrounding. Three tangible processes transport liquid molecules from bulk to the surrounding. First, phase change: the rate at which liquid molecules come across the air as vapor from the bulk [118,119]. Second, transport of the vapor molecule away from the drop into the atmosphere.[107,120,121] This is diffusion or a combination of diffusion and free convective transport. The third is evaporative cooling and heat transfer to the liquid-air interface.[119]

Due to the concentration gradient, liquid molecules cross the air-liquid interface into the atmosphere. Vapor concentration is more saturated at the interface than away from the drop. So, vapor molecules drive away from the interface, leading to more evaporation from the bulk of the liquid. As the liquid molecule gets vaporized, the drop size also decreases. Simultaneously, the air-liquid interface shifts from its' original position. This time-dependent vapor concentration 'c' is governed by the unsteady state diffusion equation

$$\frac{\partial c}{\partial t} = D\nabla^2 c \tag{1.1}$$

where, D is the diffusion constant for vapor in the air. Here motion of the drop is much slower than the diffusion time of vapor. Therefore, we may assume that the system is quasi-steady. The concentration is expressed by

$$\nabla^2 c = 0 \tag{1.2}$$

$$\mathbf{J} = -D\nabla c \tag{1.3}$$

J is the strength of the evaporative flux, deduced by the gradient in the vapor concentration from the drop surface. Vapor is saturated c_{sat} just above the drop surface, and c_∞ is the concentration away from the surface. These are the boundary condition to evaluate evaporative flux. If $c_\infty < c_{sat}$, then vapor diffuses towards the atmosphere. So that drop starts evaporating, and a diffusive out flux arises. Another boundary condition is that the vapor cannot diffuse into the substrate on which the drop rests. Researchers reported that this evaporative flux is not uniform all around the surface. Evaporation is much higher at the contact line than at the top surface when the substrate is partially-wetted ($0° < \theta < 90°$).[107,122] Drop forms a pointy wedge geometry, where evaporation is stronger. Hu and Lasron reinvestigated and simplified Deegan's model to determine the evaporative flux, which is as follows

$$\mathbf{J}(\mathbf{r}) = J_0(\theta)[1 - (\frac{r}{R})^2]^{-\lambda(\theta)} \tag{1.4}$$

where, r is radial coordinate, θ is contact angle and R is the wetted radius. The terms $J_0(\theta)$ and $\lambda(\theta)$ are defined as follows,[122,123]

$$J_0(\theta) = [D(c_{sat} - c_\infty)/R\,(0.27\theta^2 + 1.30)(0.6381 - 0.2239(\theta - \pi/4))^2] \tag{1.5}$$

$$\lambda(\theta) = 0.5 - \theta/\pi \tag{1.6}$$

to know the complete evaporation time of the entire drop, one has to know the evaporative flux. However, decrease in size also gives the duration. If drop volume is V, $V \sim R^3$, the diffusion time $t_d = {R^2}/{D}$, rate of volume changes as

$$\frac{dV}{dt} \sim \frac{R}{t_d} = -DR \tag{1.7}$$

Equation 1.7 expresses that the rate of volume change is proportional to the perimeter of the drop, and does not depend on the surface area. There are two modes that occur when air-liquid interface moves. First is constant contact angle, where the contact line rapidly moves

without change in contact angle while drop size reduces. The second is the constant contact line. In this case, drop is in pinned position, and the contact angle is proportional to the drop size.

1.5 Thesis Overview

The primary objective of this thesis is to adopt a low-cost approach for long-range pattern formation with polymers. We investigate a variety of polymeric structures comprising straight to undulated micro-threads or micro/nanodroplets of homo or blend polymers. The methodology, which has been adopted here, is a form of self-assembled micro/nanostructures from a moving contact line, termed as dynamic contact line lithography (DCLL). The first three problems, are based on the surface engineering of a Si/glass substrate. We investigate different morphological structures by various setups, collaborated with DCLL, and at the last problem, we develop an energy harvesting device, which shows the potential of DCLL in modern low-cost technology.

References

[1] W. Barthlott, C. Neinhuis, *Planta* **1997**, *202*, 1.

[2] S. Derler, R. Huber, H.-P. Feuz, M. Hadad, *Wear* **2009**, *267*, 1281.

[3] S. Walheim, E. Schäffer, J. Mlynek, U. Steiner, *Science (80-.).* **1999**, *283*, 520.

[4] S. C. Veenstra, W. J. H. Verhees, J. M. Kroon, M. M. Koetse, J. Sweelssen, J. J. A. M. Bastiaansen, H. F. M. Schoo, X. Yang, A. Alexeev, J. Loos, U. S. Schubert, M. M. Wienk, *Chem. Mater.* **2004**, *16*, 2503.

[5] J. L. Wu, F. C. Chen, Y. S. Hsiao, F. C. Chien, P. Chen, C. H. Kuo, M. H. Huang, C. S. Hsu, *ACS Nano* **2011**, *5*, 959.

[6] X. Chang, J. Fang, Y. Fan, T. Luo, H. Su, Y. Zhang, J. Lu, L. Tsetseris, T. D. Anthopoulos, S. Liu, K. Zhao, *Adv. Mater.* **2020**, *2001243*, 1.

[7] S. Wang, K. Liu, X. Yao, L. Jiang, *Chem. Rev.* **2015**, *115*, 8230.

[8] Z. Nie, E. Kumacheva, *Nat. Mater.* **2008**, *7*, 277.

[9] J. W. Lathrop, *IEEE Ann. Hist. Comput.* **2013**, *35*, 48.

[10] K. Autumn, Y. A. Liang, S. T. Hsieh, W. Zesch, W. P. Chan, T. W. Kenny, R. Fearing, R. J. Full, *Nature* **2000**, *405*, 681.

[11] H. Lee, B. P. Lee, P. B. Messersmith, *Nature* **2007**, *448*, 338.

[12] K. Liu, L. Jiang, *Nano Today* **2011**, *6*, 155.

[13] X. Gao, L. Jiang, *Nature* **2004**, *432*, 36.

[14] W. J. Hamilton, J. R. Henschel, M. K. Seely, *S. Afr. J. Sci.* **2003**, *99*, 181.

[15] A. del Campo, E. Arzt, *Chem. Rev.* **2008**, *108*, 911.

[16] K. Nozaki, N. Ebe, N. Horiuchi, M. Nakamura, Y. Tsutsumi, *Mater. Sci. Eng. C* **2015**, *57*, 1.

[17] X.-Q. Dou, D. Zhang, C. Feng, L. Jiang, *ACS Nano* **2015**, *9*, 10664.

[18] P. Kumnorkaew, Y. Ee, N. Tansu, J. F. Gilchrist, *Langmuir* **2008**, *24*, 12150.

[19] G. M. Whitesides, S. K. Y. Tang, in *Optofluidics*, **2006**, p. 63290A.

[20] G. Hughes, M. R. Bryce, *J. Mater. Chem.* **2005**, *15*, 94.

[21] J. J. Norman, T. A. Desai, *Ann. Biomed. Eng.* **2006**, *34*, 89.

[22] T. Maitra, C. Antonini, M. Auf der Mauer, C. Stamatopoulos, M. K. Tiwari, D. Poulikakos, *Nanoscale* **2014**, *6*, 8710.

[23] J. B. Boreyko, C.-H. Chen, *Phys. Rev. Lett.* **2009**, *103*, 184501.

[24] M.-R. Panahi-Bazaz, M. Zamani, B. Abazar, *J. Ophthalmic Vis. Res.* **2009**, *4*, 201.

[25] J. L. Marignier, *Nicéphore Niépce 1765-1833: L'invention de La Photographie*, Paris: Belin, **1999**.

[26] C. G. Willson, R. A. Dammel, A. Reiser, **1997**, 28.

[27] A. Pimpin, W. Srituravanich, *Eng. J.* **2012**, *16*, 37.

[28] D. P. Sanders, *Chem. Rev.* **2010**, *110*, 321.

[29] C. Wagner, N. Harned, *Nat. Photonics* **2010**, *4*, 24.

[30] R. F. Pease, S. Y. Chou, *Proc. IEEE* **2008**, *96*, 248.

[31] R. Menon, A. Patel, D. Gil, H. I. Smith, *Mater. Today* **2005**, *8*, 26.

[32] A. R. Neureuther, J. Rubinstein, E. Chin, L. Wang, M. Miller, C. Clifford, K. Yamazoe, *Jpn. J. Appl. Phys.* **2010**, *49*, DOI 10.1143/JJAP.49.06GA01.

[33] B. D. Gates, Q. Xu, M. Stewart, D. Ryan, C. G. Willson, G. M. Whitesides, *Chem. Rev.* **2005**, *105*, 1171.

[34] A. Pandey, S. Maity, K. Murmu, S. Middya, D. Bandyopadhyay, P. S. Gooh Pattader, *Nanotechnology* **2021**, *32*, 285302.

[35] Ş. Tirpanci, D. E. Bürgler, C. M. Schneider, B. Rameev, B. Aktaş, *Microelectron. Eng.* **2015**, *140*, 33.

[36] M. Altissimo, *Biomicrofluidics* **2010**, *4*, DOI 10.1063/1.3437589.

[37] C. Vieu, F. Carcenac, A. Pépin, Y. Chen, M. Mejias, A. Lebib, L. Manin-Ferlazzo, L. Couraud, H. Launois, *Appl. Surf. Sci.* **2000**, *164*, 111.

[38] **2002**, 2002.

[39] V. Grigaliūnas, A. Lazauskas, D. Jucius, D. Viržonis, B. Abakevičienė, S. Smetona, S. Tamulevičius, *Microelectron. Eng.* **2016**, *164*, 23.

[40] H. Morimoto, Y. Sasaki, K. Saitoh, Y. Watakabe, T. Kato, *Microelectron. Eng.* **1986**, *4*, 163.

[41] S. Reyntjens, R. Puers, *J. Micromech. Microeng* **2001**, *11*, 287.

[42] R. M. André, S. Pevec, M. Becker, J. Dellith, M. Rothhardt, M. B. Marques, D. Donlagic, H. Bartelt, O. Frazão, *Opt. Express* **2014**, *22*, 13102.

[43] J. Melngailis, *J. Vac. Sci. Technol. B Microelectron. Nanom. Struct.* **1987**, *5*, 469.

[44] C. Li, L. Zhao, Y. Mao, W. Wu, J. Xu, *Sci. Rep.* **2015**, *5*, DOI 10.1038/srep08236.

[45] M. De Ridder, W. C. L. Hopman, F. Ay, *Scanning* **2007**, *00*, 212.

[46] F. P. W. Melchels, J. Feijen, D. W. Grijpma, *Biomaterials* **2010**, *31*, 6121.

[47] A. Muzaffar, M. B. Ahamed, K. Deshmukh, T. Kovářík, T. Křenek, S. K. K. Pasha, *3D and 4D Printing of PH-Responsive and Functional Polymers and Their Composites*, **2019**.

[48] J. L. Walker, M. Santoro, *Processing and Production of Bioresorbable Polymer Scaffolds for Tissue Engineering*, Elsevier Ltd, **2017**.

[49] K. Salonitis, *Stereolithography*, **2014**.

[50] T. Saison, C. Peroz, V. Chauveau, S. Berthier, E. Sondergard, H. Arribart, *Bioinspir.*

Biomim. **2008**, *3*, 046004.

[51] J. Zhang, B. Yang, *Adv. Funct. Mater.* **2010**, *20*, 3411.

[52] X. Fu, W. Yang, M. He, Y. Li, Z. Hao, Y. He, C. Yuan, Y. Cui, H. Ge, *Mater. Lett.* **2020**, *260*, 126867.

[53] J. Chen, J. Shi, D. Decanini, E. Cambril, Y. Chen, A. M. Haghiri-Gosnet, *Microelectron. Eng.* **2009**, *86*, 632.

[54] S. Y. Chou, P. R. Krauss, *Microelectron. Eng.* **1997**, *35*, 237.

[55] H. Schulz, D. Lyebyedyev, H.-C. Scheer, K. Pfeiffer, G. Bleidiessel, G. Grützner, J. Ahopelto, *J. Vac. Sci. Technol. B Microelectron. Nanom. Struct.* **2000**, *18*, 3582.

[56] A. Cattoni, E. Cambril, D. Decanini, G. Faini, A. M. Haghiri-Gosnet, *Microelectron. Eng.* **2010**, *87*, 1015.

[57] P. Gogoi, A. Chattopadhyay, P. S. Gooh Pattader, *J. Phys. Chem. B* **2020**, *124*, 11530.

[58] J. Xu, J. Xia, S. W. Hong, Z. Lin, F. Qiu, Y. Yang, *Phys. Rev. Lett.* **2006**, *96*, 1.

[59] M. Gonuguntla, A. Sharma, *Langmuir* **2004**, *20*, 3456.

[60] U. Thiele, *Adv. Colloid Interface Sci.* **2014**, *206*, 399.

[61] A. C. Kandemir, S. N. Ramakrishna, D. Erdem, D. Courty, R. Spolenak, *Compos. Sci. Technol.* **2017**, *138*, 186.

[62] C. A. Mirkin, *ACS Nano* **2007**, *1*, 79.

[63] **N.d.**

[64] S. D. Cronin, K. Sabolsky, E. M. Sabolsky, K. A. Sierros, *Thin Solid Films* **2014**, *552*, 50.

[65] R. D. Piner, J. Zhu, F. Xu, S. Hong, **1999**, *283*, 661.

[66] B. Li, Y. Zhang, J. Hu, M. Li, *Ultramicroscopy* **2005**, *105*, 312.

[67] Q. Tang, S. Q. Shi, *Sensors Actuators, B Chem.* **2008**, *131*, 379.

[68] P. Roy, R. Mukherjee, D. Bandyopadhyay, P. S. Gooh Pattader, *Nanoscale* **2019**, *11*, 16523.

[69] P. Roy, P. S. Gooh Pattader, *Bull. Mater. Sci.* **2020**, *43*, 169.

[70] J. M. Reynolds, *Phys. Fluids* **1965**, *8*, 161.

[71] N. Arun, A. Sharma, P. S. G. Pattader, I. Banerjee, H. M. Dixit, K. S. Narayan, *Phys. Rev. Lett.* **2009**, *102*, 254502.

[72] G. Zhang, D. Wang, *Chem. - An Asian J.* **2009**, *4*, 236.

[73] U. C. Fischer, H. P. Zingsheim, *J. Vac. Sci. Technol.* **1981**, *19*, 881.

[74] C. Papadopoulos, *SpringerBriefs Mater.* **2016**, *377*, 37.

[75] C. N. R. Rao, G. U. Kulkarni, P. J. Thomas, V. V. Agrawal, P. Saravanan, *J. Phys. Chem. B* **2003**, *107*, 7391.

[76] C. N. R. Rao, G. U. Kulkarni, P. J. Thomas, P. P. Edwards, *Chem. Soc. Rev.* **2000**, *29*, 27.

[77] C. N. R. Rao, G. U. Kulkarni, V. V. Agrawal, U. K. Gautam, M. Ghosh, U. Tumkurkar, *J. Colloid Interface Sci.* **2005**, *289*, 305.

[78] W. G. Bae, H. N. Kim, D. Kim, S. H. Park, H. E. Jeong, K. Y. Suh, *Adv. Mater.* **2014**, *26*, 675.

[79] T. Sun, G. Qing, B. Su, L. Jiang, *Chem. Soc. Rev.* **2011**, *40*, 2909.

[80] B. L. Feng, S. H. Li, Y. S. Li, H. J. Li, L. J. Zhang, J. Zhai, Y. L. Song, B. Q. Liu, L. Jiang, D. B. Zhu, *Adv. Mater.* **2002**, *14*, 1857.

[81] X. Gao, X. Yan, X. Yao, L. Xu, K. Zhang, J. Zhang, B. Yang, L. Jiang, *Adv. Mater.* **2007**, *19*, 2213.

[82] N. Becker, E. Oroudjev, S. Mutz, J. P. Cleveland, P. K. Hansma, C. Y. Hayashi, D. E. Makarov, H. G. Hansma, *Nat. Mater.* **2003**, *2*, 278.

[83] Y. Zheng, H. Bai, Z. Huang, X. Tian, F. Q. Nie, Y. Zhao, J. Zhai, L. Jiang, *Nature* **2010**, *463*, 640.

[84] Y. Liu, Z. Shao, F. Vollrath, *Nat. Mater.* **2005**, *4*, 901.

[85] Y. Cai, L. Lin, Z. Xue, M. Liu, S. Wang, L. Jiang, *Adv. Funct. Mater.* **2014**, *24*, 809.

[86] P. Y. Chen, A. Y. M. Lin, J. McKittrick, M. A. Meyers, *Acta Biomater.* **2008**, *4*, 587.

[87] H. Rhee, M. F. Horstemeyer, Y. Hwang, H. Lim, H. El Kadiri, W. Trim, *Mater. Sci. Eng. C* **2009**, *29*, 2333.

[88] I. H. Chen, J. H. Kiang, V. Correa, M. I. Lopez, P. Y. Chen, J. McKittrick, M. A. Meyers, *J. Mech. Behav. Biomed. Mater.* **2011**, *4*, 713.

[89] W. Yang, I. H. Chen, B. Gludovatz, E. A. Zimmermann, R. O. Ritchie, M. A. Meyers, *Adv. Mater.* **2013**, *25*, 31.

[90] K. Liu, Y. Tian, L. Jiang, *Prog. Mater. Sci.* **2013**, *58*, 503.

[91] Y. Li, J. Zhang, B. Yang, *Nano Today* **2010**, *5*, 117.

[92] H. H. Han, M. C. Lee, S. H. Kim, J. H. Lee, S. T. Ahn, J. W. Rhie, *Arch. Plast. Surg.* **2014**, *41*, 271.

[93] J. Zhang, Y. Li, X. Zhang, B. Yang, *Adv. Mater.* **2010**, *22*, 4249.

[94] R. Ogaki, M. Alexander, P. Kingshott, *Mater. Today* **2010**, *13*, 22.

[95] T. Blattler, C. Huwiler, M. Ochsner, B. Stadler, H. Solak, J. Voros, H. Grandin, *J. Nanosci. Nanotechnol.* **2006**, *6*, 2237.

[96] D. C. Chow, M. S. Johannes, W. K. Lee, R. L. Clark, S. Zauscher, A. Chilkoti, *Mater. Today* **2005**, *8*, 30.

[97] K. L. Christman, V. D. Enriquez-Rios, H. D. Maynard, *Soft Matter* **2006**, *2*, 928.

[98] R. Ganesan, K. Kratz, A. Lendlein, *J. Mater. Chem.* **2010**, *20*, 7322.

[99] B. Derby, *Science (80-.).* **2012**, *338*, 921.

[100] W. Liu, Y. Li, B. Yang, *Sci. China Chem.* **2013**, *56*, 1087.

[101] J. El-Ali, P. K. Sorger, K. F. Jensen, *Nature* **2006**, *442*, 403.

[102] M. C. Marconi, P. W. Wachulak, *Prog. Quantum Electron.* **2010**, *34*, 173.

[103] R. D. Deegan, *Phys. Rev. E* **2000**, *61*, 475.

[104] Y. Chen, *Microelectron. Eng.* **2015**, *135*, 57.

[105] A. Jain, A. Spann, A. Cochrane, P. Randall Schunk, R. T. Bonnecaze, *Microelectron. Eng.* **2017**, *173*, 62.

[106] C. Crozatier, M. Le Berre, Y. Chen, *Microelectron. Eng.* **2006**, *83*, 910.

[107] R. D. Deegan, O. Bakajin, T. F. Dupont, G. Huber, S. R. Nagel, T. A. Witten, *Nature* **1997**, *389*, 827.

[108] R. D. Deegan, O. Bakajin, T. F. Dupont, G. Huber, S. R. Nagel, T. A. Witten, *Phys. Rev. E - Stat. Physics, Plasmas, Fluids, Relat. Interdiscip. Top.* **2000**, *62*, 756.

[109] D. BRUTIN, B. SOBAC, B. LOQUET, J. SAMPOL, *J. Fluid Mech.* **2011**, *667*, 85.

[110] J. Perelaer, P. J. Smith, C. E. Hendriks, A. M. J. van den Berg, U. S. Schubert, *Soft Matter* **2008**, *4*, 1072.

[111] G. McHale, *Analyst* **2007**, *132*, 192.

[112] R. Blossey, A. Bosio, *Langmuir* **2002**, *18*, 2952.

[113] Y. Kim, G. B. Hurst, M. J. Doktycz, M. V. Buchanan, *Anal. Chem.* **2001**, *73*, 2617.

[114] J. Boneberg, F. Burmeister, C. Schäfle, P. Leiderer, D. Reim, A. Fery, S. Herminghaus, *Langmuir* **1997**, *13*, 7080.

[115] L. Meng, H. Wei, A. Nagel, B. J. Wiley, L. E. Scriven, D. J. Norris, *Nano Lett.* **2006**, *6*, 2249.

[116] M. Layani, M. Gruchko, O. Milo, I. Balberg, D. Azulay, S. Magdassi, *ACS Nano* **2009**, *3*, 3537.

[117] L. Bocquet, *Am. J. Phys.* **2007**, *75*, 148.

[118] H. Gelderblom, Á. G. Marín, H. Nair, A. Van Houselt, L. Lefferts, J. H. Snoeijer, D. Lohse, *Phys. Rev. E - Stat. Nonlinear, Soft Matter Phys.* **2011**, *83*, 1.

[119] B. Sobac, D. Brutin, *Langmuir* **2011**, *27*, 14999.

[120] M. Sbragaglia, A. M. Peters, C. Pirat, B. M. Borkent, R. G. H. Lammertink, M. Wessling, D. Lohse, *Phys. Rev. Lett.* **2007**, *99*, 1.

[121] P. Tsai, R. G. H. Lammertink, M. Wessling, D. Lohse, *Phys. Rev. Lett.* **2010**, *104*, 2.

[122] H. Hu, R. G. Larson, *J. Phys. Chem. B* **2002**, *106*, 1334.

[123] R. Bhardwaj, *Colloid Interface Sci. Commun.* **2018**, *24*, 49.

Chapter 2
Literature Review

This page is left blank intentionally

On the demand for structured surfaces for various applications, a number of studies have been reported about different methodologies of surface engineering in the micro/nanoscale, and it is still counting. This thesis mainly focuses on the self-deposition of polymeric structures from a moving contact line and its applications. Therefore, the subsequent sections discuss some relevant reported works as a literature survey.

2.1 Recent Works on Contact Line Deposition and The Deposited Features

Fefen et al.[1] have approached experimentally to get a coffee stain patterns with self-assembled microparticles. Some chemically functionalized microbeads are used for the coffee stain deposition process. A fixed concentration (0.02% wt vol^{-1}) solution is prepared and deposited on a glass slide. Polystyrene and silica beads, size of 500 nm, are used as particles. As evaporation is a much slower process, a porous media (wick) is introduced to take out the liquid. During the evacuation, a high degree of contact angle hysteresis is also found to develop at the contact line when contact angle reaches below $5°$ which imply evacuation flow and particle jamming at the contact line (Figure 2.1 & 2.2).

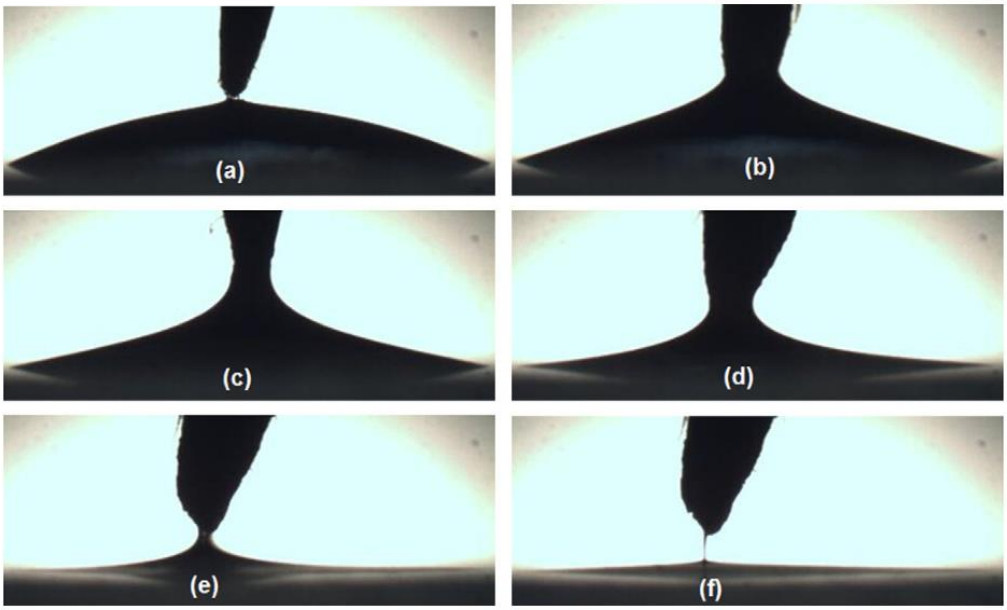

Figure 2.1: Side image of the droplet during evacuation at time evolution of (a) 0 s, (b) 0.72 s, (c) 1.29 s, (d) 2 s, (e) 2.58 s, and (f) 2.72 s.[1]

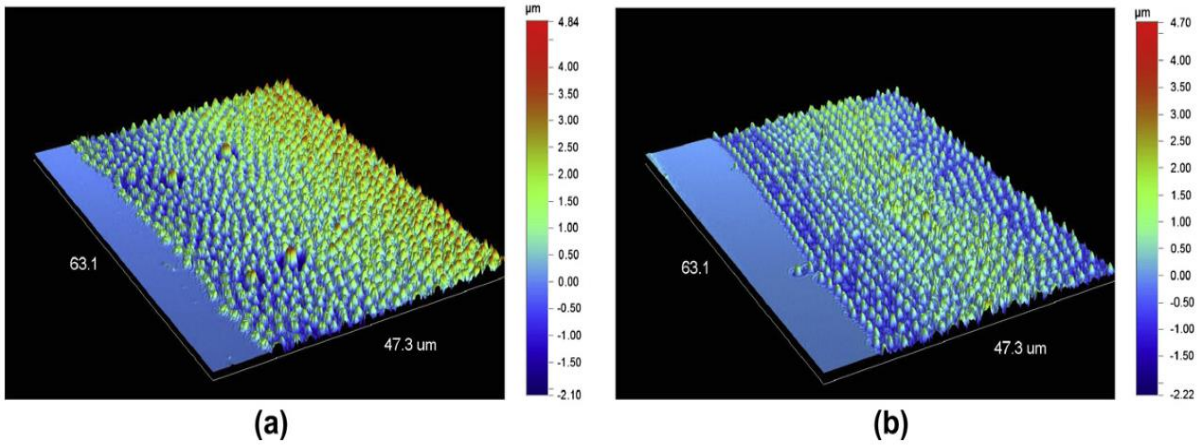

Figure 2.2: High magnification optical profilometry readings of (a) polystyrene and (b) silica microspheres at the front of the coffee stain ring deposited for 13 min before evacuation. The polystyrene array appears "higher" despite each microsphere being of the same size, indicating a higher propensity of stacking on top of each other with these particles.[1]

F.F. Shao et al.[2] have investigated the methods of intervening in the natural process of particle collection in an evaporating droplet. They have shown how to remove the smear of particles randomly distributed within a single ring and to create more ordered and concentric multiple-ring patterns (Figure 2.3). The techniques have then been shown to control deposition's cross-sectional characteristics.

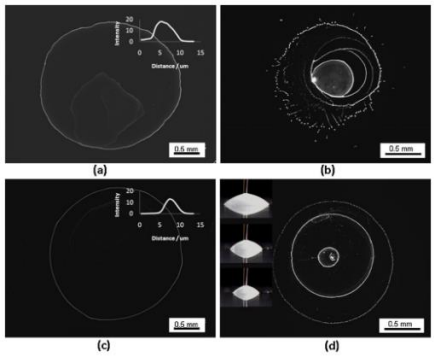

Figure 2.3: (a) Under natural condition, a single ring was formed on glass slide after evaporation process completed (the intensity profile taken across the ring shows its width and height), (b) while multiple rings were formed on a "starfrost" coated glass slide. (c) When the natural condition was distributed, a single ring well was formed by removal of the remaining fluid before the evaporation process completed (the intensity profile this time shows the decreased width and height), and (d) concentric rings were formed by extract-inject motion via a fine needle connect with syringe.[2]

W. D. Ristenpart et al.[3] have studied the effect of Marangoni flows on the deposition pattern by forcing particles toward the drop center. They have demonstrated experimentally that thermal Marangoni flow in evaporating droplets depends sensitively on the ratio of the liquid and substrate thermal conductivity. A quantitative derivation shows the direction and magnitude.

$$k_R^{crit} = \tan(\theta_c)\cot(\frac{\theta_c}{2} + \frac{\theta_c^2}{\pi}) \quad (2.1)$$

k_R^{crit} is the critical thermal conductivity ratio. It is the ratio of Substrate and liquid thermal conductivity. The values of k_R above the curve (Figure 2.4 & 2.5), the temperature decreases with distance from the contact line, and the flow is directed radially outward along the substrate.

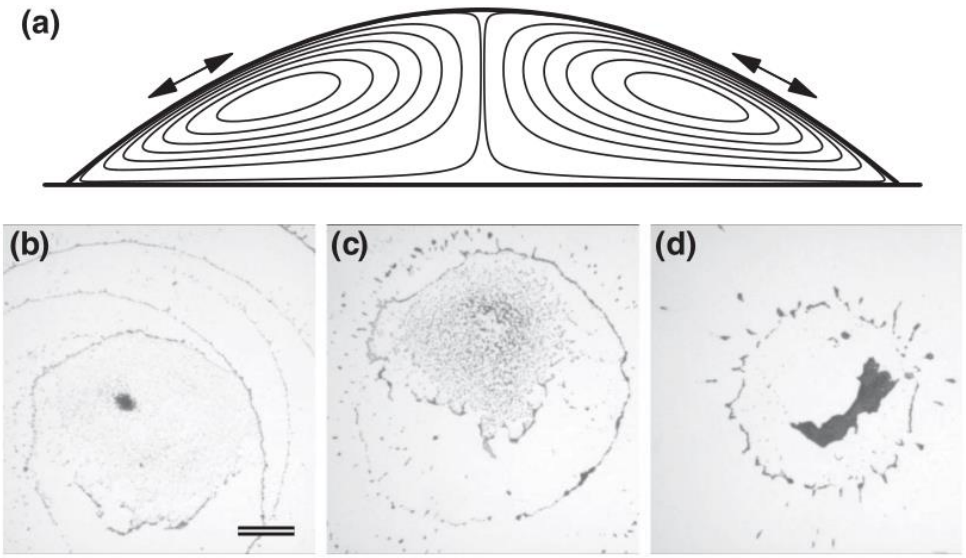

Figure 2.4: (a) Qualitative depiction of the streamlines observed inside evaporating droplets on PDMS. Arrows indicate the direction of different liquid: upward for isopropanol and chloroform, downward for methanol and ethanol. (b)-(d) Particle deposition patterns resulting from different evapoting fluids on PDMS. INeach case, a high concentration of particles deposited in a central part of the pattern near the stagnation points of the Marangoni flow. (b) Methanol, (c) Ethanol. (d) Isopropanol. Scale bar is 0.2 mm.[3]

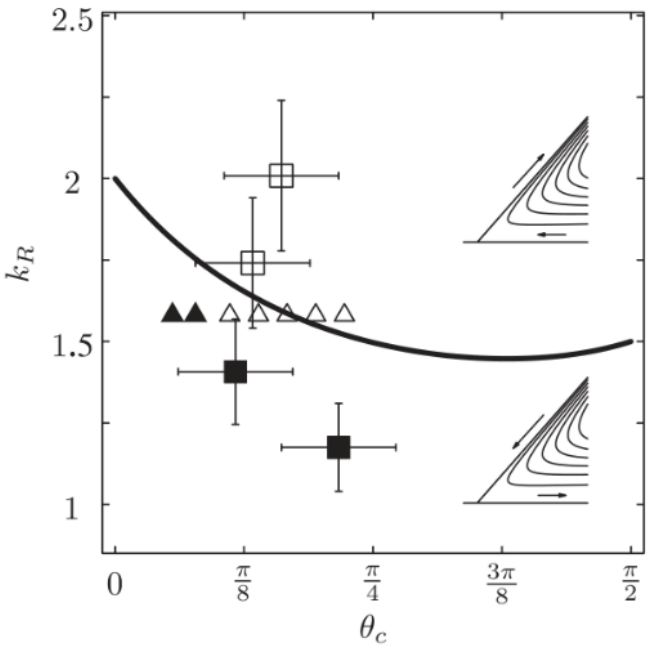

Figure 2.5: Experimental observations and numerical calculations of the circulation direction inside evaporating drops. The solid line is Eq. (1). Regions above and below the line correspond to circulation directions sketched in the respective streamlines, obtained from the asymmetric corner flow solution.[3]

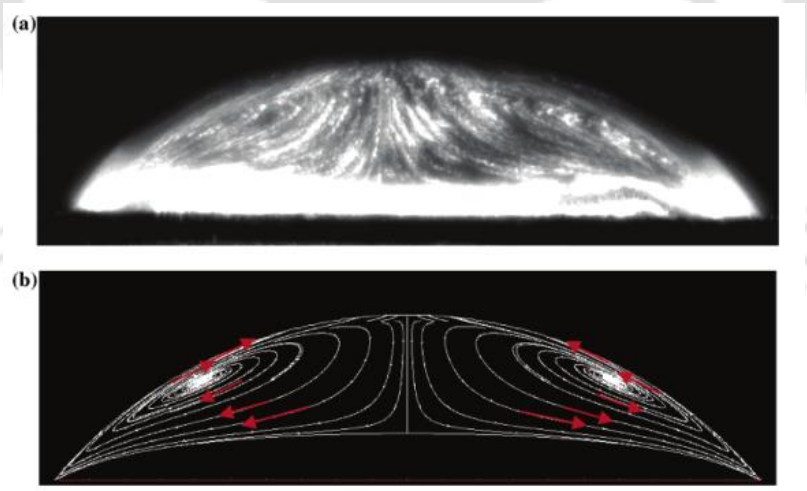

Figure 2.6: Flow field in a drying octane droplet, (a) imaged experimentally and (b) predicted ($M_a = 45800$). To observe a clear Marangoni Vortex the illumination plane was moved forward about 0.66 mm from the symmetrical axis of the droplet.[4]

Hua Hu et al.[4] also have shown the reverse coffee ring deposition due to Marangoni flow. They have mentioned that manipulating this Marangoni flow in a drying droplet should

allow one, in principle, to control and redirect evaporation-driven deposition and assembly of colloids and other materials (Figure 2.6).

Hanneke Gelderblom et al.[5] have reported that monodisperse colloidal particles have revealed a structural transition, originated from a temporal singularity of the flow velocity inside the evaporating droplet at the end of its life. Particles have time to arrange themselves by Brownian motion when deposition speed is low, but at the end, high-speed particles are deposited into a disordered phase (Figure 2.7 & 2.8).

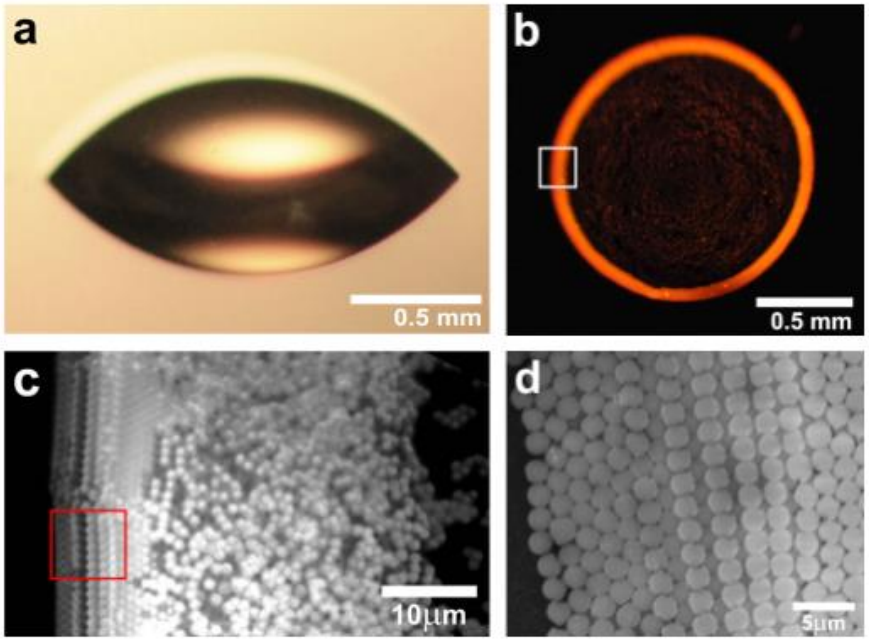

Figure 2.7: Order-to-disorder transition in the particle stain left by an evaporating drop. (a) A 3 µl sessile water droplet evaporates from a glass substrate. (b) Ring-shaped stain of red particles (the coffee stain) left on the substrate after evaporation. (c) A close-up by an optical microscope of the bottom layer of the stain, taken from the white square in (b), shows that the outermost lines of the stain (left) have an ordered, crystalline structure. Towards the center of the drop (right), a transition to a disordered particle arrangement is observed. (d) A top view of the ring stain, taken from the red square in (c) with a scanning electron microscope (SEM), shows that the first lines of particles (left) are arranged in a hexagonal array, while the next lines (brighter in the image) are arranged as square, followed by again hexagonal array.[5]

Peter J. Yunker et al.[6] have reported that the shape of the suspended particles is important and can be used to eliminate the coffee-ring effect. Ellipsoidal particles are deposited

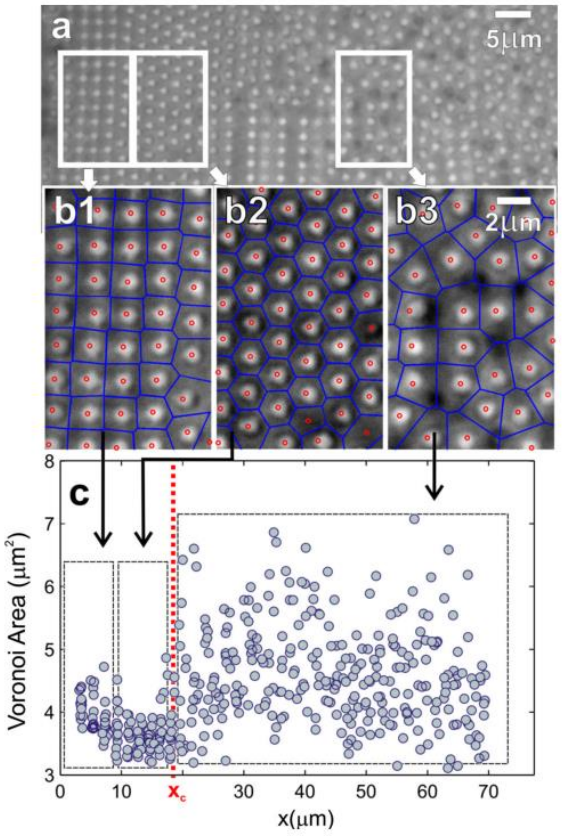

Figure 2.8: Analysis of the particle ordering in the stain. (a) Overview of the different patterns observed in the ring stain. The position of the contact line is on the left side of the figure (the first layers of particles are not shown). (b1)–(b3) A close-up reveals the sequence of patterns in the stain: square packing close to the contact line (b1), followed by hexagonal packing (b2), and finally disordered packing (b3). The Voronoi cells belonging to the particles are shown by blue lines. (c) The area of the Voronoi cells plotted versus the distance x from the contact line.[5]

uniformly during evaporation. The anisotropic shape of the particles significantly deforms interfaces producing strong interparticle capillary interactions.[7–13] Thus, after the ellipsoids are carried to the air-water interface by the same outward flow that causes the coffee-ring effect for spheres (Figure 2.9). Strong long-ranged interparticle attractions between ellipsoids lead to the formation of loosely packed or arrested structures on the air-water interface.[7,8,11,14]

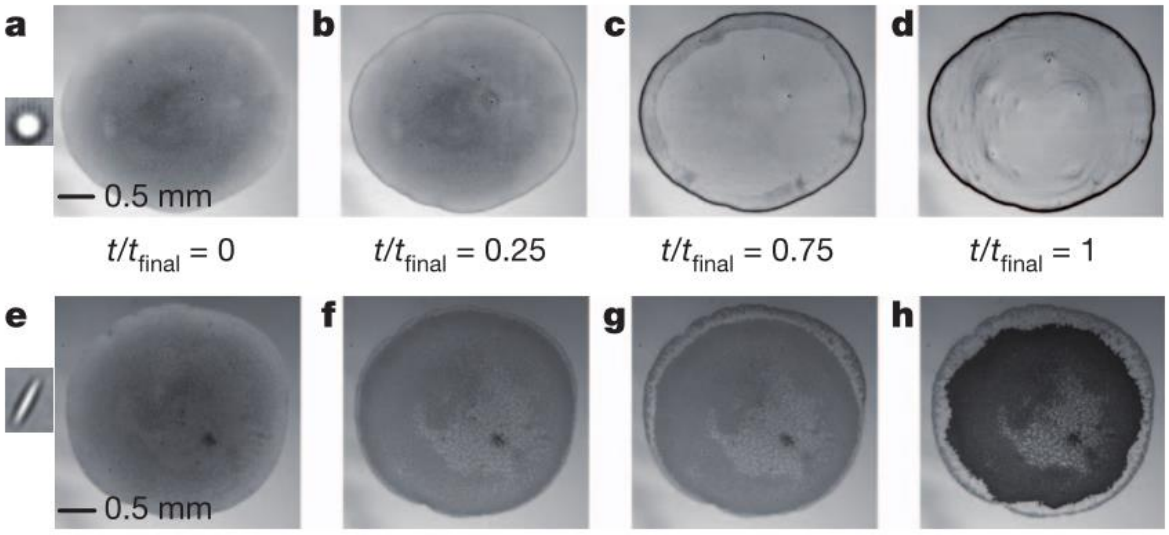

Figure 2.9: Transportation of particles over time. a-h, Experimental snapshot at different times t/t_{final} during the evaporation of a drop of particle suspension; shown are data for spherical particles (a-d) and for ellipsoidal particles with aspect ratio $\alpha = 3.5$ (e-h).[6]

These structures prevent the suspended particles from reaching the drop edge and ensure uniform deposition. Interestingly, under appropriate conditions, suspended spheres mixed with a small number of ellipsoids also produce uniform deposition. Thus, particle shape provides a convenient parameter to control the deposition of particles without modification of particle or solvent chemistry.

Hiroshi Yabu et al.[15] have proposed a novel method to fabricate patterns from receding meniscus on a solid surface. A chloroform solution of polystyrene and poly(3-hexylthipene) is prepared. Polymer solutions (200 µl) are placed in between two glass slides. Both glasses are separated by a narrow gap of 200 µm. The upper glass plate is moved at speed from 10 µm s^{-1} to 400 µm s^{-1}. A thin liquid film is formed behind the moving edge of the glass plate. A rapid evaporation of solvent at the meniscus helps to form the mesoscale pattern on the surface (Figure 2.10).

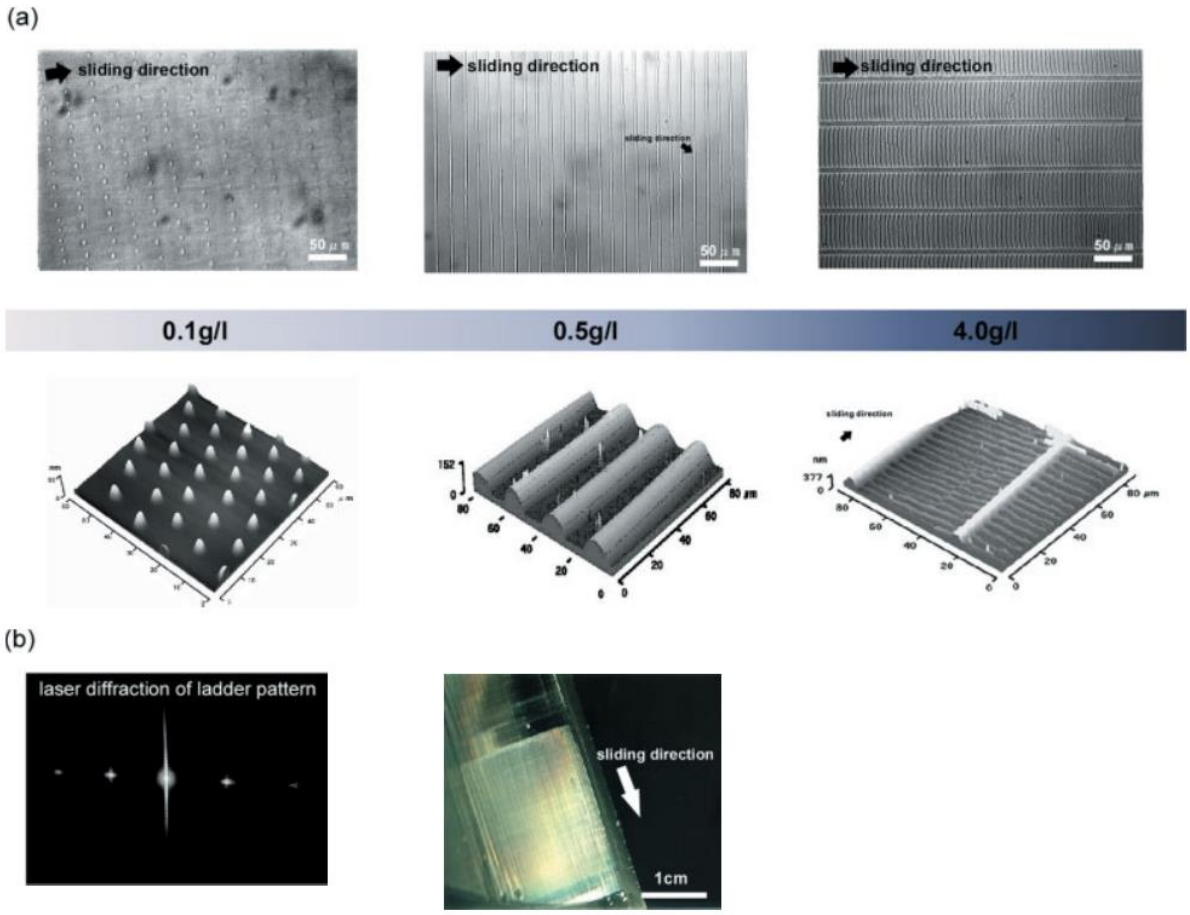

Figure 2.10: (a) Optical (upper row) and atomic force (lower row) microscopy images of polymer pattern prepared from polystyrene solutions. (b) The ladder pattern prepared on the glass plate and its laser diffraction pattern.[15]

Pisist Kumnorkaew wt al.[16] have reported a new method to fabricate micro-patterned surfaces. Dragging a meniscus of a suspension across a substrate helps to deposit a monolayer of microspheres. The primary colloid suspension is used in this work. A colloidal solution is prepared by dispersing silica microspheres having a density of $2.2\,\mathrm{g\,cm^{-3}}$ and average diameter of 0.50 ± 0.01 and 1.01 ± 0.02 µm in deionized water with a volume fraction of $\emptyset$=0.2. for the fabrication of micro-lens arrays, a separate solution of 1.1 µm polystyrene was prepared at $\emptyset$=0.2 in DI water. In controlled humidity chamber, a glass slide is placed on a glass substrate (Figure 2.11, 2.12 & 2.13). The distance is maintained at 10 µm between two glass substrates. At different sets of angle glass slide is dragged along with the meniscus at a

speed of $20 - 90\ \mu m\ s^{-1}$. Thus, a monolayer of particles is deposited on the surface to fabricate micro-lens arrays.

Figure 2.12 depicts a schematic of configuration of the fabricated micro-lens arrays. Here, gallium nitride (GaN) is a base contact layer of the indium gallium nitride (InGaN) quantum well (QW) LEDs device. Polystyrene (PS) and silica monolayers are deposited subsequently. At first, PS is deposited, and dried in air, followed by deposition of silica monolayer. Here, monolayer of PS microparticles acts as a template for the deposition of the silica monolayer. The sample is then heated above the melting temperature of the PS ($\sim$240 ℃), so that the silica monolayer is wetted by the melted polystyrene. The obtained morphologies of silica monolayer that include submonolayer, monolayer, and multilayer, are depicted in Figure 2.13. Within each of these morphologies, multiple microstructures are observed including randomly deposited colloids and both locally and long-range-ordered structures with various packings and symmetries.

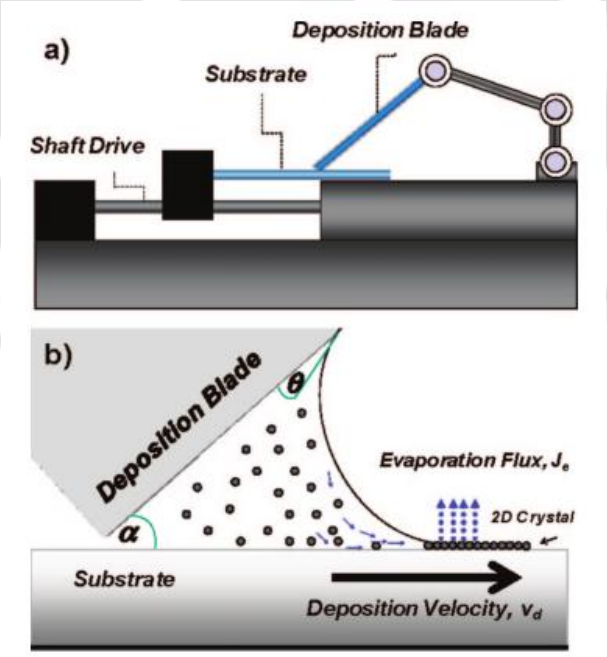

Figure 2.11: Experimental setup showing equipment (a) and the local deposition process (b) where a meniscus is pulled relative to the substrate to induce deposition and the local ordering of particles.[16]

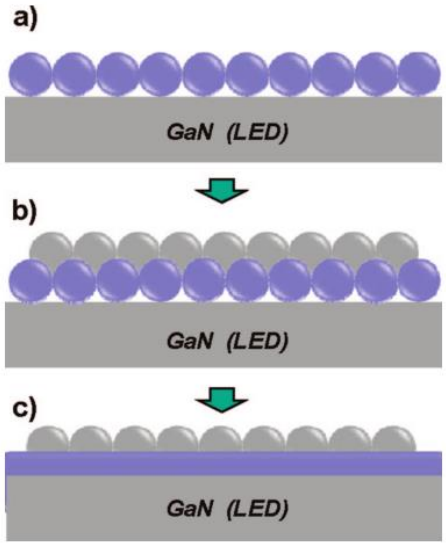

Figure 2.12: Deposition process to fabricate micro-lens arrays, (a) An initial monolayer of 1.1 µm polystyrene microspheres is deposited on the InGaN/GaN quantum well LED. (b) A second monolayer of 1.01 µm SiO_2 is deposited on top of the PS layer. (c) Heating above the melting temperature of PS partially submerges the SiO_2 microspheres, forming the desired geometry.[16]

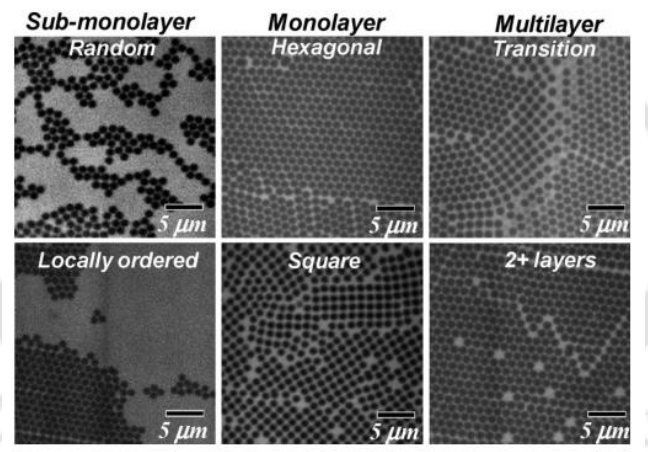

Figure 2.13: Three resulting morphologies are submonolayer, monolayer and multilayer depositions. Various microstructures may exist, including random and locally ordered morphologies in the submonolayer regime, hexagonal and square close-packed monolayer crystals, and transition regions separating various microstructures formed in 3D.[16]

Koushik Viswanathan et al.[17] are in favor of stick-slip modes at the interface of two polymer surfaces while in movement. They have talked about three waves that directly affect the movement of the substrates.

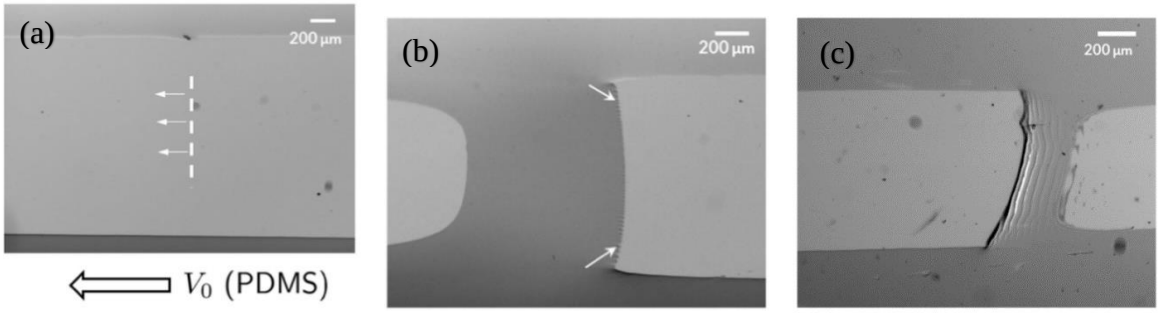

Figure 2.14: (a) Slip pulse propagation. In optical image, dirt particles inside the contact are seen to move in the direction of V_0 (remote velocity). However, wave features are not visible since interface detachment does not occur. (b) Shape of separation pulse near the $2a$ (applied normal loads) transition. Large tensile strains are evident in the wrinkle marks (at arrows) at the front of the wave. For slightly larger $2a$ values, detachment is not observed, and a slip pulse propagates instead. (c) Schallamach wave propagation in an imperfect contact. Despite the presence of dirt particles/scratches inside the contact region, Schallamach wave propagation occurs albeit with altered geometry as shown here. The wave shape is distinctly different from a single wave inside a perfect adhesive contact with no impurities.[17]

First one is due to their slow propagation speeds, called Schallamach waves. The second is the slip pulse which is a sharp stress front that propagates in the same direction as the Schallamach wave. The last one is the separation pulse involves local interface detachment and travels in the opposite direction. The transition between these stick-slip modes is easily affected by changing the sliding velocity or normal load (Figure 2.14).

The direction of wave propagation V_0 can be explained in terms of the tension/ compression at the free surface. Using the coordinate system, the direction of propagation is linked to the sign of the surface strain ϵ_{xx}. For steady-state constant velocity propagation, the tangential interface displacement u_x is a function $u_x(x - \tilde{V}t)$. The surface strain ϵ_{xx} can be approximated as

$$\epsilon_{xx} = \frac{\partial u_x}{\partial x} \cong -\tilde{V}^{-1}\frac{\Delta x}{T} \tag{2.2}$$

where, Δx is the slip per wave and T is the duration of propagation. The sign of Δx is the same as V_0, so that strain ϵ_{xx} is negative if the wave propagates in the same direction as V_0 and is positive if it propagates in the opposite direction. For the case of Schallamach waves and slip pulses $\epsilon_{xx} < 0$, and they result in compressive surface strain. For separation pulse $\epsilon_{xx} > 0$ and the surface strain is tensile.

Hugues bodiguel et al.[18] have shown stick-slip mode in the evaporating silica-suspended droplet. After evaporation, a pattern formation is exhibited from the suspended particles. Their study is mainly focused on the stick-slip regime and the formation of the patterns (Figure 2.15 & 2.16). Their analysis supports the idea that the pinning of the contact line results from a competition between the geometry of the deposit and the force due to gravity.

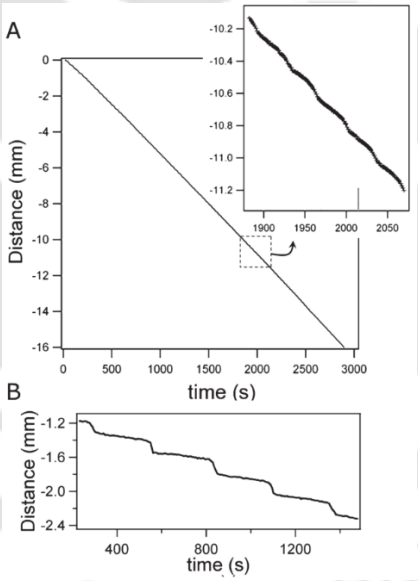

Figure 2.15: Examples of the meniscus displacement obtained by the analysis of the images. (A) The imposed average velocity is 5.5μm s^{-1}, temperature 25°C, humidity 30%. (B) Strong stick-slip at 0.95 μm s^{-1} with a volume fraction of 1.4%.[18]

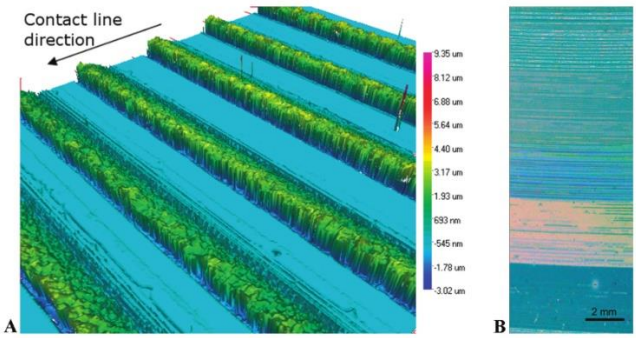

Figure 2.16: (A) Optical profilometer image of a periodic deposit obtained in the following conditions: imposed average velocity = 1 μm s^{-1}, particle volume fraction = 1.41%, humidity 90%, temperature 25°C, $v_{evap} \cong 0.06\mu m\ s^{-1}$. The typical pattern height is 5 μm. (B) Optical image of a dried glass slide.[18]

Wei Sun et al.[19] have shown a different yet simple method to fabricate gradient grating on polymer films in an economical and efficient way. Copper wires of varying diameters 51, 79 and 102 μm are placed separately on a 90 nm thick poly(methyl methacrylate) (PMMA) film. Copper wire is covered by 20 μl toluene solvent. Gradient surface stripes are constructed on PMMA film. Results show the variation of the spatial wavelength with the distance to the copper wire center. The spatial wavelength decreases linearly with a decrease of the distance to the copper wire center (Figure 2.17 & 2.18).

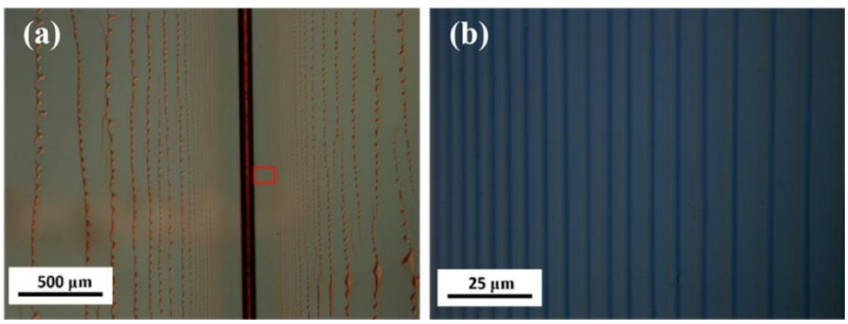

Figure 2.17: Optical images of the evaporation-induced surface pattern: (a) surface patterns formed via a single copper wire and (b) enlarged view of the surface pattern in the enclosed area in (a) (Film Thickness 90 nm, diameter of the copper wire 79 μm).[19]

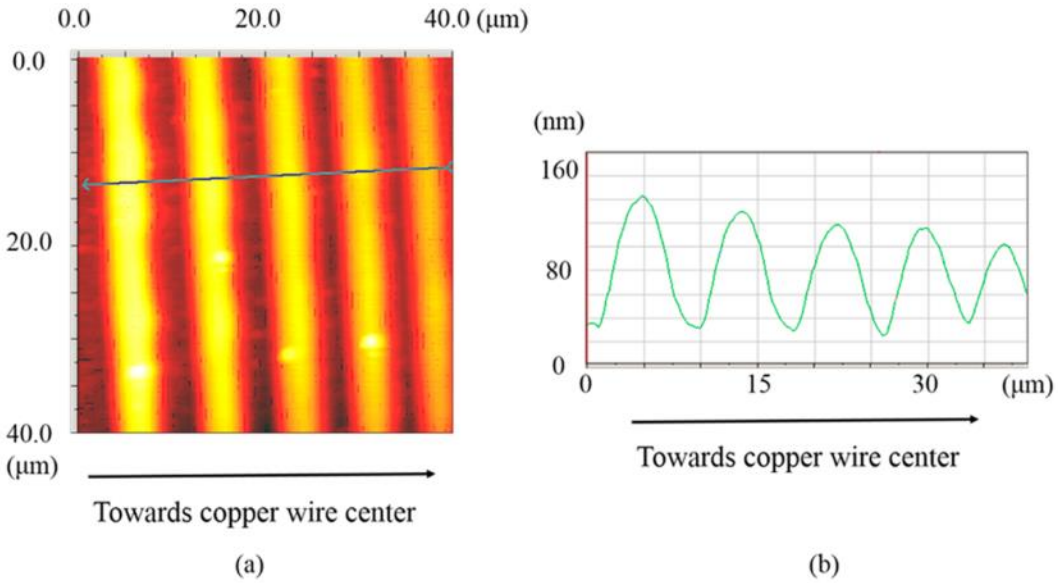

Figure 2.18: (a) AFM image of the parallel stripes over an area of $40 \times 40\ \mu m^2$ and (b) Surface profile of the parallel stripes.[19]

2.2 Recent Works on Patterned Surface Based Applications

2.2.1 Biosensing

Patterned surfaces with ordered structures have been introduced into the field of sensing, since their ordered two-dimensional structures, which can provide more reactive sites, enhanced sensitivity and obvious visualization. A variety of sensing platforms based on two-dimensional patterned surfaces have been fabricated for protein, DNA, cell and bacteria sensing. In this part, we will present a brief introduction of the research progress focused on patterned surfaces-based sensing.

2.2.1.1 Protein Sensing

As an essential organism component, protein has played a specific role in maintaining daily activities.[20–25] Protein can perform incredible stereo-structures since it does not have a predictable sequence and always perform multimerization and post-modification after the translation process. The structures of the protein are also diverse and have a great effect on the organism functions in daily life. Thus, it is essential to build a facile and sensitive platform for

the detection of the proteins that act as a feature markers for specific functions.[26–31] Taking advantage of patterned surfaces, Zhang et al. fabricated sensitive protein sensors based on elevated silver nano-hole arrays by reactive ion etching and vapor deposition.[32]

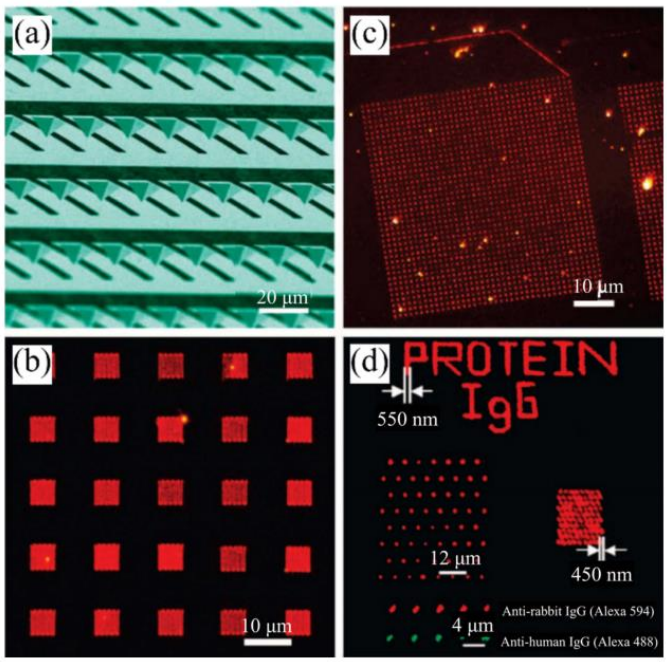

Figure 2.19: Dip-pen nanolithography approach for the preparation of functional patterns. (a) SEM image of part of a 55,000-pen 2D array. (b) Fluorescence microscopy of 1 mol% rhodamine-labeled 1,2-dioleoyl-sn-glycero-3-phosphocho-line. (c) Dark-field light-scattering image of gold nanoparticles hybridized to immobilized DNA patterns created by passive 26-pen arrays. (d) Fluorescence images of protein patterns generated by DPN.[33]

Jung-Hyurk Lim et al.[34] fabricated protein nanostructured pattern on a modified silicon oxide surface (Figure 2.19 (d)) by dip-pen nanolithography (DPN). There were two types of protein. First, rabbit immunoglobulin G (IgG, developed in goat, Sigma), and second, human immunoglobulin G. Two types of protein were deposited separately on separate substrates. Later, both the samples were immersed in antirabbit IgG (Labeled with Alexa 594) and antihuman IgG (Labeled with Alexa 488) solutions, respectively. Fluorescence microscopy showed a prominent selective attachment of anti-IgGs with their respective IgGs. A cross attachment is also reported with a percentage of < 20 %.

2.2.1.2 DNA Sensing

Besides the protein mentioned above, DNA is another kind of important macromolecule that exists in organisms. It has a long history that can trace back to the birth of life, carrying genetic information and acting as the foundational materials for biological heredity. Life will present unexpected phenotype or subject to different diseases due to the mutation at specific sites of its backbone structure. Therefore, it has become a very important problem for rapid DNA detection to evaluate the life's health status before the phenotypes emerge. Taking advantage of the double helix structure, DNA chains can have various secondary structures, which endow the DNA chains with the ability to recognize DNA, RNA, protein, and other molecules. And this provides opportunities for researchers to prepare DNA sensors based on patterned surfaces with a low detection limit, simplified approaches, less input and conduct in rapidly with high performance.[35,36] Liu et al. reported a facile and cost-efficiency method to fabricate single-strand DNA (ssDNA) nano-cone arrays and hierarchical ssDNA patterns (Figure 2.20), which perform great potential in specific DNA sensing.[37]

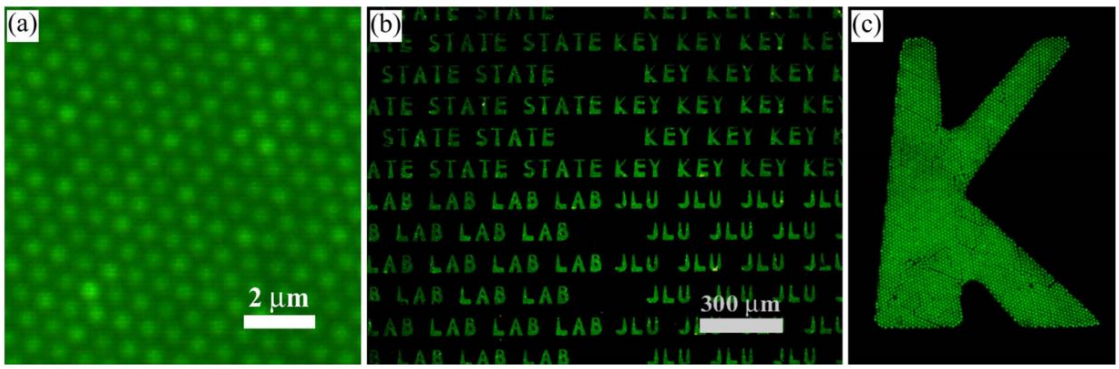

Figure 2.20: Polymer brush patterns mediated DNA sensing system. (a) Fluorescence image of the DNA nano-cone arrays with the period of 620 nm after binding the FITC-conjugate complementary oligonucleotide; (b) fluorescence image of hierarchical DNA patterns after binding FITC-conjugate complementary oligonucleotide. (c) The enlarged fluorescence photograph of the DNA pattern in image.[37]

2.2.1.3 Cell Isolation and Sensing

Another important sensing application of patterned surfaces is specific cell detection.[38,39] Cells, as the building block for organisms, have a great effect on the functions and behaviours of organisms, and there possess various kinds of cells with specific functions to support their daily lives. Just as each corn has two sides, there are also some bad cells which will cause detrimental diseases. For example, circulating tumor cells, a kind of cancer cells which break away from tumor or metastatic sites, circulating in peripheral systems as the original metastasis and providing facile assessment to all disease sites.[40,41] Thus, it is of great importance to detect and analyze such kind of bad cells and provide helpful information for disease status evaluation. Based on this, series of efficient platforms for specific cells in patient's blood sample identification have been successfully fabricated with common efforts in chemistry, material science and bioengineering.[42–44] And patterned surfaces have become an alternative system to sense different cells in a facile, real-time, and visible manner. Hsiao et al. prepared PEDOT (poly(3,4-ethylenedioxythio-phene) derivatives based rod arrays for the capture of circulating tumor cells with rod sizes ranging from micrometer to nanometer.[45]

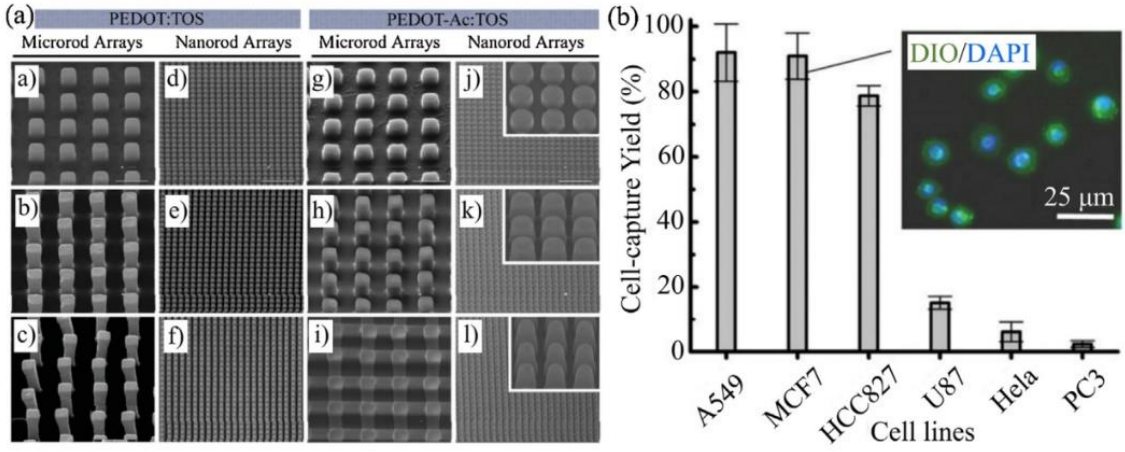

Figure 2.21: Specific cell sensing on patterned structures. (a) SEM images of PEDOT-based micro/nano-rod array films; (b) cell-capture efficiencies from suspensions of breast (MCF), lung (A549, HCC827), cervical (HeLa), prostate (PC3), and brain (U87) cell lines; inset: two-color fluorescence image based on DiO membrane (green) and DAPI nuclear staining.[45]

2.2.2 Thin Film Battery

Baggetto et al.[46] fabricated a honeycomb-structured Si film on planar TiN-covered Si substrate by photoetching. After lithiation, the honeycombs became highly curved (Fig. 24a). The thickness, length and height of the curved wall all increased compared with the starting material. Figure 2.22 (b) illustrates the morphological changes during delithiation. Interestingly, the

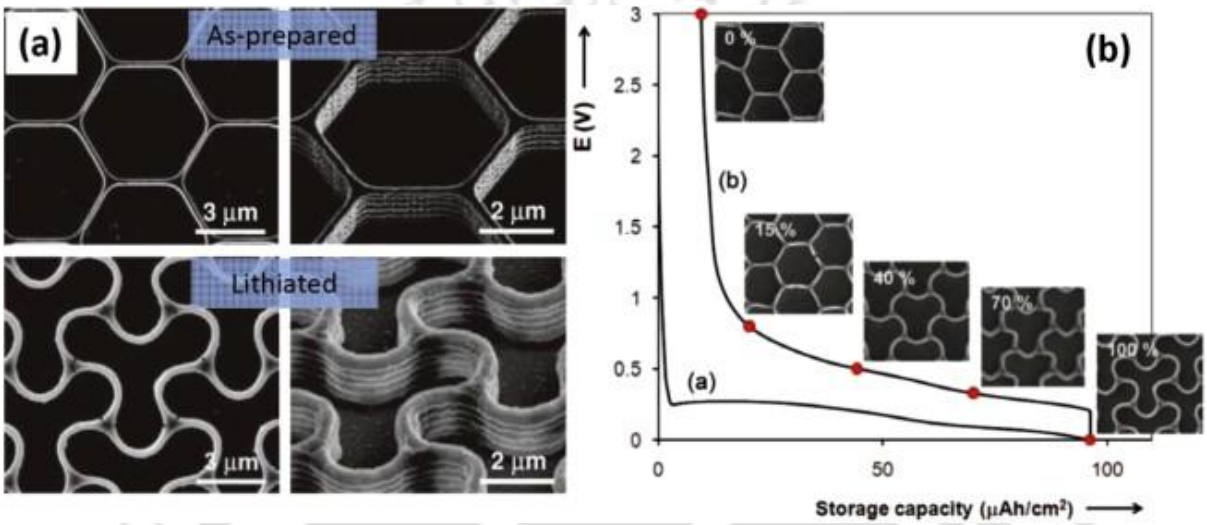

Figure 2.22: (a) SEM images of the as-prepared and fully lithiated Si honeycombs; (b) morphological changes of the Si honeycomb structure during delithiation.[46]

highly curved structure gradually converted back to its original configuration, and the hexagonal honeycombs were recovered finally, with exhibiting only slight deformation.

2.3 Knowledge Gap and Objectives of The Thesis

- Literature survey clearly shows that investigation is going on in the field of colloidal lithography to improve the process and its practical applicability. Colloidal lithography has its own limitation as there are lot of complexity in order to fabricate well-patterned surface with high resolution. A proper explanation of the evaporation process and how the suspended particles deposit at the contact line is still a mystery.

- Some novel methods have been developed to get the patterned surface in a microscale. Fabrication of a specific pattern on a large scale with colloidal lithography process is complicated.
- So far, very few reports on fabricating polymeric micro/nano-threads have been published. Most of the literature is on colloidal suspension. Here we attempt to fabricate micro/nano-threads of only polymers.

In contrast to the previous studies of literature and knowledge gap, we are proposing some methods to fabricate patterned polymer surface and their applications, and those are as follows

- Dynamic Contact Line Lithography: Template-less Complex Meso-Patterning with Polystyrene and Poly(methyl methacrylate).
- Janus Micro-thread to Micro-nanodroplets Using Dynamic Contact Line Lithography.
- Solvent Assisted Dewetting of PMMA Thin Film and PS Micro-thread: Fabricated by Dynamic Contact Line Lithography.
- Self-assembled PVDF Micro-threads with β-phase Crystallinity; Induced by Dynamic Contact Line Lithography Coupled with Electric Field.

Concisely, in the present thesis, objectives are distributed into four chapters, along with future scopes of the works. A detailed list of publications has been provided at the end of the document.

References

[1] F. Shao, T. W. Ng, J. Efthimiadis, A. Somers, W. Schwalb, *J. Colloid Interface Sci.* **2012**, *377*, 421.

[2] F. F. Shao, A. Neild, T. Alan, *Colloids Surfaces A Physicochem. Eng. Asp.* **2012**, *398*, 64.

[3] W. D. Ristenpart, P. G. Kim, C. Domingues, J. Wan, H. A. Stone, *Phys. Rev. Lett.* **2007**, *99*, 1.

[4] H. Hu, R. G. Larson, *J. Phys. Chem. B* **2006**, *110*, 7090.

[5] H. Gelderblom, Á. G. Marín, H. Nair, A. Van Houselt, L. Lefferts, J. H. Snoeijer, D. Lohse, *Phys. Rev. E - Stat. Nonlinear, Soft Matter Phys.* **2011**, *83*, 1.

[6] P. J. Yunker, T. Still, M. A. Lohr, A. G. Yodh, *Nature* **2011**, *476*, 308.

[7] J. C. Loudet, A. G. Yodh, B. Pouligny, *Phys. Rev. Lett.* **2006**, *97*, 1.

[8] J. C. Loudet, A. M. Alsayed, J. Zhang, A. G. Yodh, *Phys. Rev. Lett.* **2005**, *94*, 2.

[9] N. Bowden, F. Arias, T. Deng, G. M. Whitesides, *Langmuir* **2001**, *17*, 1757.

[10] A. B. D. Brown, C. G. Smith, A. R. Rennie, *Phys. Rev. E - Stat. Physics, Plasmas, Fluids, Relat. Interdiscip. Top.* **2000**, *62*, 951.

[11] B. Madivala, J. Fransaer, J. Vermant, *Langmuir* **2009**, *25*, 2718.

[12] B. Madivala, S. Vandebril, J. Fransaer, J. Vermant, *Soft Matter* **2009**, *5*, 1717.

[13] B. J. Park, E. M. Furst, *Soft Matter* **2011**, *7*, 7676.

[14] J. B. Fournier, P. Galatola, *Phys. Rev. E - Stat. Nonlinear, Soft Matter Phys.* **2002**, *65*, 1.

[15] H. Yabu, M. Shimomura, *Adv. Funct. Mater.* **2005**, *15*, 575.

[16] P. Kumnorkaew, Y. Ee, N. Tansu, J. F. Gilchrist, *Langmuir* **2008**, *24*, 12150.

[17] K. Viswanathan, N. K. Sundaram, *Wear* **2017**, *376–377*, 1271.

[18] H. Bodiguel, **2010**, *26*, 10758.

[19] W. Sun, F. Yang, *Langmuir* **2014**, *30*, 6548.

[20] M. Fais, R. Karamanska, D. A. Russell, R. A. Field, *J. Cereal Sci.* **2009**, *50*, 306.

[21] H. Kong, D. Liu, S. Zhang, X. Zhang, *Anal. Chem.* **2011**, *83*, 1867.

[22] G. Chang, Y. Mori, S. Mori, T. Irie, H. Nagai, T. Goto, Y. Tatsu, H. Imaishi, K. Morigaki, *Anal. Chem.* **2012**, *84*, 5292.

[23] L. Baldini, A. J. Wilson, J. Hong, A. D. Hamilton, *J. Am. Chem. Soc.* **2004**, *126*, 5656.

[24] Y. Liu, W. Hu, Z. Lu, C. M. Li, *ACS Appl. Mater. Interfaces* **2014**, *6*, 7728.

[25] Y. Zhao, X. Zhao, X. Pei, J. Hu, W. Zhao, B. Chen, Z. Gu, *Anal. Chim. Acta* **2009**, *633*, 103.

[26] Z. Wu, P. Yang, *Adv. Mater. Interfaces* **2015**, *2*, 1.

[27] M. J. Linman, H. Yu, X. Chen, Q. Cheng, *ACS Appl. Mater. Interfaces* **2009**, *1*, 1755.

[28] K. J. Son, S. Kim, J.-H. Kim, W.-D. Jang, Y. Lee, W.-G. Koh, *J. Mater. Chem.* **2010**, *20*, 6531.

[29] K. Nam, K. Eom, J. Yang, J. Park, G. Lee, K. Jang, H. Lee, S. W. Lee, D. S. Yoon, C. Y. Lee, T. Kwon, *J. Mater. Chem.* **2012**, *22*, 23348.

[30] H. Wang, Q. Xu, L. Shang, J. Wang, F. Rong, Z. Gu, Y. Zhao, *Chem. Commun.* **2016**, *52*, 3296.

[31] D. R. Walt, *Lab Chip* **2014**, *14*, 3195.

[32] X. Zhang, Z. Li, S. Ye, S. Wu, J. Zhang, L. Cui, A. Li, T. Wang, S. Li, B. Yang, *J. Mater. Chem.* **2012**, *22*, 8903.

[33] C. A. Mirkin, *ACS Nano* **2007**, *1*, 79.

[34] J.-H. Lim, D. S. Ginger, K.-B. Lee, J. Heo, J.-M. Nam, C. A. Mirkin, *Angew. Chemie Int. Ed.* **2003**, *42*, 2309.

[35] R. Duan, X. Zuo, S. Wang, X. Quan, D. Chen, Z. Chen, L. Jiang, C. Fan, F. Xia, *J. Am. Chem. Soc.* **2013**, *135*, 4604.

[36] R. Schlapak, J. Danzberger, D. Armitage, D. Morgan, A. Ebner, P. Hinterdorfer, P. Pollheimer, H. J. Gruber, F. Schäffler, S. Howorka, *Small* **2012**, *8*, 89.

[37] W. Liu, X. Liu, P. Ge, L. Fang, S. Xiang, X. Zhao, H. Shen, B. Yang, *ACS Appl. Mater. Interfaces* **2015**, *7*, 24760.

[38] A. Bajaj, O. R. Miranda, R. Phillips, I. B. Kim, D. J. Jerry, U. H. F. Bunz, V. M. Rotello, *J. Am. Chem. Soc.* **2010**, *132*, 1018.

[39] C. Siltanen, D. S. Shin, J. Sutcliffe, A. Revzin, *Angew. Chemie - Int. Ed.* **2013**, *52*, 9224.

[40] S. Wang, H. Wang, J. Jiao, K. J. Chen, G. E. Owens, K. I. Kamei, J. Sun, D. J. Sherman, C. P. Behrenbruch, H. Wu, H. R. Tseng, *Angew. Chemie - Int. Ed.* **2009**, *48*, 8970.

[41] M. Lin, J. F. Chen, Y. T. Lu, Y. Zhang, J. Song, S. Hou, Z. Ke, H. R. Tseng, *Acc. Chem. Res.* **2014**, *47*, 2941.

[42] Y. Y. I. Amin, K. Runager, F. Simoes, A. Celiz, V. Taresco, R. Rossi, J. J. Enghild, L. A. Abildtrup, D. C. E. Kraft, D. S. Sutherland, M. R. Alexander, M. Foss, R. Ogaki, *Adv. Mater.* **2016**, *28*, 1472.

[43] S. Zhao, H. Zhao, X. Zhang, Y. Li, Y. Du, *Lab Chip* **2013**, *13*, 2350.

[44] F. Zhang, Y. Jiang, X. Liu, J. Meng, P. Zhang, H. Liu, G. Yang, G. Li, L. Jiang, L. J. Wan, J. S. Hu, S. Wang, *Nano Lett.* **2016**, *16*, 766.

[45] Y. S. Hsiao, S. C. Luo, S. Hou, B. Zhu, J. Sekine, C. W. Kuo, D. Y. Chueh, H. H. Yu, H. R. Tseng, P. Chen, *Small* **2014**, *10*, 3012.

[46] L. Baggetto, D. Danilov, P. H. L. Notten, *Adv. Mater.* **2011**, *23*, 1563.

Chapter 3

Dynamic Contact Line Lithography: Template-less Complex Meso-Patterning with Polystyrene and Poly(methyl methacrylate)

This page is left blank intentionally

Abstract

Micro/nanopatterning on a 2D surface is apt for cutting-edge miniaturization technology, which directly or indirectly requires high-end expensive lithographic tools. The evaporative deposition at the receding contact-line of a polymer solution, termed as Dynamic Contact Line Lithography (DCLL), can be a potential inexpensive technique for template-less meso-patterning. The desired morphology can be achieved if the deposition patterns from DCLL can be predicted a priori. A deposition map (morphological zone diagram) from the myriads of patterns is constructed in terms of contact-line velocity and the polymer concentration. Specifically, two combinations: polystyrene (PS)/cyclohexane and poly (methyl methacrylate) (PMMA)/toluene are used to show the generic nature of the zone diagrams. The surface wettability of Si (water contact angle, CA ~ 15°) is tuned from CA ~ 35° to ~ 98° by patterning with DCLL. Directed by the zone diagrams, fabrication of a complex rectangular cross-pattern of PS and PMMA micro-threads with a periodicity of ~ 65 μm and ~ 50 μm respectively on a Si surface is demonstrated to establish the robustness and potential of the DCLL and predictive zone diagram.

3.1 Introduction

Surface modification by coating with functional materials is essential nowadays in various industrial applications. Some of the coating techniques are complex and involve sophisticated equipment aiming at specific applications such as anti-reflective lens,[1] frictionless surfaces,[2–4] photovoltaic applications,[5] etc. However, some of the applications such as super-hydrophobicity,[6,7] reversible adhesive,[8] sensors,[9,10] micro-lens arrays to improve the efficiency of LED,[11] optofluidics,[12] solar cell,[13] biomedical applications,[14] etc. can be achieved simply by facile, inexpensive techniques mostly relying on self-assembly of materials. One such technique is the natural evaporative deposition of particles from a solution

* This Chapter is published in *Journal of Colloid and Interface Science*, **2021**, 601, 156 – 166

droplet, where the particles are dragged towards the pinned contact line due to the Marangoni flow induced by the higher evaporation rate of the solvent near the contact line and form a "coffee ring".[15] Realizing its potential application in inkjet printing, microfabrication, biomedical, and electronic printing, in the last few decades, this problem is studied extensively aiming to control the deposition patterns from coffee ring to disk-like deposition.[16–19] The evaporative deposition pattern from a stationary solution droplet can be influenced by the concentration of the particles, controlled Marangoni flow induced by temperature of the substrate,[20] or by the presence of a volatile solvent source.[19] Unlike a stationary droplet, by drawing the solution meniscus away from the contact line at a regulated speed, the controlled deposition of particles has been made continuous, often known as blade coating or doctor-blade.[21] In this process, the colloidal solution is arrested between the deposition blade and the substrate due to the capillary force. The speed of the contact line on the substrate is maintained by controlling the relative motion of the deposition blade and the substrate while driving any one or both. This convective flow deposition technique experimentally and theoretically was investigated for colloidal particles,[11,22–26] as well as for polymer,[27–29] or organic molecules.[30,31]

Formation of micro/nanostructure from convective flow deposition of a polymer solution is associated with dewetting of the thin liquid film, stick-slip phenomena, and fingering instability, originating from the Marangoni stress near the contact line.[32] Another surrogate technique is the solvent evaporation-induced pattern formation from a precast polymer thin film.[33, 34] Deblais *et al.* have demonstrated that using the contact line instability of non-Newtonian fluid, slender liquid micro-filament can be formed in the orthogonal direction to the contact line and this can be used for particle sorting or stretching of DNA molecules.[35] These self-assembled evaporative patterns are highly sensitive to the deposition conditions such as solvent evaporation rate, polymer, substrate, the gap distance between the deposition blade and

the substrate, speed of the contact line, temperature, etc. but can be reproducible at identical conditions. Deposition characteristics changes depending on the radius of curvature of the liquid meniscus, substrate, or blade surface energy.[11] Yabu *et al.* have also demonstrated that different morphology such as stripes, ladders, droplets can be deposited on a substrate by tuning the system parameters.[27] To date, there is no guidance available for a predictive deposition following this method. As these regular patterns are reproducible at controlled conditions, this can be used as a template-less patterning technique, if only, one can foretell the deposition pattern a priori depending on the process parameters.

In this report, we uncover the generic predictive nature of the controlled evaporative deposition by constructing the morphological phase diagram for such template-less micro-patterning as a function of polymer concentration and stage velocity. Two common polymer solutions polystyrene (PS) in cyclohexane and poly (methyl methacrylate) (PMMA) in toluene are used in this study. Although toluene is a good solvent for both PS and PMMA, the two different solvents cyclohexane and toluene are chosen for the experiments to identify the generic nature of the deposition patterns for both high (cyclohexane) and low (toluene) volatile solvents. Guided by the predictive morphological zone diagrams of the deposition from two polymer-solvent systems, a complex long-range micro-striped pattern of binary polymer is also fabricated which is quite challenging to achieve by any other method other than a short-range ordered arrangement by self-assembly.[36]

3.2 Experimental Section

3.2.1 Materials

The materials used for the experiment were polystyrene (Mw – 192000, Sigma Aldrich), poly (methyl methacrylate) (Mw – 120000, Sigma Aldrich), cyclohexane (Extrapure AR, Sisco Research Laboratory), and toluene (rectified 99%, Loba Chemie). Polymers with moderate

molecular weight were chosen to probe the variety of deposition patterns (discussed later) at different concentrations. The solubility of PS in cyclohexane is 3.9×10^{-4} mol L^{-1} and that of PMMA in toluene is 5.8×10^{-4} mol L^{-1}. A stainless-steel blade (Gillette) was purchased from a local vendor and a p-type one-sided polished silicon wafer with an orientation of <100>, was procured from Macwin India.

3.2.2 Preparation of Solution and Sample

We used the solution of polystyrene (PS) and poly (methyl methacrylate) (PMMA) in cyclohexane and toluene, respectively, for this experiment. The polymers were dissolved in respective solvents at room temperature ($\sim 23°C$) with continuous stirring for six hours. The concentration of PS and PMMA were varied from 0.05 g L^{-1} to 0.6 g L^{-1} and from 0.5 g L^{-1} to 2 g L^{-1} respectively. It is important to note that the diffusion coefficient (D_p) of both the polymer molecules in the selected solvents are of the same order (PS in cyclohexane is $\sim 3.04 \times 10^7$ cm^2 s^{-1} and PMMA in toluene is $\sim 5.80 \times 10^7$ cm^2 s^{-1} at a room temperature of 23 °C).[37] Silicon wafers were cut into pieces of dimension 1 cm x 2 cm, and before the experiments, were cleaned with piranha solution (a mixture of sulphuric acid and hydrogen peroxide in 4: 1 ratio), followed by rinsing with de-ionized water (Elix-3, Milli-Q; Millipore, USA). After cleaning, the silicon substrates were dried under a nitrogen stream. The dried Si wafer was then fixed on a goniometer (GN05/M, Thorlabs Inc) for precise control of the substrate leveling. The whole set-up was mounted on a custom-made movable stage.

3.2.3 Characterization

The prepared polymer solution was checked with a particle size distribution (PSD) analyzer (Delsa Nano C Particle Analyzer by Beckman Coulter) to ensure that there is no filler particles or globules in the solution. The movement of the contact line during deposition was

observed by a high-speed camera (Basler Pilot piA640-210gc Color Camera) and the optical image of the deposition was recorded using a bright field microscope (Axio Scope.A1 MAT HAL 100). The contact angle (CA) of a 3 µl water droplet placed on the deposited polymer pattern was measured using a contact angle goniometer and associated software (Holmarc, HO-IAD-CAM-01B).

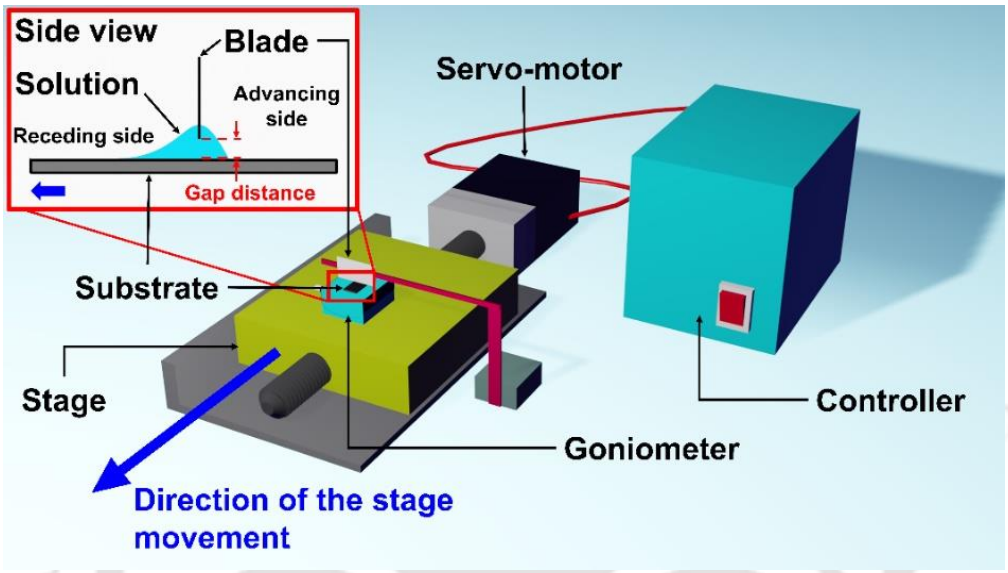

Figure 3.1. A schematic of the experimental setup and its components for dynamic contact line lithography (DCLL). The inset diagram depicts a decrease of the receding contact angle by dragged meniscus due to stage movement.

3.3 Results and Discussion

3.3.1 Dynamic Contact Line Lithography (DCLL)

Figure 3.1 shows the schematic of the experimental setup to deposit polymer micro/nano features on a substrate. A cleaned silicon substrate was fixed on a custom-made stage, which was driven horizontally by a servo motor. A stationary stainless-steel blade (Gillette Blade) was attached to a holder, such that the blade firmly hung over the Si substrate vertically, maintaining a narrow gap of ~ 200 µm between the substrate and the blade tip. The narrow

gap was ensured by taking an optical image of the arrangement and subsequently measuring the gap. At this juncture, we would also like to mention that this gap distance affects the hydrodynamic flow behavior of the polymer solution that marginally alters the morphological zone diagram (discussed later). 20 µl of a polymer solution of different concentrations was dispensed into the gap between the blade and the Si wafer surface.

Initially, at the stationary condition of the stage, the polymer solution symmetrically distributed to both sides of the blade and the solution made a stationary CA of $\theta_s \approx 8^\circ$ ($\theta_s \approx 7^\circ$) with the substrate at both sides of the blade when toluene (cyclohexane) was used. Upon initiation of the stage motion, the CA differed to advancing (higher than the θ_s) and receding (lower than the θ_s) contact angle at the front and rear contact line, respectively. The deposition of the polymer took place at the rear contact line. This narrow gap between the blade and the substrate perfectly held the solution because of the capillary force and the drop meniscus was dragged on the substrate along with the blade while the stage was moving. The velocity of the stage along with the substrate was controlled mechanically by a motor. For a particular experiment, stage velocity was kept constant. Although the instantaneous speed of the contact line motion varied intermittently in a time-periodic manner due to stick-slip phenomena, the average velocity of the contact line was dictated by the stage velocity in the opposite direction. Thus, for simplicity, hereafter, we will denote the stage speed as the speed of the contact line. The contact line speed was varied from 20 µm s^{-1} to 100 µm s^{-1}.

Three distinguishable deposition regimes were identified – i) initial unsteady deposition, ii) intermediate steady deposition, and iii) final unsteady deposition. Unsteady situations instigated because of the interplay between unsteady evaporation of solvent and speed of contact line (regime (i)), and due to high local concentration fluctuation at the end part of the experiment (regime (iii)). The deposition patterns become irregular in these unsteady regimes.

In this report, we will restrict our discussion only on the quasi-steady state deposition, the middle part of the deposition pattern (regime (ii)). As the experiments were carried out in a controlled environment with a temperature of $\sim 25\ ^{\circ}C$ and at a relative humidity of $\sim 68 \pm 2\ \%$, negligible disturbance from the surroundings was expected to affect the evaporation rate of the solvent and the deposition pattern.

At the receding contact line, due to very low contact angle and the higher evaporation rate,[15] three interesting phenomena occurred simultaneously:

i) The local concentration of polymer increased near the contact line due to a higher evaporation rate.

ii) Polymer micro/nano-thread deposited at the receding contact line. A thin film of the polymer solution was formed and get pinned at the deposited thread as the substrate was in motion.

iii) The detachment of the thin liquid film from the pinned contact line took place as soon as the pinning force was overcome by the restoring force.

This restoring force ($\gamma_{sl} + \gamma_l \cos\theta$) increased with time due to a decrease in the contact angle θ while pinned contact line was dragged by the moving stage. γ_{sl} and γ_l are the solid-liquid interfacial tension and surface tension of the liquid, respectively. Except at a very low stage velocity when the evaporation time scale was comparable to the deposition time scale (one can compare the colloidal deposition from a stationary sessile drop scenario as an asymptotic limit), the decrement in the contact angle was predominantly due to the dragging of the pinned contact line by the moving stage. This increasing restoring force when exceeded the substrate surface tension (γ_s) and the pinning force per unit length of the contact line (F_{pin}), the contact line detached and sprang back to a new pinning site.[38–40] Thus, pinning and de-

pinning took place time periodically. We call this time-periodic deposition 'dynamic contact line lithography' (DCLL). The concentration of the polymer and the speed of the contact line were systematically varied to investigate the deposition from dynamic contact line lithography (DCLL).

To capture the pinning and de-pinning events of a contact line, a high-speed camera was used to record the contact line motion at 210 fps. First, the deposition of PMMA thread from toluene (concentration $1\ g\ L^{-1}$) was observed while the speed of the contact line was maintained at $40\ \mu m\ s^{-1}$. As the toluene evaporation rate is relatively slower compared to cyclohexane, the pinned contact line was found to be relatively uniform and straight (Figure 3.2, top panel (a_1) to (a_4)).

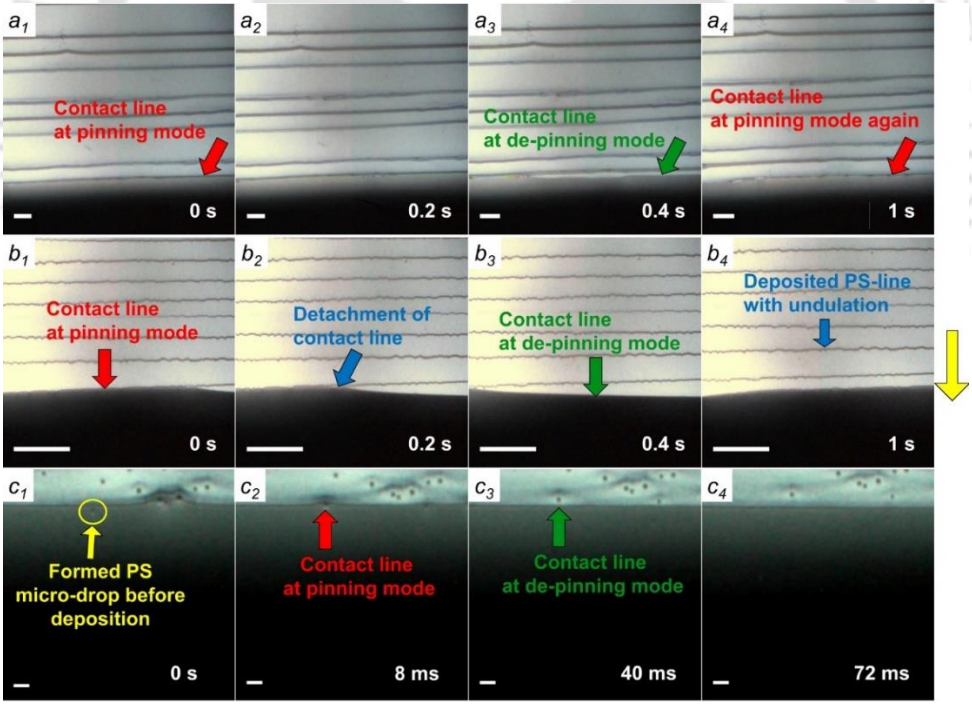

Figure 3.2. (Color online) (a_1) to (a_4) are the optical images at different timescale during deposition of PMMA from toluene ($1\ g\ L^{-1}$) at stage speed of $40\ \mu m\ s^{-1}$, (b_1) to (b_4) represent the deposition process of the undulated line of PS from cyclohexane ($0.1\ g\ L^{-1}$) at the stage speed of $40\ \mu m\ s^{-1}$. (c_1) to (c_4) are the optical images at different times of deposited PS micro-globules from cyclohexane ($0.4\ g\ L^{-1}$) at the stage speed of $100\ \mu m\ s^{-1}$. All the scale bars of a_1 – a_4 and b_1 – b_4 represent 100 µm and the scale bars of c_1 – c_4 represent 10 µm. The downward yellow arrow (right side) represents the direction of the contact line motion.

On the other hand, at the same contact line speed, the pinned contact line of PS in cyclohexane (concentration 0.1 g L^{-1}) was undulated (Figure 3.2, middle panel (b_1) to (b_4)). In both cases, the de-pinning process started from one side of the pinned contact line and then propagated along the deposited thread line just like a crack opening. The deposition of PS from cyclohexane was also associated with another interesting phenomenon. Once the contact line was detached from the deposited polymer thread, initially it retreated, then swung back again toward the already deposited polymer thread direction to some extent (see the gap between the detached contact line and the adjacent deposited thread at the right side of Figure 3.2 (b_3) and 2(b_4), only to deposit the next polymer micro-thread on the surface. During this advancement of the contact line, the polymer solution wetted the surface non-uniformly due to the surface defects along with the fluctuation of local polymer concentration that gave rise to the undulated contact line. This contact line instability [33] resulted in an undulated deposition. At a relatively higher speed of the contact line and higher concentration of the polymer, this undulation was reduced (shown later).

Interestingly, at a relatively moderate concentration of PS in cyclohexane (0.4 g L^{-1}) and a high contact line velocity of 100 μm s^{-1}, PS micro-globules, instead of micro-threads, were deposited (Figure 3.2 lower panel (c)). Moderate average concentration, relatively high stage speed, and high evaporation rate of cyclohexane (and hence the low temperature of the solution) induced local concentration fluctuation. The solubility of PS in cyclohexane being less, the local concentration fluctuation randomly surpassed the solubility thus rendered micro-globule formation due to the aggregation of the interchain association of the PS within the solution near the contact line.[41] Receding contact line facilitated the deposition of the formed micro-globules. The average diameter of the micro-globules was ~ 2 μm. It was verified using the PSD analyzer that there was no globule formation in the bulk of the PS-cyclohexane

solution. Continuing deposition experiments with higher bulk polymer concentrations at the same stage speed, PS micro-threads having a short length (or can be called the sporadic micro-threads) due to partial pinning was obtained.

3.3.2 Morphological Zone Diagram

Figure 3.3 shows the typical deposition patterns from PS-cyclohexane (Figure 3.3, (a) – (f)) and PMMA-toluene (Figure 3.3, (g) – (l)) solutions at a few selected representative concentrations and stage velocities. Other deposition patterns from polymer solutions having different concentrations and at different contact line velocities. In general, PS micro-threads from cyclohexane are more undulated and associated with more irregularities than PMMA threads from toluene. This can be attributed to the more volatility of cyclohexane (saturated vapor pressure $P_{CH}^{Sat} = 97.59\ \text{mmHg}$ at $25\ °C$),[42] compared to that of toluene ($P_{Tol}^{Sat} = 28.529\ \text{mmHg}$ at $25\ °C$).[43] As rapid evaporation of cyclohexane took place near the contact line, the local cooling because of penalty for heat of evaporation of the liquid induced a temperature gradient along the curved meniscus. This temperature gradient instigated Marangoni flow into the bulk and induced local fluctuations in the polymer solution. It is often observed that particles in a sessile colloidal droplet do not have sufficient time to redistribute and organize during deposition due to the small time scale of evaporation associated with a solvent having high volatility.[19] Here also, near the contact line, higher volatility prompted a sudden rise of the local polymer concentration which in turn induced local concentration fluctuation near the contact line.

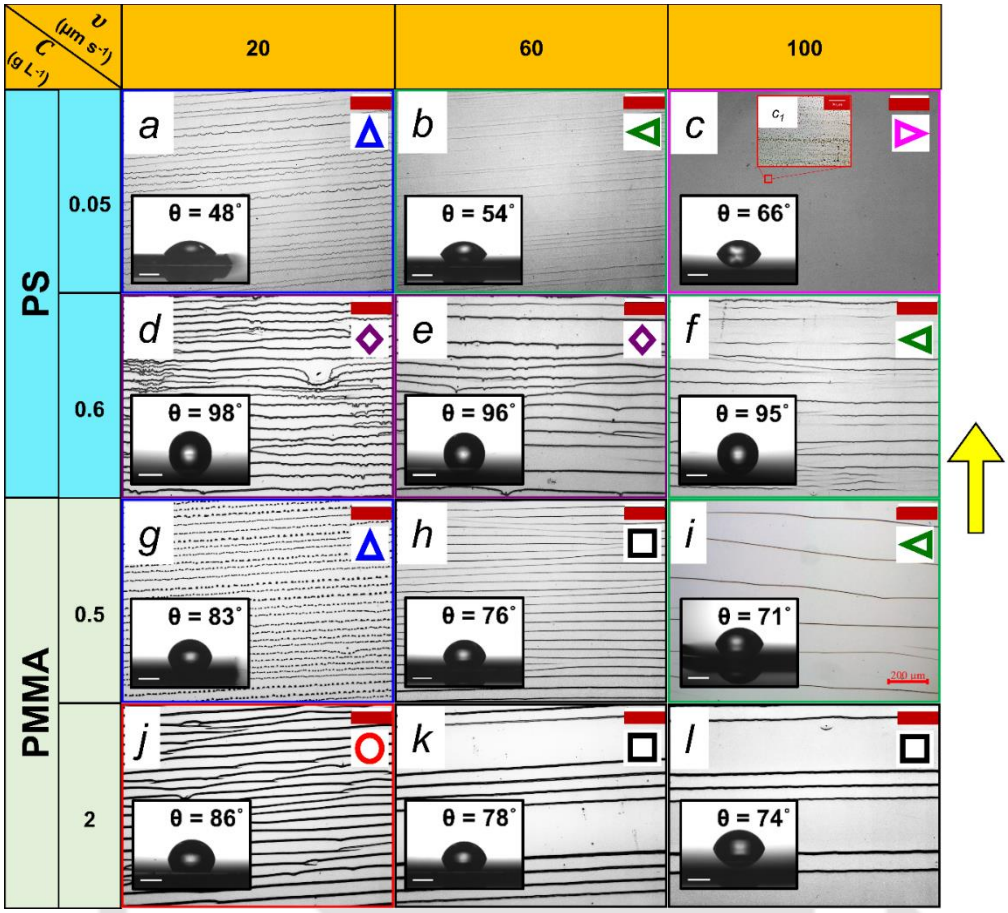

Figure 3.3. (Color online) The micro patterns of deposited PS from cyclohexane (a-f) and PMMA from toluene (g-l) at different concentration and contact line velocity: (a) sparse undulated pattern, (b) line with partial pinning, (c) nanodroplet, (d), (e) – undulated lines with branching and pinning (f) lines with partial pinning. (g) extreme undulation instability leads to droplet-like appearance, (h) straight line, (i) lines with partial pinning, (j) lines with branching, (k), (l)- straight lines with intermittent 'missed out' lines. Optical images of 3 µl water droplets on these structured surfaces are depicted in the inset with contact angle stamped on the image. The symbol at the top right corner of each frame corresponds to different zones in the zone diagram discussed later in the text and Figure 3.4. The scale bar of primary images corresponds to 200 µm and that of the insets (water contact angle) depicts 1 mm. The magnified image (c1) of Figure (c) has a scale bar of 50 µm. The yellow arrow represents the direction of a moving contact line.

The random formation of concentrated polymer globules-like structures due to concentration fluctuation also imparted some defects on the surface. These defects became the pinning sites during the final thread-like deposition and generated "undulations with branches" (Figure 3.3 (d), (e)). Apart from these defects, the contact line also underwent instability caused

by the unstable ridge formation due to Rayleigh instability. At a low stage speed, the instability time scale for the undulations was comparable to the deposition time scale. However, these irregularities, as well as undulation, decreased with the increasing stage speed due to the shorter deposition time scale (discussed later). At the high stage speed, for the low concentrated solution, partial pinning with incomplete thread ("line with partial pinning") was observed. On the other hand, with relatively higher concentration, and with a less volatile solvent (which alleviated the concentration fluctuations) in the case of the PMMA-toluene system, the micro-threads obtained were quite straight and regular. At a relatively low velocity of the contact line and high concentration of PMMA, due to pinning at defects, 'branching' of the lines was observed (Figure 3.3 (j)).

The 'pinning' was reduced and the undulation of threads became prominent (Figure 3.3 (a) and (g)) at a relatively low concentration of polymer. In general, PMMA melt has preferential interaction with native oxide layer of Si wafer (SiO_2) over PS.[36,44] Thus, one can expect a stable PMMA thread compared to the PS. However, in this case, continuous undulated PS thread (Figure 3.3 (a)) and seemingly isolated droplets of PMMA (Figure 3.3 (g)) were obtained. A close inspection revealed that these isolated droplets-like structures were faintly connected with a very thin line of PMMA. The polymer solutions being of low concentration, initially formed stable undulated micro-thread of the solution on SiO_2 ($\gamma_{SiO_2} \approx 64.7\ mJ/m^2$).[45] At this juncture, it should be noted that the surface tension of cyclohexane ($\gamma_{CH} \approx 24.9\ mN/m$) and toluene ($\gamma_{Tol} \approx 28.4\ mN/m$) are much smaller than high energy SiO_2 surface. The undulated liquid PMMA/toluene solution threads eventually with time underwent Rayleigh-Plateau like instability and disintegrated into small droplets. But for the PS/cyclohexane system, due to the higher evaporation rate of the cyclohexane, the undulated threads did not get enough time to undergo Rayleigh instability and deposited as the undulated polymer micro-thread. On the other hand, the PMMA/toluene system, due to the slow

evaporation rate of toluene, the undulated micro-threads of PMMA/toluene got sufficient time to undergo Rayleigh instability and broke up into small polymer droplets. At high velocity of the stage, due to large mass transfer area provided by the extended liquid meniscus, the solvent evaporated rapidly thus formed stable micro-threads (Figure 3.3 (i)) of PMMA. On the other hand, PS concentration being very low, the rapid evaporation of the cyclohexane induced thin film dewetting thus formed dewetted microstructures of PS all over the surface (Figure 3.3 (c)). The period or separation distance between two consecutive micro-threads is defined as the wavelength (λ) of the deposition. At a high concentration of PMMA and moderate to high contact line velocity, intermittently, the formation of micro-thread was 'missed out' from the periodic deposition (Figure 3.3 (k), (l)). A thread-like deposition initiates when the local concentration near the contact line exceeds a threshold value (~solubility of the polymer). Then the contact line gets pinned in that location due to deposition of the polymer and eventually with time, forms a polymer micro-thread. As long as the liquid meniscus is attached with the deposited thread, the polymer deposits and the liquid film (or liquid bridge) gradually get thinner in between the deposited micro-thread and the bulk liquid meniscus. When the liquid film is thin enough to instigate rupture, the bulk liquid meniscus, associated with the vertical blade, snaps back like a spring to a new equilibrium position and starts depositing again. The other part of the ruptured thin liquid polymer film associated with the rear side of the deposited thread starts to dewet the substrate (discussed later). Sometimes the liquid meniscus remains pinned at a deposited thread for a longer time. This longer pinning time is also associated with the local polymer concentration fluctuations. After the deposition of every 3 or 4 threads, the local polymer concentration is relatively depleted and renders a stable liquid bridge that connects the deposited thread and bulk meniscus attached to the blade. This increases the separation between the deposited thread and the moving blade position and thus increases the distance to the equilibrium position to initiate new deposition. This appears as a 'missed out'

thread in the overall deposition pattern. The thicker deposition of polymer micro-thread just before the 'missed out' position compared to other regular micro-threads, confirms the longer pinning time and supports this explanation (Figure 3.3 (k), (l)).

Based on the different types of deposition patterns, e.g. lines, undulated lines, lines with branches, lines with pinning, etc., due to the variation of contact line velocity and concentration of polymers, a morphological zone diagram was constructed and shown in Figure 3.4. For the PS-cyclohexane system, low polymer concentration and low contact line velocity promoted micro-thread with undulation which was the manifestation of fingering instability observed at a much lower velocity (Figure 3.4 (a)). The high evaporation rate of cyclohexane induced Marangoni stresses near the contact line, thus initiated the finger-like structure.[32]

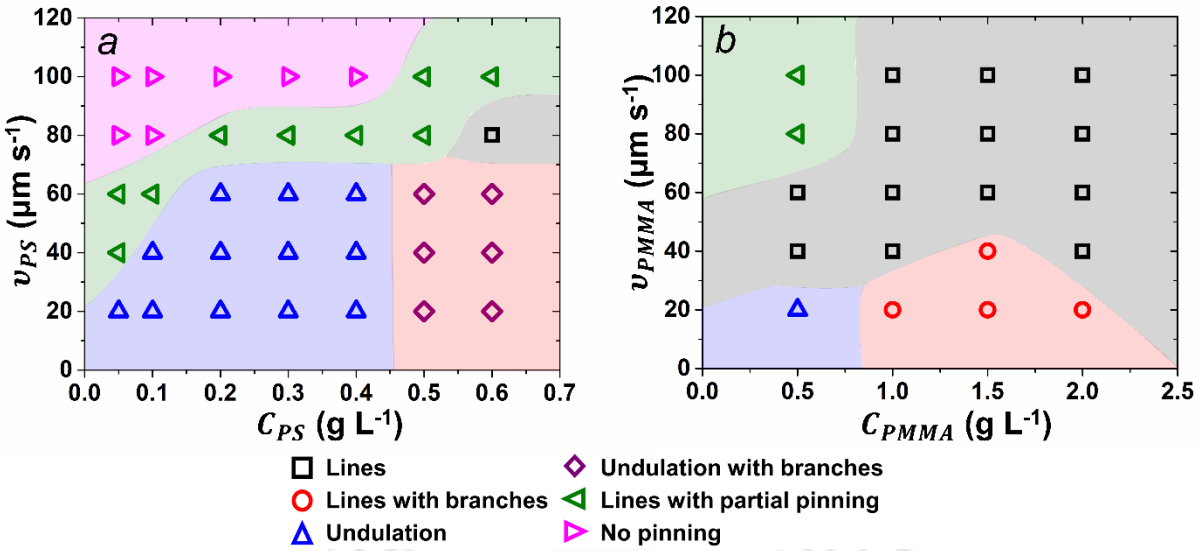

Figure 3.4. (Color online) Morphological zone diagrams of (a) PS and (b) PMMA from cyclohexane and toluene, respectively, in terms of different velocities (v) of the contact line and different concentrations of polymers. Undulation (up triangle, blue), lines with partial pinning (left triangle, green), and no pinning (right triangle, magenta) are mostly visible at low to moderate concentration of PS with increasing contact line velocity. Higher concentrated solutions at lower velocities of contact line deposit thick undulated lines with branches (diamond, deep purple). At a moderately high velocity of 80 µm s^{-1} and high concentration nearly perfect straight line (square, black) deposition is obtained. For PMMA, a larger zone for straight lines (square, black) is obtained for a low to a high concentration and at a moderate to high contact line velocity. At a moderate to high concentration but at a low velocity however lines with branches (circle, red) are obtained.

Near perfect straight micro-threads or lines were obtained at a small 'sweet spot' of 0.6 g L^{-1} PS concentration and near about 80 µm s^{-1} contact line speed. Broken micro-threads due to partial pinning were observed at moderate to high contact line speed and at moderate to low concentration. No micro-thread deposition was observed at higher contact line velocity (80 − 100 µm s^{-1}) with low to moderate concentration (0.05 – 0.4 g L^{-1}), due to the lack of pinning at the contact line; rather, micro-nano polymer droplets were found to be deposited. This regime is termed as a "no pinning" regime in the morphological zone diagram (Figure 3.4 (a)). In the case of the PMMA-toluene system, the whole morphological zone diagram was spanning over a larger concentration domain, thus all the different domains discussed above were squeezed towards a lower concentration regime revealing the generic nature of the zone diagram. PMMA-toluene system depicts nearly perfect straight-line deposition, spanning over a large concentration range, shown by black squares in Figure 3.4 (b).

The rich phenomena at the three-phase contact line such as stick-slip dynamics, deposition at the contact line during the pinning stage, unzipping of the contact line, etc. are also observed in the case of colloidal flow deposition. The high local concentration of polymer near the contact line is analogous to the presence of particles in the case of a colloidal deposition system. For such a particle/carrier solvent system as well, one can identify and characterize the deposition patterns in terms of parameters such as concentration of particles and contact line velocity.

3.3.3 Deposition Pattern Characteristics

Figure 3.5 (a) depicts the wavelength (λ_d) of the deposited straight lines as a function of contact line velocity for PS and PMMA. The whole deposition process is a quasi-static phenomenon and deposition takes place at the contact line if the local concentration of the polymer, near the contact line, exceeds the solubility at the experimental temperature and the

polymer phase separates from the solution. The local concentration of the polymer near the contact line increases due to the higher evaporation rate of the solvent at that regime, and to replenish the evaporative loss, more solvent flows toward the contact line along with the polymer molecules present in the bulk.[46,47] Thus, the accumulation of polymer molecules takes place and eventually deposits as micro-threads on the substrate while the solubility threshold is reached. Once the micro-threads are deposited and the contact line detaches from the deposited thread, the local concentration of the polymer again becomes close to bulk concentration or probably slightly less than the bulk concentration due to excess solvent flow towards the contact line. The whole process then repeats in a time-periodic manner. We refer to this time period as an average deposition time scale t_d. The high velocity of the contact line, achieved by the fast stage velocity, facilitates faster evaporation of the solvent by providing a large area for the mass transfer. Assuming very thin liquid film formation near the contact line, the evaporative mass transfer area develops per unit length (m) of the contact line per s is $\upsilon\ m^2\ s^{-1}$, where υ being the contact line velocity with respect to the substrate in $m\ s^{-1}$ unit. At a high speed of the contact line motion and for low bulk concentration, local concentration fluctuation becomes high but due to low overall concentration, the polymer cannot accumulate as a thread, rather form micro-globules near the contact line and deposits while the solvent evaporates. The micro-thread deposition being more regular for PMMA/toluene system, we attempt to characterize the same by calculating the wavelength, λ_d. The deposition time scale t_d can be estimated from the following equations:

$$\lambda_d = \upsilon t_d, \quad \dots \quad \dots \quad \dots \quad \dots \quad \dots \quad \dots \quad \dots \quad \dots \quad \dots \quad (3.1)$$

It was found that the deposition time t_d is decreasing with the velocity of the contact line (Figure 3.5 (b)).

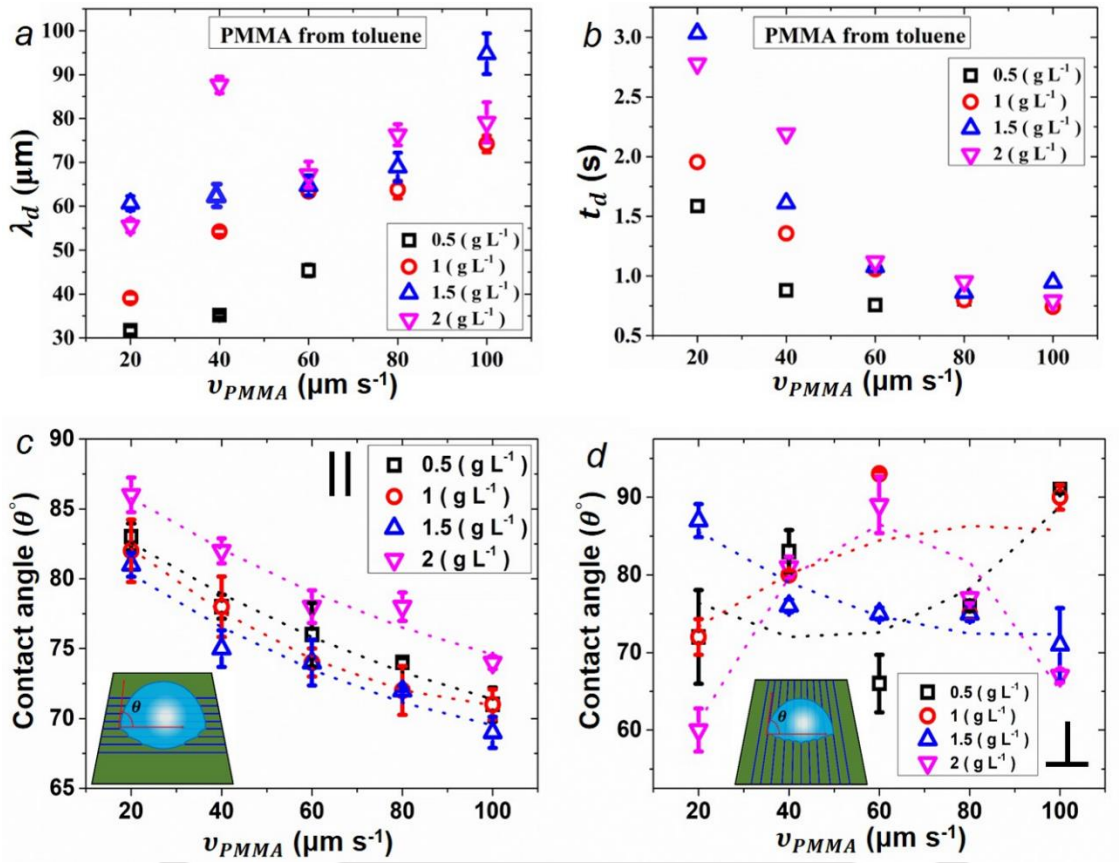

Figure 3.5. (Color online) (a) Characteristic wavelength of the deposition against the velocity of the contact line at different concentrations of the PMMA. (b) Estimated deposition time, t_d, from eq. 3.1 shows decreasing trend with the velocity of the contact line. (c), (d) represent the water contact angle in the parallel and perpendicular direction of the deposited PMMA micro-threads, respectively. Dotted lines in Figure (c)-(d) are meant to guide the eye.

3.3.4 Tuning Wettability

We aim to tune the wettability of a Si surface by depositing polymer microstructure by DCLL. The water contact angle on atomically smooth Si wafer is ~ 15˚ and that on flat PS and PMMA are ~ 95° and ~ 75° respectively. We studied the wettability of the structured surface against the DCLL process parameters viz. polymer concentration, C_p, and the velocity of the contact line, υ. As the polymer micro-thread deposition makes the surface anisotropic, two sets of contact angles, one, in the direction of the micro-threads (∥) (i.e. contact angle measurement point lies on contact line perpendicular to the direction of micro-thread), and another, transverse to the micro-threads (⊥) (i.e. contact angle measurement point lies on the contact

line parallel to the micro-thread),[48] are shown in Figure 3.5 (c) and (d) insets, respectively. Typical water contact angle data in the direction of the micro-threads (∥) arrangement on both PS and PMMA structured surfaces are shown as insets in Figure 3.3. The experimental water contact angle values for PMMA microstructures span from 60° to 93°. There is a general trend in the case of PMMA microstructure that with increasing contact line velocity (υ), the water contact angle in the direction of the micro-threads (∥) decreases, but in the case of PS the dependency is quite random and ranges from 35° to 98°. This can be attributed to the fact that in the case of PS, there is a myriad of different morphologies such as branching of threads, drop formation, etc. Whereas, for PMMA, in a majority of the cases, the deposition is nearly perfect straight micro-threads. In general, it is observed that, with the increasing velocity of the contact line (υ), the wavelength of deposition (λ) increases (Figure 3.5 (a)). Thus, roughness factor r, which is defined as the ratio of the actual surface area to the projected surface area, decreases with the increasing υ. The decreasing trend of the parallel contact angle with the increasing velocity is not in line with the earlier report,[48] that reflects that parallel contact angle should attain the global minima close to the Wenzel state. From the calculated roughness factor following the Wenzel model,[49,50] the estimation of the contact angle in the direction of the micro-threads (∥) of water for PS (PMMA) microstructured surface, varies from 95.3° to 98° (70° to 74.6°) whereas the same based on the Cassie Baxter model,[51–53] varies from 142° to 166° (139° to 167°). Both models differ vastly from the experimental contact angle values shown in Figures 5 (c). The range of experimental contact angle (∥) for PMMA span above and below the static contact angle of a flat PMMA surface. Apart from that, the water contact angle transverse to the micro-threads (⊥) of PMMA deposited surface is also not following any systematic trend (Figure 3.5 (d)). We have noticed another discrepancy that with increasing the wavelength of the deposition (or with the increasing υ), for a particular polymer concentration,

the width of the deposition should increase to satisfy the mass balance. But to our surprise, there is a decreasing tendency of the width of the micro-thread with increasing υ.

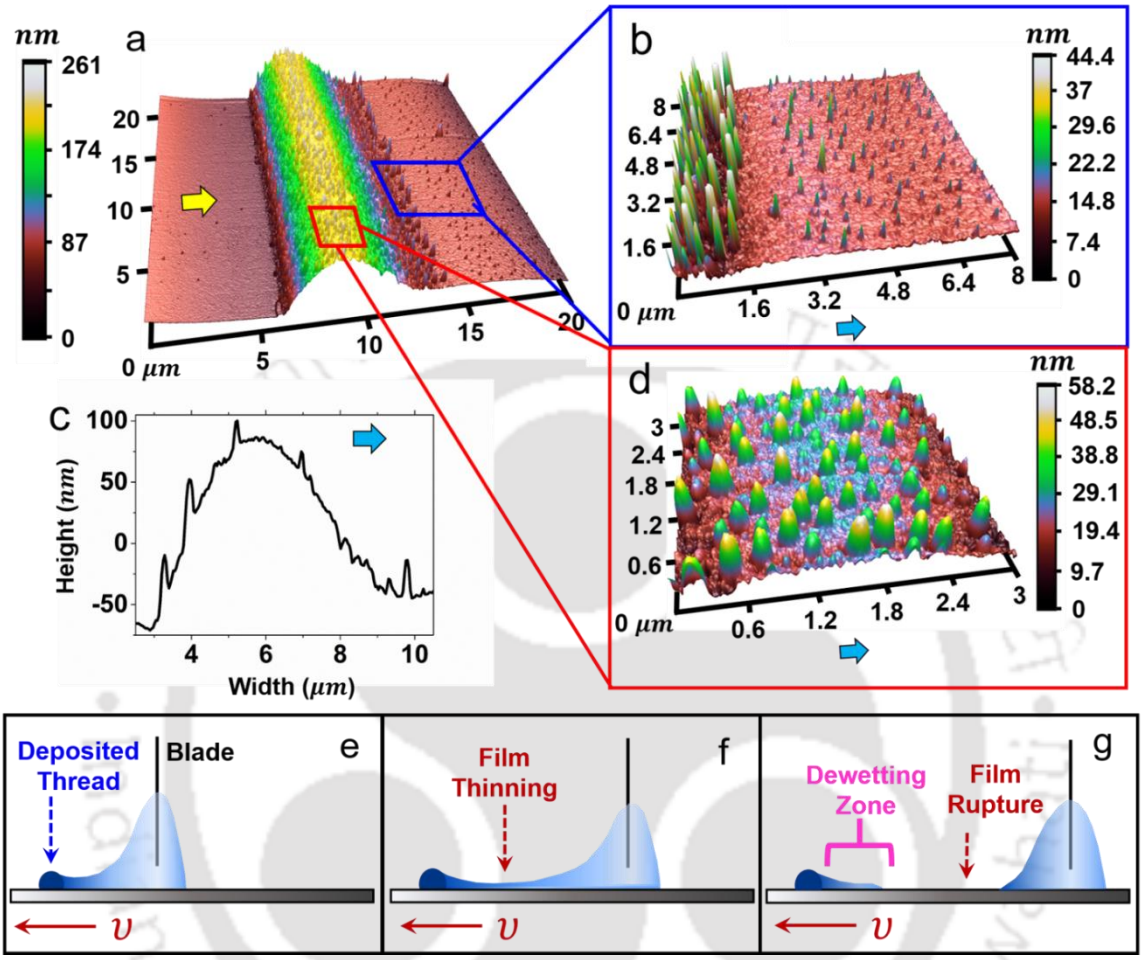

Figure 3.6. (Color online) (a) AFM image of a micro-thread obtained from 0.5 g L^{-1} PMMA in toluene with a contact line velocity of 60 μm s^{-1}. At the front side of the thread (yellow arrow), no nanoscale features are observed, whereas at the backside numerous nano-features are observed. (b) and (d) are the magnified AFM images of the surface just at the backside of the deposited thread and on the micro-thread, respectively. (c) represents the cross-sectional profile of the micro-thread. The blue arrows in (b), (c), and (d) indicate the direction of the contact line motion. The lower panel depicts schematics of the thread deposition (e), thinning of the liquid film (f), and dewetting of the ruptured thin film responsible for the nano structures on the backside of the deposited thread (g), respectively.

Close inspection of the surface revealed that there is a wide range of nanoscale (~ 50 nm $-$ 200 nm) features on the micro-threads (width ~ 6 μm), as well as on the Si substrate itself (Figure 3.6). This hierarchical multi-length-scale structure might have enhanced

the overall roughness factor, r, and differed the polymer fraction on the surface, f_p, way off than that estimated. Also, on the substrate, only at the rear side of the deposited micro-thread, there is nano feature formation due to dewetting (dewetting zone in Figure 3.6 (g)) of the locally diluted liquid thin film of polymer solution adhered to the deposited micro-thread. This film is of locally diluted due to the immediate deposition of the polymers from the solution as micro-thread. The presence of these nanostructures explains the reason behind the random contact angles at the perpendicular orientation. The effect of the nanostructures is averaged out during the measurement of the contact angle in the direction of the micro-threads as the contact line runs over multiple micro-threads. These nanoscopic structures inflict metastable states with a smaller energy barrier that often can be overcome by the slightest energy input or may be activated by noise.[54-56] The precise estimation of the r and f_p is challenging and requires sophisticated tools and is beyond the scope of the present study. Nevertheless, the experimental contact angles of water in the direction of the micro-threads (∥) on the systematically structured surface (in the case of PMMA micro-threads) show that by varying the deposition speed, one can control the wettability of the surface from way above (~ 86°) to much below (~ 68°) contact angle than the same on flat PMMA surface (~ 75°). This also indicates that there may be a transition regime or mixed configurations of the different wetting modes i.e. Cassie and/or Wenzel state. In the direction transverse to the micro-threads (⊥) (Figure 3.5 (d)), the contact angle measurement point lies randomly either on a micro-thread, or on the nano structured PMMA portrusions just behind the deposited thread ('dewetting zone' as shown in Figure 3.6 (g) and (b)) or on the Si substrate devoid of any polymer features. As there is no control over the placement of the contact line, the measured apparent contact angle (⊥) become random. This plausible explanation for the non-monotonic nature of contact angle in the transverse direction (⊥) is supported by the large standard deviation of the measurement shown in Figure 3.5 (d) (note that, y-axis of Figure 3.5 (d) is much compressed compared to Figure 3.5 (c)).

Although there are other methods to control the wettability of surfaces such as chemical (by altering the surface energy) or physical (tuning the surface topography) modification, DCLL offers fabrication of physicochemical composite surfaces at the mild chemical condition to manipulate contact angle. This DCLL might be useful where chemical modification is restricted due to harsh chemical conditions to the sensitive substrate or where physical modification is limited by the requirement of expensive lithographic tools.

In this discussion, we have shown the possible tuning method of wettability of substrate in terms of the contact angle of solution. However, in similar condition, contact angle may differ if we change the concentration of solute into the solution. Change of the concentration directly affects the viscosity of the solution which changes the surface tension of the liquid. Eventually, change of the surface tension has the direct effect on the wettability of the surface. Therefore, viscosity of the solution is also an important parameter for tuning the wettability of any surface.

3.3.5 Effect of Various Parameters

3.3.5.1 Effect of Gap Distance

In this particular experiment, $5 \times 10^{-5}\,\mathrm{g\,L^{-1}}$ PS in toluene is used to deposit PS microdroplets on the Si substrate. Figure 3.7 represents the deposited microdrops of PS while the gap distance (d_g) in between the vertical glass slide and Si substrate was maintained within the range of 214 µm to 43 µm. The contact line speed was at 33 µm s^{-1}.

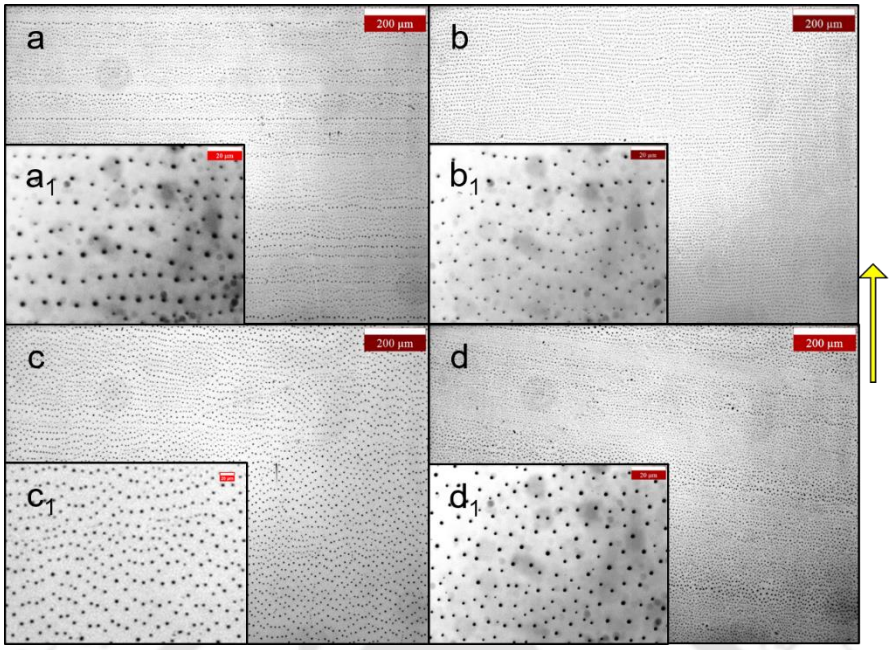

Figure 3.7. Depicts the deposited PS microdrops from toluene at a constant velocity of the contact line of 33 µm s^{-1} when the gap distance d_g is fixed at (a) 214 µm, (b) 129 µm, (c) 86 µm and (d) 43 µm. The respective insets represent the magnified images. All scale bars of primary images and inset images represent 200 µm and 20 µm, respectively. The yellow arrow to the right side corresponds to the direction of contact line movement.

It is observed that the relatively high gap distance 214 µm (Figure 3.7 (a)) to 86 µm (Figure 3.7 (c)) generates ordered deposition of microdroplets compared to the small gap distance d_g of 43 µm (Figure 3.7 (d)). The average diameters of the deposited microdroplets are 1.83 µm (for d_g = 214 µm), 1.87 µm (for d_g = 129 µm), 4.41 µm (for d_g = 86 µm) and, 1.64 µm (for d_g = 43 µm). The average deposition wavelengths (separation distance between two adjacent droplets) are 13.13 µm, 13.64 µm, 21.93 µm and 11.52 µm for the d_g of 214 µm, 129 µm, 86 µm and 43 µm, respectively. As the d_g decreases, the droplet sizes, as well as the average wavelengths first increase and then decrease abruptly at d_g = 43 µm. The hydrodynamics of the liquid polymer solution is influenced by the dg and thus affect the local polymer concentration and subsequent deposition of the polymer droplets. Further extensive investigation is required to fully understand the effect of the gap d_g, its inclination angle.[11]

3.3.5.2 Effect of Speed of Contact Line

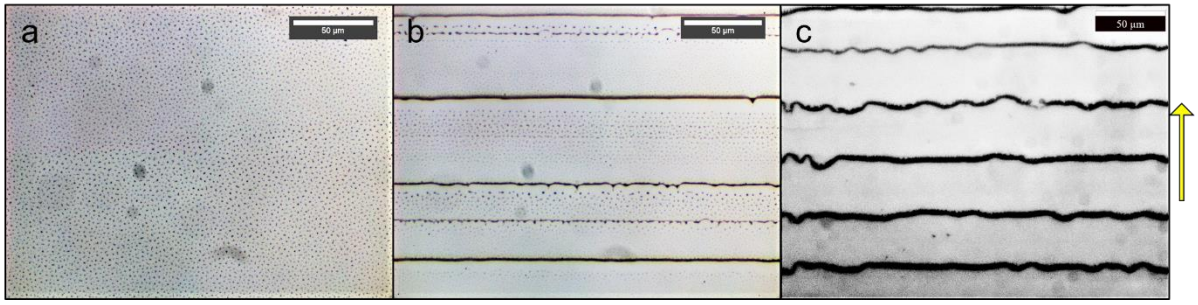

Figure 3.8. Deposited PS microdrops and threads from solution 2 (0.2 mg ml^{-1}PS in toluene) at a contact line of (a) 100 µm $s^{-1}$and (b) 60 µm s^{-1}. (c) depicts deposited PS micro-threads from cyclohexane (0.2 g L^{-1} PS in cyclohexane) at a contact line speed of 60 µm s^{-1}. The gap distance in between the Gillette blade and Si substrate was maintained at ~ 200 µm. The yellow arrow at the right side corresponds to the direction of contact line movement. All scale bars represent as 50 µm.

The speed of the contact line (contact line velocity), the evaporation rate of solvent near the contact line, as well as the accumulation rate of polymer molecules at the contact line synergistically dictate the deposition pattern of the polymer from DCLL. Figure 3.8 depicts the deposition of polymer features on Si substrate from a moderate concentration of PS in toluene at different speeds of the contact line. At a low speed, the time scale of the stick phase of the contact line is long enough to accumulate sufficient polymer molecules near the contact line to form a uniform micro-thread. This deposited micro-thread in turns acts as an additional pinning site that induces the stick phase even longer and the micro-thread accumulates more polymers (Figure 3.8 (a)). During this process, two things happen: first, due to accumulation of the polymer on the micro-thread, local polymer concentration depletes in the liquid meniscus, and second, due to an increase in the time scale of stick-phase (pinning), the liquid meniscus becomes larger with more mass transfer area to facilitate evaporation of the solvent. This lowering of the local polymer concentration and the increased evaporation of the solvent induce

deposition of the micro/nano-droplets on the Si substrate in between two consecutive micro-thread depositions (Figure 3.8 (a)).

At a higher contact line speed of $100\ \mu m\ s^{-1}$, only PS micro/nanodrops due to the lowering of the pinning duration (almost a continuous slip-phase) was observed (Figure 3.8 (a)). The microdrops were formed near the vicinity of the contact line.

3.3.5.3 Effect of Type of Solvent

The volatility of solvent and the solubility of the polymer in the solvent have an immense influence on the deposited morphology. Two different types of solutions are prepared by dissolving PS into two different solvents, toluene and cyclohexane respectively, with a same concentration of $0.2\ g\ L^{-1}$. At room temperature, the solubility of the PS in toluene and cyclohexane are $\sim 1.1 \times 10^{-3}\ mol\ L^{-1}$,[44] and $3.9 \times 10^{-4}\ mol\ L^{-1}$, [44] respectively. Higher volatility of the cyclohexane and less solubility of the PS in cyclohexane brought about the undulated micro-threads (Figure 3.8 (c)). At the identical condition of deposition of PS from toluene, one gets a combination of micro-threads and micro/nanodroplets in between the threads as discussed earlier (Figure 3.8 (b)). In the case of the PS deposition from cyclohexane, as the rate of evaporation is relatively fast and the solubility of PS in cyclohexane is less than that in toluene, the average deposition lengthscale (separation distance between two deposited micro-threads) is relatively smaller for deposition from cyclohexane than that from toluene.

3.3.5.4 Effect of Polymer Concentration

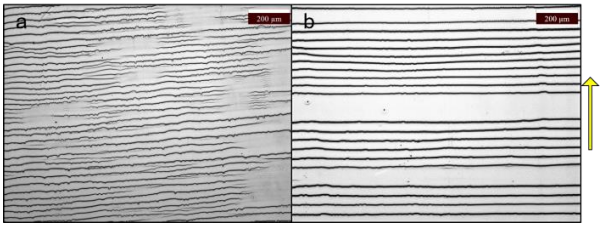

Figure 3.9. Deposited micro-threads from PS in cyclohexane having concentrations of (a) $0.3\ g\ L^{-1}$ and (b) $0.6\ g\ L^{-1}$, at a speed of contact line of $80\ \mu m\ s^{-1}$. The gap distance in between the blade and Si substrate was maintained at $\sim 200\ \mu m$. The yellow arrow at the right side corresponds to the direction of contact line movement. All scale bars represent $200\ \mu m$.

Change of polymer concentration also affects the deposited morphology. Two concentrated PS solutions, $0.3\ \mathrm{g\ L^{-1}}$ and $0.6\ \mathrm{g\ L^{-1}}$ in cyclohexane, were used to deposit microfeatures on Si substrate. Keeping all other parameters such as speed of contact line, d_g, and type of solvent (cyclohexane) the same, only concentrations of the polymer were varied for this study. The deposition of undulated incomplete micro-threads of PS (Figure 3.9 (a)) was obtained for lower concentration ($0.3\ \mathrm{g\ L^{-1}}$), whereas, uniform straight micro-threads (Figure 3.9 (b)) were obtained from a relatively higher concentration of ($0.6\ \mathrm{g\ L^{-1}}$).

3.3.6 Mechanism of Micro-thread Deposition

The DCLL method described in this work is generic and similar depositions can also be observed for other polymer/solvent systems such as PMMA/cyclohexane. For a relatively wide concentration range from $1\ \mathrm{g\ L^{-1}}$ to $2\ \mathrm{g\ L^{-1}}$ and with different contact line speed ranging from $40\ \mu\mathrm{m\ s^{-1}}$ to $100\ \mu\mathrm{m\ s^{-1}}$ straight micro-thread deposition of PMMA from cyclohexane was observed. This supports our earlier observations as well. As the deposition of the micro-threads are relatively straight, one can define the deposition length scale λ_d as the separation distance between two consecutive deposited threads. Dividing this λ_d by contact line speed v gives the average deposition time scale t_d. Next, we will discuss the mechanism of the micro-thread deposition.

During DCLL the solvents from the solution evaporates faster from the regime close to the contact line and to replenish the evaporative loss, the solvent along with the solvated polymer molecules are dragged towards the contact line. [15,16,47] Once the solvent evaporated from the contact line, the local polymer concentration exceeds a threshold value and phase-separates at the contact line. Thus, accumulation of the polymer at the contact line takes place and at the same time, the liquid meniscus gets pinned at the deposited polymers threads. During

this process as the stage continuously moves, the liquid meniscus get thinner over time. This process continues until the liquid film get thin enough to rupture and meniscus slips back to the new pinning position. Thus, stick-clip phenomena of the contact line takes place. Often the solvent from the thin liquid film evaporates and the thin film dewets to small droplets due to van der Walls interactions. Thus, the polymer micro/nanodroplets form in between two micro-threads.

However, assuming the quasi-steady state process of deposition, and neglecting complication of dewetting phenomena in between the micro-threads, the deposition time scale for the micro-threads, $t_d \left(=\frac{\lambda}{v}\right)$, can be estimated as described below.

3.3.6.1 Derivation of the Deposition Time t_d

The deposition of the polymer near the contact line is a quasi-steady-state process and is possible only when the local concentration of the polymer near the contact line is equal or close to the solubility of the polymer at that temperature.

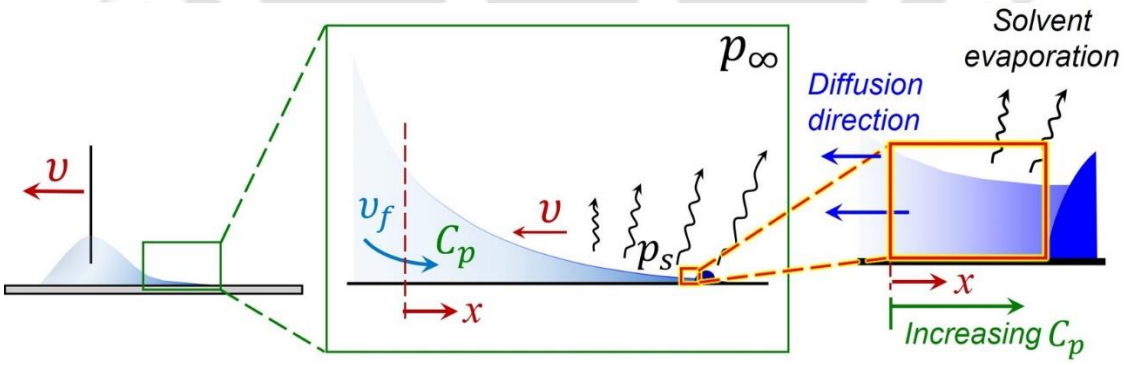

Figure 3.10. Schematic of the receding edge of the dragged polymer solution.

Let's assume a control volume near the contact line (indicated by small red colored rectangle in Figure 3.10) for this analysis. Near the contact line, the rate of change of polymer concentration, $\frac{\partial C_p}{\partial t}$, depends mainly on the following three factors:

1) Advective flow of polymer towards the contact line from the bulk polymer solution.

2) Diffusive flow of polymer from the already deposited polymer thread (maximum polymer concentration), towards the bulk polymer solution (relatively low polymer concentration). Diffusion towards the opposite direction of the bulk advective flow.

3) Increase in polymer concentration due to depletion of the solvent by evaporation.

Let's discuss these three contributing factors separately as follows:

3.3.6.1.1 Advective Flow of Polymer

The rate of change of polymer concentration due to the advective flow of the polymer from bulk to the contact line can be expressed as:

$$\frac{\partial C_p}{\partial t} \approx \frac{\partial (v_f C_p)}{\partial x}, \quad \ldots \quad \ldots \quad \ldots \quad \ldots \quad \ldots \quad \ldots \quad (3.2)$$

Here,

$C_p =$ Molar concentration of polymer in the bulk,

$v_f =$ Bulk flow velocity toward the contact line, (+X direction)

As v_f is a function of stage velocity, at steady state, one can assume this advective flow is proportional to (vC_p). Thus, $\frac{\partial (v_f C_p)}{\partial x} = AvC_p$,

where A is the proportionality constant having unit of m^{-1} and v is the relative velocity of the contact line with respect to the substrate at non-zero stage velocity, (-X direction). Thus, one can write:

$$\frac{\partial C_p}{\partial t} \approx AvC_p, \quad \ldots \quad \ldots \quad \ldots \quad \ldots \quad \ldots \quad (3.3)$$

3.3.6.1.2 Polymer Diffusion Towards Bulk

At the developing stage of the micro-thread deposition, there will be a diffusive flow from the surface of the micro-thread (maximum polymer concentration), towards the bulk polymer solution (Relatively low polymer concentration). For simplicity, we will also assume

the diffusion of the polymer through the solvent molecule is faster than the dissolution rate of the polymer micro-thread. This diffusion is in the -*x* direction and is responsible for the lowering of the polymer concentration in the control volume, i.e., the polymer is depleting from the control volume with time. From Fick's first law of diffusion, one can write the expression of the molar flux of polymer as follows:

$J_p = D_p \frac{\partial C_p}{\partial x}$, where D_p is the diffusivity ($m^2\ s^{-1}$) of the polymer through the solvent. Here one point to be noticed is that, in general, Fick's first law of diffusion is associated with a negative sign on the right-hand side when the gradient of the concentration, $\frac{\partial C_p}{\partial x}$, is itself negative. Here we are considering the flux of the polymer in the negative *x*-direction (as per Figure 3.10), thus the gradient of the concentration, $\frac{\partial C_p}{\partial x}$, is itself positive. Hence no negative sign is considered. From the mass balance, one can write,

$\frac{\partial C_p}{\partial t} + \frac{\partial J_p}{\partial x} = 0$, without considering any polymer generation term in the control volume. Incorporating the expression of J_p from Fick's first law, one can write,

$$\frac{\partial C_p}{\partial t} \approx - D_p \frac{\partial^2 C_p}{\partial x^2}, \quad \dots \quad \dots \quad \dots \quad \dots \quad \dots \quad (3.4)$$

Diffusion being a slow process, the concentration gradient, for an infinitesimally small control volume near a solid wall (here the micro-thread), can be approximated as a linear function of the *x*, i.e. $\frac{\partial C_p}{\partial x} = K_p x$. Here K_p is a phenomenological constant having a unit of mol m^{-5}. Using Taylor series expansion,

$$\frac{\partial c_p}{\partial x} = K_p x$$

$$c_p = c_p(x_0) + c_p'(x_0) \cdot (x - x_0) + \frac{c_p''(x_0)}{2!}(x - x_0)^2 \qquad [at\ x_0 = 0;\ c_p = 1]$$

$$= 1 + K_p x \cdot x + \frac{K_p}{2!} x^2$$

$$= 1 + K_p x^2 + \frac{K_p x^2}{2!}$$

$$\frac{\partial c_p}{\partial t} \approx -D_p \frac{\partial^2 c_p}{\partial x^2}$$

$$\approx -D_p \frac{\partial^2 (1+K_p x^2+\frac{K_p x^2}{2!})}{\partial x^2} \qquad [Substituting\ c_p]$$

$$\approx -D_p[0 + 2K_p + K_p]$$

$$\approx -3K_p D_p$$

$$\approx -K_p D_p \ldots \quad \ldots \quad \ldots \quad \ldots \quad \ldots \quad (3.5)$$

In comparison to the advective polymer flow towards the micro-thread (contributing factor 1) and the rate of the increase of polymer concentration due to the solvent evaporation (contributing factor 3, discussed later), this diffusive backflow is negligible for a concentrated bulk polymer solution. However, this term can become significant for the dilute bulk polymer solution.

3.3.6.1.3 Solvent Evaporation

The third contributor to the rate of change of the polymer concentration is proportional to the evaporation of solvent from the control volume through the meniscus as the mass transfer area. So, the rate of increase of polymer concentration is directly proportional to the rate of depletion of the solvent molecules, i.e.

$$\frac{\partial C_p}{\partial t} \propto -\frac{\partial C_s}{\partial t} \quad \ldots \quad \ldots \quad \ldots \quad \ldots \quad \ldots \quad \ldots \quad (3.6)$$

Where, C_s is the molar concentration of solvent molecule, and the solvent depletion rate can be described by the expression

$$-\frac{\partial C_s}{\partial t} = \alpha\, D_s (p_s - p_\infty) \frac{v}{v_0} \quad \ldots \quad \ldots \quad \ldots \quad \ldots \quad (3.7)$$

where α is a constant, D_s is the diffusivity ($m^2\ s^{-1}$) of the solvent through ambient air, p_s is the vapor pressure of the solvent at the meniscus surface, p_∞ is the vapor pressure of the solvent far away from the meniscus surface with $p_s \gg p_\infty$ and v_0 is the relative velocity of contact line with respect to the substrate at zero stage velocity, (-x direction) and $v \gg v_0$. The factor $\frac{v}{v_0}$ denotes the normalized mass transfer area due to stage velocity.

For a particular concentration, and at a constant temperature, the driving force for solvent evaporation, $(p_s - p_\infty)$, can be assumed constant, and equation (3.7) can be further simplified to

$$-\frac{\partial C_s}{\partial t} \approx K_s D_s \frac{v}{v_0} \quad \ldots \quad \ldots \quad \ldots \quad \ldots \quad \ldots \quad (3.8)$$

Here, $K_s(\approx \alpha p_s)$ is another phenomenological constant having a unit of mol.m^{-5}. Thus, one can write equation (3.6) as,

$$\frac{\partial C_p}{\partial t} \approx K_s D_s \frac{v}{v_0}, \quad \ldots \quad \ldots \quad \ldots \quad \ldots \quad \ldots \quad (3.9)$$

Combining eq. (3.3), (3.5), and (3.9) one can get,

$$\frac{\partial C_p}{\partial t} = AvC_p - K_pD_p + K_s D_s \frac{v}{v_0}, \quad \ldots \quad \ldots \quad \ldots \quad (3.10)$$

Integrating eq (3.10), the deposition time, t_d, can be obtained as,

$\int_{C_p}^{S} \frac{dC_p}{\left[AvC_p - 3K_pD_p + K_s D_s \frac{v}{v_0}\right]} = \int_0^{t_d} dt$, where S is the solubility of the polymer at the operating temperature.

$$t_d = \frac{1}{(Av)} ln \left[\frac{AvS - 3K_pD_p + K_s D_s \frac{v}{v_0}}{AvC_p - 3K_pD_p + K_s D_s \frac{v}{v_0}}\right] \quad \ldots \quad \ldots \quad \ldots \quad (3.11)$$

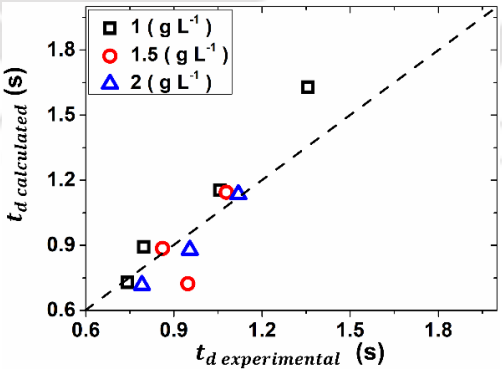

Figure 3.11. Comparison between experimental and calculated deposition time using eq 3.11.

Using the following constants for PMMA/cyclohexane system

$A = 3.5 \times 10^3 \mathrm{m}^{-1}$,

$K_p = 1 \times 10^7 \text{Mol. m}^{-5}$,

$K_s = 6.2 \times 10^3 \text{Mol. m}^{-5}$,

the deposition time scale t_d was estimated using eq. 3.11 for different concentrations and speed of contact line, and compared with the experimental value (Figure 3.11). The agreement between the experimental and theoretical estimation is quite good considering the experimental limitation and simplicity of the model.

3.3.7 Complex Patterning

So far, we have discussed the DCLL, its morphological zone diagram, and its application in tuning hydrophobicity. DCLL opens up a vast new field of micro/nanofabrication with flexibility. One can use multiple depositions using multiple polymers with the appropriate choice of mutually exclusive solvents for the polymers.

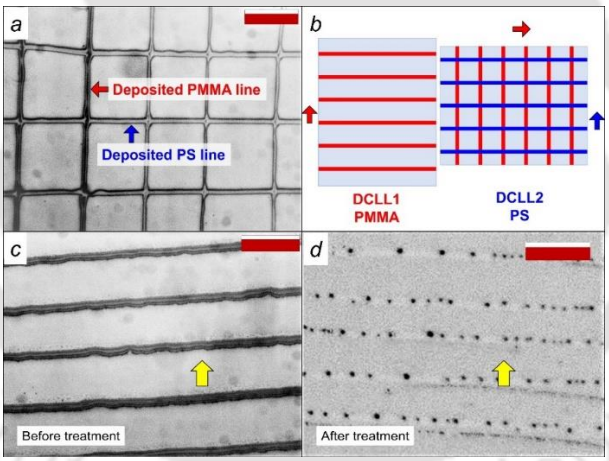

Figure 3.12. (Color online) (a) Optical image represents the deposited complex pattern of PMMA from toluene (vertical stripes) and PS from cyclohexane (horizontal stripes). Here, the concentration of PMMA is 1 g L^{-1} and the contact line velocity is 40 μm s^{-1} in DCLL-1, and in DCLL-2, the concentration of PS is 0.6 g s^{-1} and the contact line velocity is 80 μm s^{-1}. Arrows represent the directions of a moving contact line. (b) Schematic representation of the sequential run of DCLL-1 using PMMA and DCLL-2 using PS. Figure (c) represents PS micro-threads obtained by the DCLL technique, transformed into arrays of micro-drops (d) just by dipping into acetone for 1 min. The scale bar is 50 μm.

The concentration and the contact line speed can be appropriately selected from the morphological zone diagram (Figure 3.4) as per the design requirement. In this report, we demonstrate the fabrication of such a complex pattern as shown in Figure 3.12 (a). First, PMMA was deposited from the toluene solution (concentration $\sim 1\ \mathrm{g\ L^{-1}}$) following DCLL, on a cleaned Si wafer at a stage speed (contact line speed) of $\sim 40\ \mu\mathrm{m\ s^{-1}}$ (DCLL-1). Perfect micro-threads with $\lambda_d \sim 50\ \mu\mathrm{m}$ were obtained. We termed this first deposition as DCLL-1. The sample was then left for $8\ \mathrm{h}$ at ambient conditions for natural drying to remove any excess solvent present on the surface. This process can be made faster by keeping the sample in a vacuum desiccator for an hour. Once the solvent was removed, the same sample underwent DCLL again (DCLL-2) by fixing the sample on the stage orthogonal to the direction of the DCLL-1. This time, PS was deposited from cyclohexane solution ($\sim 0.6\ \mathrm{g\ s^{-1}}$) and at a stage speed of $\sim 80\ \mu\mathrm{m\ s^{-1}}$ to obtain a deposition wavelength of $\sim 65\ \mu\mathrm{m}$. The choice of the concentration and the contact line speed was guided by Figure 3.4 (a). PMMA being insoluble in cyclohexane, remained undisturbed during DCLL-2. This gives a rectangular pattern of micro-threads made of PS in one direction and PMMA in the orthogonal direction (Figure 3.7 (a)). A schematic of DCLL-1 and DCLL-2 is depicted in Figure 3.7 (b). By selecting the mutually exclusive solvent and appropriate polymer concentration and stage speed one can create more complex patterns with micro-threads or micro-droplets of multiple polymers. For microdroplets, one can harness solvent-induced dewetting of the micro-threads,[57] fabricated using DCLL. Dipping the sample having micro-threads in an appropriate solvent, almost instantly the microdroplets can be formed. An example of such transformation of PS micro-thread to PS micro-droplets by dipping into acetone for $1\ \mathrm{min}$ is shown in Figures 3.7 (c) and 3.7 (d).

For this study, we have intentionally chosen common polymers like PS and PMMA for demonstration purposes, as these polymers offer cost-effective options for versatile properties

upon infusion of different co-monomers. These polymers can be modified and already find their use as impact resistance materials, optical glasses, optical filters, microchips, and microfluidic applications. Along with this, due to their biocompatibility, these polymers are used for intra-ocular or contact lenses.[58–60] Meso-patterning with these polymers or their copolymers,[44,61] will help in technological advancement in all these applications. Nevertheless, the DCLL is generic and applicable for other functional polymers as well.

3.4 Conclusions

In summary, this work reports the following salient features of dynamic contact line lithography (DCLL):

- Myriads of polymeric meso features such as microdroplets, undulated micro-threads, straight micro-threads, etc. can be generated using DCLL.
- To fabricate a pattern-on-demand, it is a prerequisite to have a morphological zone diagram. In this work, we presented the zone diagrams for two polymer/solvent systems to demonstrate the robustness and predictive generic nature of the same.
- Along with the microscale deposition, nanoscale features were also developed during DCLL, leading to the one-step hierarchical mesoscale pattern fabrication that vastly influences the wettability of a surface. For example, the wettability of Si substrate (CA ~ 15°) can be tuned by DCLL from CA ~ 35° to ~ 98° using PS. Thus, the wettability of a surface can be controlled by proper selection of polymer and tuning the length scale of deposition.
- The morphological zone diagrams can be a guiding tool to fabricate complex micro patterns with multiple polymer-solvent combinations that are otherwise challenging to achieve. One such pattern fabrication using DCLL is demonstrated.

In contrast to the earlier literature on the evaporative deposition of colloidal particles,[11,21–24,26] we report the deposition of polymer meso-patterns in this study. Although there exist very few accounts on polymer deposition in dynamic contact line settings,[27,35] to the best of our knowledge, for the first time, we present the morphological zone diagram which is of utmost necessity to guide the researchers seeking a desired pattern. Certain process features such as gap distance between the blade and substrate, blade, and substrate wettability, etc. may affect the zone diagram. Further investigation in this direction can be an interesting future research topic. Complex surface texturing using two polymers is demonstrated but this process can be extended further for more than two polymer systems with desired morphology, viz. microdroplets or threads or their combinations as desired. The versatile and low-cost DCLL technique can be employed for meso-patterning with functional materials. This will open up whole new research opportunities in interface science and its applications in the advancement of biomedical,[62] sensors, photonics,[63] etc.

References

[1] K. Pfeiffer, U. Schulz, A. Tünnermann, A. Szeghalmi, Coatings. 7 (2017) 1–12.

[2] P.S. Goohpattader, N. Dwivedi, E. Rismani-Yazdi, N. Satyanarayana, R.J. Yeo, S. Kundu, C.S. Bhatia, Tribol. Int. 81 (2015) 73–88.

[3] N. Dwivedi, R.J. Yeo, P.S. Goohpattader, N. Satyanarayana, S. Tripathy, C.S. Bhatia, Diam. Relat. Mater. 51 (2015) 14–23.

[4] V.P. Babak, V. V. Shchepetov, S.D. Harchenko, J. Frict. Wear. 40 (2019) 593–598.

[5] K. Benyahia, A. Benhaya, M.S. Aida, J. Semicond. 36 (2015) 103001.

[6] B. L. Feng, S.H. Li, Y.S. Li, H.J. Li, L.J. Zhang, J. Zhai, Y.L. Song, B.Q. Liu, L. Jiang, D.B. Zhu, Adv. Mater. 14 (2002) 1857–1860.

[7] M. Sun, C. Luo, L. Xu, H. Ji, Q. Ouyang, D. Yu, Y. Chen, Langmuir. 21 (2005) 8978–8981.

[8] S. Patil, R. Mangal, A. Malasi, A. Sharma, Langmuir. 28 (2012) 14784–14791.

[9] P. Roy, R. Mukherjee, D. Bandyopadhyay, P.S. Gooh Pattader, Nanoscale. 11 (2019) 16523–16533.

[10] R. Bolleddu, S. Chakraborty, M. Bhattacharjee, N. Bhandaru, S. Thakur, P.S. Gooh-Pattader, R. Mukherjee, D. Bandyopadhyay, Ind. Eng. Chem. Res. 59 (2020) 1902–1913.

[11] P. Kumnorkaew, Y. Ee, N. Tansu, J.F. Gilchrist, Langmuir. 24 (2008) 12150–12157.

[12] G.M. Whitesides, S.K.Y. Tang, 2006: p. 63290A.

[13] X. Chang, J. Fang, Y. Fan, T. Luo, H. Su, Y. Zhang, J. Lu, L. Tsetseris, T.D. Anthopoulos, S. Liu, K. Zhao, Adv. Mater. 2001243 (2020) 1–8.

[14] D. Brutin, B. Sobac, B. Loquet, J. Sampol, J. Fluid Mech. 667 (2011) 85–95.

[15] R.D. Deegan, O. Bakajin, T.F. Dupont, G. Huber, S.R. Nagel, T.A. Witten, Nature. 389 (1997) 827–829.

[16] F.F. Shao, A. Neild, T. Alan, Colloids Surfaces A Physicochem. Eng. Asp. 398 (2012) 64–68.

[17] X. Shen, C.M. Ho, T.S. Wong, J. Phys. Chem. B. 114 (2010) 5269–5274.

[18] T.T. Nellimoottil, P.N. Rao, S.S. Ghosh, A. Chattopadhyay, Langmuir. 23 (2007) 8655–8658.

[19] P. Gogoi, A. Chattopadhyay, P.S. Gooh Pattader, J. Phys. Chem. B. 124 (2020) 11530–11539.

[20] N. Basu, R. Mukherjee, J. Phys. Chem. B. 124 (2020) 1266–1274.

[21] B.G. Prevo, O.D. Velev, Langmuir. 20 (2004) 2099–2107.

[22] M. Joy, T. Muangnapoh, M.A. Snyder, J.F. Gilchrist, Soft Matter. 11 (2015) 7092–7100.

[23] C. Loussert, F. Doumenc, J.B. Salmon, V.S. Nikolayev, B. Guerrier, Langmuir. 33 (2017) 14078–14086.

[24] C.N. Kaplan, N. Wu, S. Mandre, J. Aizenberg, L. Mahadevan, Phys. Fluids. 27 (2015) 092105.

[25] U. Thiele, Adv. Colloid Interface Sci. 206 (2014) 399–413.

[26] H.S. Kim, C.H. Lee, P.K. Sudeep, T. Emrick, A.J. Crosby, Adv. Mater. 22 (2010) 4600–4604.

[27] H. Yabu, M. Shimomura, Adv. Funct. Mater. 15 (2005) 575–581.

[28] G. Jing, H. Bodiguel, F. Doumenc, E. Sultan, B. Guerrier, Langmuir. 26 (2010) 2288–2293.

[29] X. Gu, L. Shaw, K. Gu, M.F. Toney, Z. Bao, Nat. Commun. 9 (2018) 534.

[30] M. Le Berre, Y. Chen, D. Baigl, Langmuir. 25 (2009) 2554–2557.

[31] S.F. Maloy, G.L. Martin, P. Atanassov, M.J. Cooney, Langmuir. 28 (2012) 2589–2595.

[32] A.P. Mouat, C.E. Wood, J.E. Pye, J.C. Burton, Phys. Rev. Fluids. 4 (2019) 100512.

[33] M. Gonuguntla, A. Sharma, Langmuir. 20 (2004) 3456–3463.

[34] W. Sun, F. Yang, J. Phys. Chem. C. 118 (2014) 10177–10182.

[35] A. Deblais, R. Harich, A. Colin, H. Kellay, Nat. Commun. 7 (2016) 1–7.

[36] N. Bhandaru, A. Das, N. Salunke, R. Mukherjee, Nano Lett. 14 (2014) 7009–7016.

[37] R. Hiorns, Polymer Handbook, 4th edn, Edited by J Brandup, EH Immergut and EA Grulke, Associate Editors A Abe and DR Bloch, John Wiley and Sons, New York, 1999, pp 2250, ISBN 0-471-16628-6, Polym. Int. 49 (2000) 807–807.

[38] S. Mettu, M.K. Chaudhury, Langmuir. 26 (2010) 8131–8140.

[39] P.S. Goohpattader, S. Mettu, M.K. Chaudhury, Langmuir. 25 (2009) 9969–9979.

[40] M.K. Chaudhury, P.S. Goohpattader, Eur. Phys. J. E. 36 (2013) 15–29.

[41] W.Z. Zhang, X.D. Chen, J. Yang, W.A. Luo, M.Q. Zhang, J. Phys. Chem. B. 114 (2010) 1301–1306.

[42] T.N. Bell, E.L. Cussler, K.R. Harris, C.N. Pepela, P.J. Dunlop, J. Phys. Chem. 72 (1968) 4693–4695.

[43] L. Besley, G.A. Bottomley, J. Chem. Thermodyn. 5 (1973) 397–410.

[44] A. Pandey, K. Murmu, P.S. Gooh Pattader, RSC Adv. 11 (2021) 10183–10193.

[45] A. Shivamurthy, P. S, P.G. R, R.N. M, S.R. J, Proc. 3rd Int. Conf. Theor. Appl. Nanosci. Nanotechnol. (2019) 3–9.

[46] F. Shao, T.W. Ng, J. Efthimiadis, A. Somers, W. Schwalb, J. Colloid Interface Sci. 377 (2012) 421–429.

[47] L. Shmuylovich, A.Q. Shen, H.A. Stone, Langmuir. 18 (2002) 3441–3445.

[48] J.Y. Chung, J.P. Youngblood, C.M. Stafford, Soft Matter. 3 (2007) 1163–1169.

[49] R.N. Wenzel, Ind. Eng. Chem. 28 (1936) 988–994.

[50] R.N. Wenzel, J. Phys. Colloid Chem. 53 (1949) 1466–1467.

[51] A.B.D. Cassie, S. Baxter, Trans. Faraday Soc. 40 (1944) 546–551.

[52] A.B.D. Cassie, Discuss. Faraday Soc. 3 (1948) 11–16.

[53] E. Bormashenko, Philos. Trans. R. Soc. A Math. Phys. Eng. Sci. 368 (2010) 4695–4711.

[54] M.K. Chaudhury, P.S. Goohpattader, Eur. Phys. J. E. 35 (2012) 1–9.

[55] A. Marmur, Soft Matter. 2 (2006) 12–17.

[56] Johnson, Jr, R. E.; Dettre, R. H.; Surface and Colloid Science; Wiley-Interscience: New York, vol. 2, 1969, pp. 85–153

[57] A. Verma, A. Sharma, Adv. Mater. 22 (2010) 5306–5309.

[58] S. Zuppolini, A. Borriello, M. Pellegrino, V. Venditto, L. Ambrosio, L. Nicolais, J. King Saud Univ. - Sci. 29 (2017) 487–493.

[59] A. López, A. Hoess, T. Thersleff, M. Ott, H. Engqvist, C. Persson, Biomed. Mater. Eng. 21 (2011) 323–332.

[60] M.R. Panahi-Bazaz, M. Zamani, B. Abazar, J. Ophthalmic Vis. Res. 4 (2014) 201–207.

[61] A. Pandey, S. Maity, K. Murmu, S. Middya, D. Bandyopadhyay, P.S. Gooh Pattader, Nanotechnology. (2021).

[62] E. Ostuni, C.S. Chen, D.E. Ingber, G.M. Whitesides, Langmuir. 17 (2001) 2828–2834.

[63] J.D. Joannopoulos, S.G. Johnson, J.N. Winn, R.D. Meade, Second Edition, 2008.

Chapter 4

Janus Micro-thread to Micro-nanodroplets Using Dynamic Contact Line Lithography

This page is left blank intentionally

Abstract

Dynamic contact line lithography (DCLL) is generally used for the template-less but well-ordered deposition of polymer micro/nanostructures from the solution of homopolymer. DCLL from the blend of several polymers in a common suitable solvent can generate rich morphologies including nanostructured Janus micro-threads on a surface which might be challenging to fabricate using any other method. A blend of polystyrene (PS) and poly (methyl methacrylate) (PMMA) in toluene with different compositions and concentrations are used for DCLL at a constant contact line speed of $10\ \mu m\ s^{-1}$. Variations of compositions and the overall concentration of polymer, engender Janus micro-threads to undulated threads and multilayered micro/nanodroplets of PS/PMMA. Interestingly, the more soluble PS phase separates first compared to less soluble PMMA near the contact line due to the enhanced local concentration of PS during the convective flow of the solvent toward the contact line. This is also verified by DCLL using PS/PMMA blend in ethyl acetate as well. In that case, more soluble PMMA deposits first near the contact line compared to marginally less soluble PS in the solvent.

4.1 Introduction

A homogeneous blend of two dissimilar polymers in a common solvent phase separates at appropriate thermodynamic conditions dictated by the nature of the polymers, solvent, compositions, and temperature.[1] This bulk phase separation of such polymer blend may turn into stable microphase separation in presence of the corresponding block copolymer due to the surfactant-like behavior of the copolymer. When geometrically confined into a thin film, the polymer blend alone,[2] or in combination with their corresponding copolymer,[3] self assembles into fascinating micro/nano morphologies. Polymeric phase-separation-induced morphological evolution has been extensively investigated over the last few years.[4–9] Controlling the phase segregated morphology of blend polymer, is challenging. Various avenues to fabricate well-

* This Chapter is published in *Journal of Applied Polymer Science*, **2022**, April, 1-11

ordered micro/nano morphology like hierarchical,[10] core-shell,[11–13] multilayer deposition,[14,15] or alternative deposited structure,[16,17] etc. from multiple polymers are explored. The motivation to construct these polymeric micro/nanopatterns kindles from scientific urge as well as from practical applications such as resists,[18] smart adhesives,[19,20] optoelectronics,[21] magnetic media,[22] extraction using carbon-based nanohybrid materials,[23–25] substrates for preferential cell proliferation,[26] smart skins,[27,28] etc.

Predominantly, instability of thin-film along with the external perturbations such as electric field,[29–32] temperature,[3] or solvent assisted dewetting,[33,34] etc. engender micro/nanostructures in soft films. Self-assembly of these random mesoscale features to the well-ordered patterns guided by a physicochemical template,[35] or even without a template,[36] is also reported. The phase separation in polymer blends or copolymers provides tools for further miniaturization of the developed structure. The segregated morphologies of immiscible polymer blends may be altered by different factors. The effect of film thickness,[37] and molecular weight of respective polymers,[38] on phase-separated morphologies are studied extensively for a common and vastly used blend of polystyrene (PS) and poly (methyl methacrylate) (PMMA). The composition of PS/PMMA in a blend also dictates the morphology and the preferential arrangements of the components.[39,40] Tanaka et al. demonstrated that, despite having overall higher surface energy, PMMA tends to self-assemble at the film surface when low molecular weight PMMA was used, predominantly due to the smaller conformational entropic penalty.[38] It was also argued that in a PS/PMMA/chloroform system, due to low solubility of PS in chloroform, PS first phase separates from PS/PMMA blend, and later PMMA forms a thin layer at the polymer-air interface as PMMA remain solvated in chloroform for a longer time.[14] Thus, along with the compositions of PS/PMMA in blend polymer, the surface energy of the underlying substrate is also a crucial factor that dictates the evolution of micro/nanostructured morphologies.[41] It is also found that PMMA

preferentially wets the SiO_x surface, while intermediate surface energy of substrate shows non-preferential wetting. Here, the intermediate surface energy of substrate refers to that substrate, whose surface energy lies in between blend components and equally wets by each component. This type of non-preferential surface, often refers as the "neutral" surface.[41]

Among the fabrication methods, spin-dewetting is a very rapid technique and widely adopted for decorating a surface with nanoscale structures.[2,8,16,42–44] Apart from that, dip-coating lithography,[45] physicochemical template guided deposition/ dewetting,[7,13,16,46–50] external electric field mediated assembly,[31,51,52] are also promising techniques to craft fascinating intricate features on the soft polymer surface. Alternate arrays of PS-PMMA mesoscale features can be fabricated by sequential spin dewetting on a pre-patterned substrate.[16] Also exploiting the H-bond and phase separation of the components of block copolymers, precise control of the nanoscale arrangement of the different polymeric blocks is also achieved earlier.[17] Evaporative deposition from dynamic meniscus of polymer solution creates myriad structures with the appropriate tuning of polymer concentration and speed of deposition.[53] In chapter 3, we demonstrated templateless mesoscale threads or droplets of homopolymer using dynamic contact line lithography (DCLL).[36] In that article, a morphological phase diagram to predict the deposited morphology on a Si/glass substrate was reported. Sequential DCLL with different polymers in appropriate solvent resulted in a decorated surface with multiple polymeric threads. What is still not explored extensively is the facile fabrication method for the micro/nanostructures comprising of multiple polymers of different kinds in a well-defined arrangement having close proximity with short-range order.

In the present study, we demonstrate for the first time, the fabrication of well-ordered 'Janus' micro-threads and nanodroplets comprising of PS and PMMA, placed adjacent to each other using the DCLL method (Figure 4.1), without any physico-chemical guidance or without using any conventional lithography process. The term 'Janus' signifies a double-faceted

structure with two different polymers. The effects of overall polymer concentration and the PS/PMMA blend composition on the morphology of deposited patterns are studied. Switching of the relative positions of PS-PMMA in a Janus micro-thread is also demonstrated while deposited from an appropriately chosen solvent. This unique methodology to generate Janus micro-threads and micro/nano-droplets is generic and this will open up the new window of the fabrication process for the seemingly complex micro/nanostructures in an easy and accessible manner. This process may be appropriately tuned for desired large area micro/nanopatterning for industrial applications. The term 'Janus' is used here to refer to the side-by-side deposition of two dissimilar polymers in a single entity just like a two-faced structure.

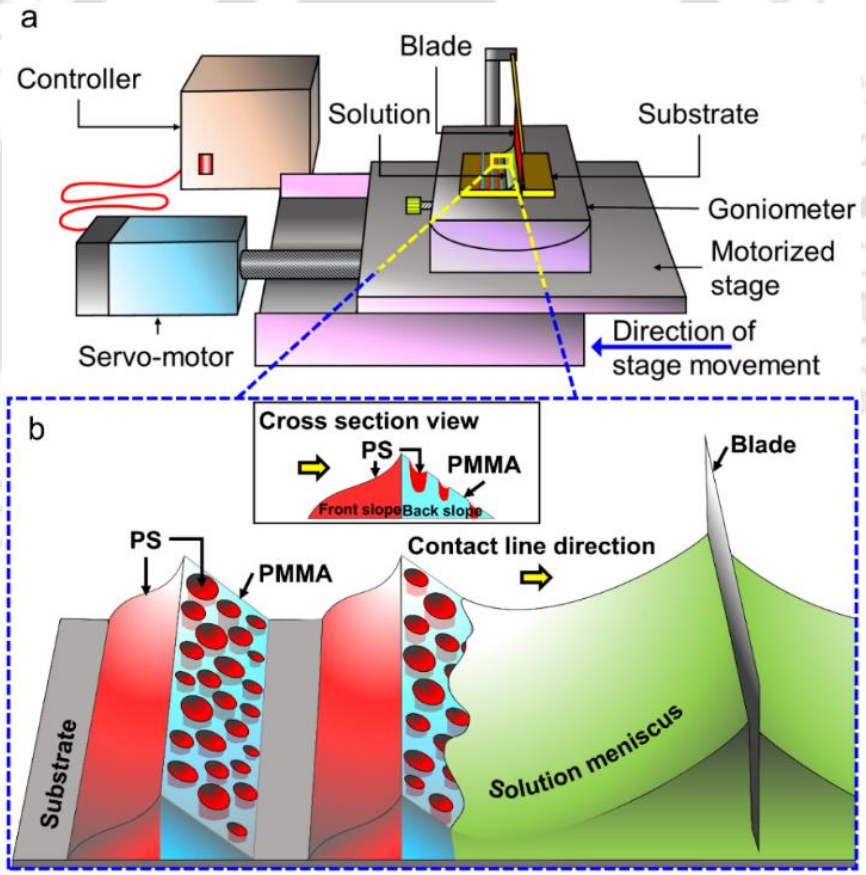

Figure 4.1. (a) A schematic of the experimental setup for Dynamic Contact Line Lithography (DCLL) and deposition of Janus PS/PMMA micro-thread from the blend solution in toluene. The fixed blade drags the PS/PMMA blend solution meniscus on the precisely controlled moving substrate to form periodically deposited Janus micro-threads. (b) Magnified schematic of Janus micro-thread.

4.2 Materials and Methods

4.2.1 Solution Preparation

The solutions of three different concentrations of PS/PMMA blend, $1\,\mathrm{g\,L^{-1}}$, $0.1\,\mathrm{g\,L^{-1}}$, $0.01\,\mathrm{g\,L^{-1}}$ were prepared by dissolving the polymers in toluene to fabricate line, undulated-line, and micro/nanodrop structured surfaces, respectively using DCLL.[36] Combinations of polymer concentration and the average contact line velocity (opposite to stage velocity), can be selected based on the desired feature on the silicon substrate. The guidelines for the choice of the parameters are discussed in detail in our earlier report.[36] The composition of PS and PMMA was varied in the blend by mixing PS and PMMA solution in $1:3$, $1:1$, and $3:1$ weight ratios. Both the polymers, PS (MW ~ 192,000, purity: 99 %, CAS No.: 9003-53-6) and PMMA (MW ~ 120,000, purity: 99 %, CAS No.: 9011-14-7) were purchased from Sigma Aldrich India as pelleted form and were used as procured without any modification. The solvent, toluene (rectified, purity: 99 %, CAS No.: 108-88-3) and ethyl acetate (extra pure, purity: 99.5 %, CAS No.: 141-78-6) was purchased from Loba Chemie India.

The solubility of PS and PMMA was determined by allowing the respective polymers to dissolve individually up to saturation point, into $2\ \mathrm{ml}$ of solvents (toluene and ethyl acetate) with vigorous stirring. The process was performed at a room temperature of $25^{\circ}\mathrm{C}$.

4.2.2 Substrate

A p-type one-sided polished silicon wafer with an orientation of $\langle 100 \rangle$, was used as a substrate to deposit polymers from the dynamic contact line. The silicon wafer was provided by Macwin India. Prior to the experiment, silicon substrates were cut into rectangular pieces of $1\,\mathrm{cm} \times 2\,\mathrm{cm}$ and were cleaned in Piranha solution, a mixture of concentrated sulphuric acid (98 %) and hydrogen peroxide, in a $7:3\,(\mathrm{v/v})$ ratio. Later, the substrates were cleaned with

the flow of a copious amount of de-ionized water. The cleaned substrates were stored underwater and were dried in the flow of nitrogen gas just before the DCLL experiment.

4.2.3 Dynamic Contact Line Lithography (DCLL)

The details of the DCLL have been discussed elsewhere.[36] Briefly, the silicon substrate was placed horizontally, on a custom-made unidirectional movable stage (motorized stage from Holmarc, India) (Figure 4.1). A stainless-steel blade (Gillette, India) was kept perpendicular to the silicon substrate by maintaining a narrow gap distance of $\sim 200\ \mu m$. $20\ \mu l$ of the polymer blend solution was dispensed into the gap and the solution was arrested in between the vertical blade and horizontal substrate due to the capillary force. After dispensing, the Si substrate along with the stage was driven at a constant velocity while the vertical blade was kept stationary. The solution was dragged by the blade on the moving substrate. As the stage moved, the contact line of the polymer solution was dragged in the opposite direction with an average velocity, the magnitude of which was identical to that of the stage velocity. So, the stage velocity can be assumed as the average contact line (CL) speed. The contact line speed for all the experiments described here was maintained at $10\ \mu m\ s^{-1}$. Pinning at the receding contact line, formation of a thin liquid meniscus, and evaporation of solvent synchronize together to form polymer micro-threads. The relative solubility difference of PS and PMMA in toluene gives rise to the periodic Janus micro-threads on the substrate. The room temperature was maintained at $25^{\circ}C$ and the relative humidity was at $68 \pm 2\ \%$ during the experiment. The effect of a slight variation of temperature and relative humidity on the pattern formation was negligible. After deposition of the polymeric structure, the substrate was kept in a vacuum desiccator for $24\ h$ before further characterization.

4.2.4 Characterization

The topography of the deposited polymer features was characterized by atomic force microscopy (AFM, Bruker, Innova series, Germany) in tapping mode, and light reflected optical microscopy (Axio Scope.A1 MAT HAL 100, Carl Zeiss Microscopy, Germany) was used to capture the bright field optical image. Generally, from the AFM phase images, PS and PMMA should be recognized. However, due to rough topography, especially at the trailing edge of the threads, the phase images were not much conclusive. So, we resorted to a selective solvent treatment approach (discussed later) to detect the different polymeric domains. A Raman spectroscopic analysis (Horiba Jobin Vyon, LabRam HR, France) was also performed to support the outcome from selective solvent treatment. Whereas the AFM and optical images were indicating the morphology of the deposited structure, the Raman analysis confirmed the specific positions of the individual polymers within those structures.

4.2.5 Selective Solvent Treatment

Micro/nanostructures of PS-PMMA fabricated using DCLL on Si substrates were treated with cyclohexane and acetic acid separately. Cyclohexane, being a good solvent for PS and non-solvent for PMMA, selectively dissolves the PS from the features of mixed polymers. Similarly, acetic acid dissolves PMMA keeping PS morphology intact. For the selective solvent treatment, substrates were immersed in the appropriate solvent for 2 h and then dried in a mild flow of nitrogen stream. The samples were then kept in a vacuum desiccator for 6 h before further characterization using AFM and Raman spectroscopic analysis.

At least 4 samples were prepared by the DCLL method for each combination of polymer blend composition and contact line velocity to check the repeatability. These samples were characterized by optical microscopy and AFM in each stage of morphological evolution. To ensure the position and morphology of the deposited PS and PMMA, these characterizations

were performed at least 4 different places on each sample, before and after the selective solvent treatment.

4.3 Results and Discussion

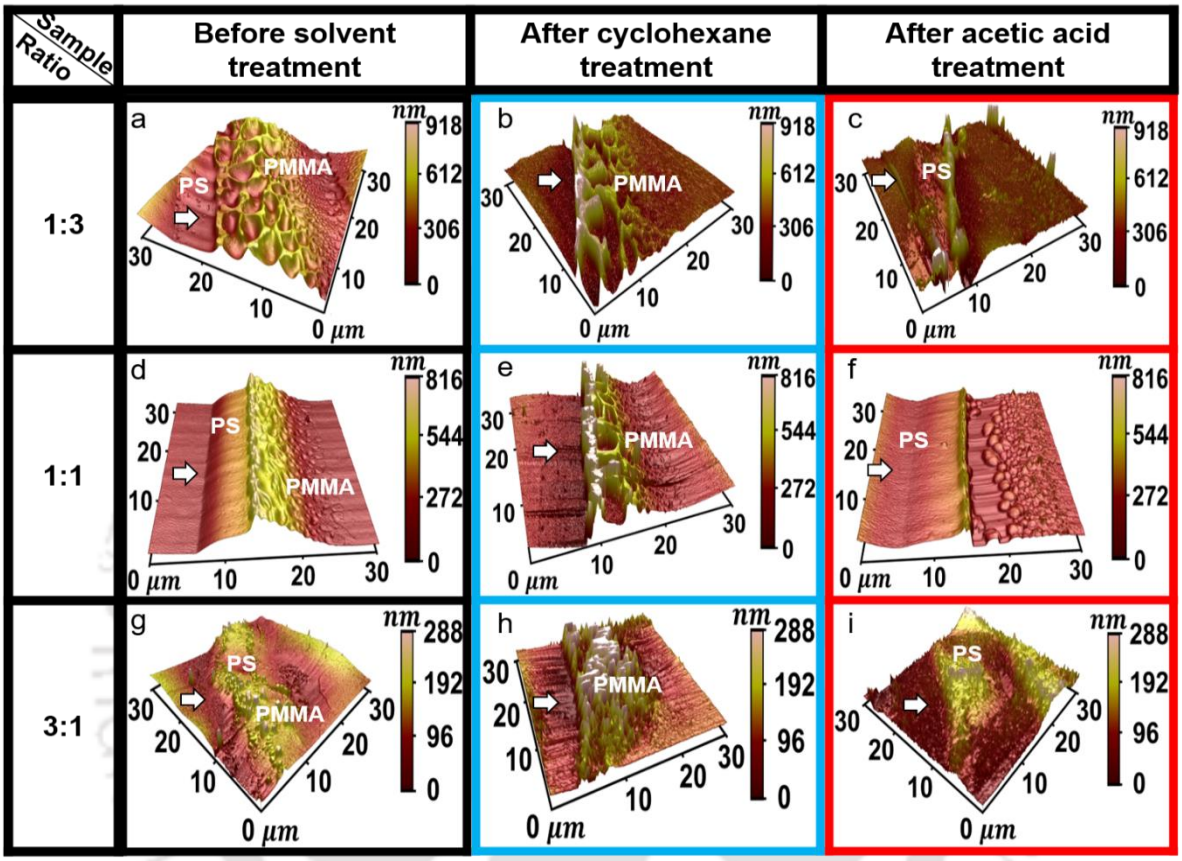

Figure 4.2. The first column (a, d, g) depicts AFM images of the deposited morphology from PS/PMMA blend polymer solution having the composition of $1:3$, $1:1$, and $3:1$ (PS : PMMA) respectively. The second (b, e, h) and the third (c, f, i) columns represent corresponding remnant PMMA and PS after selective etching of polymer by washing with cyclohexane (good solvent for PS) and acetic acid (solvent for PMMA), respectively. In all the cases, the overall polymer concentration is $1\ g\ L^{-1}$ and the arrow represents the direction of contact line motion.

Three different overall concentrations of blend polymers: $1\ g\ L^{-1}$, $0.1\ g\ L^{-1}$, and $0.01\ g\ L^{-1}$ were used to fabricate the deposited structures using DCLL and we investigated 3 different blend compositions with PS/PMMA weight ratios $1:3$, $1:1$, and $3:1$ in each

concentration. Figure 4.2 shows the AFM images of the micro-threads formed by the DCLL using $1\,g\,L^{-1}$ polymer concentration and at the average contact line speed of $10\,\mu m\,s^{-1}$. Changing the speed to $40\,\mu m\,s^{-1}$ slightly change the morphology of the Janus structure with reduced undulation as indicated by the phase diagram reported in our earlier report.[36] The average width of the threads is $\sim 25 \pm 3\,\mu m$, and the periodicity of the deposition is of $\sim 51.5 \pm 2\,\mu m$. The morphology of the Janus threads is significantly influenced by the composition ratio. With $75\,\%$ PMMA, each thread starts with a relatively smooth PS rich domain (width $\sim 4 \pm 1.5\,\mu m$) followed by the PMMA rich labyrinth section (width $\sim 21 \pm 2\,\mu m$) (Figure 4.2 (a)). The major part of the thread however is comprised of interconnected labyrinth-like PMMA structures (labyrinth domain) having cavities filled with PS. The selective solvent etching with cyclohexane (to remove PS from the morphology) (Figure 4.2 (b)) and acetic acid (to remove PMMA) (Figure 4.2 (c)) depicts the precise position of the PS and PMMA on the thread-like pattern. From the AFM images of the selective solvent etched samples, it is evident that for the PS: PMMA composition of $1:1$ as well, the front slope of the Janus thread is comprised of a relatively smooth PS rich domain and the back slope is forming PMMA rich labyrinth structures, similar to that of the composition of PS: PMMA :: $1:3$, only with relatively wider front PS slope. A similar trend is observed for the interconnected droplets obtained from the solution having PS: PMMA ratio of $3:1$.

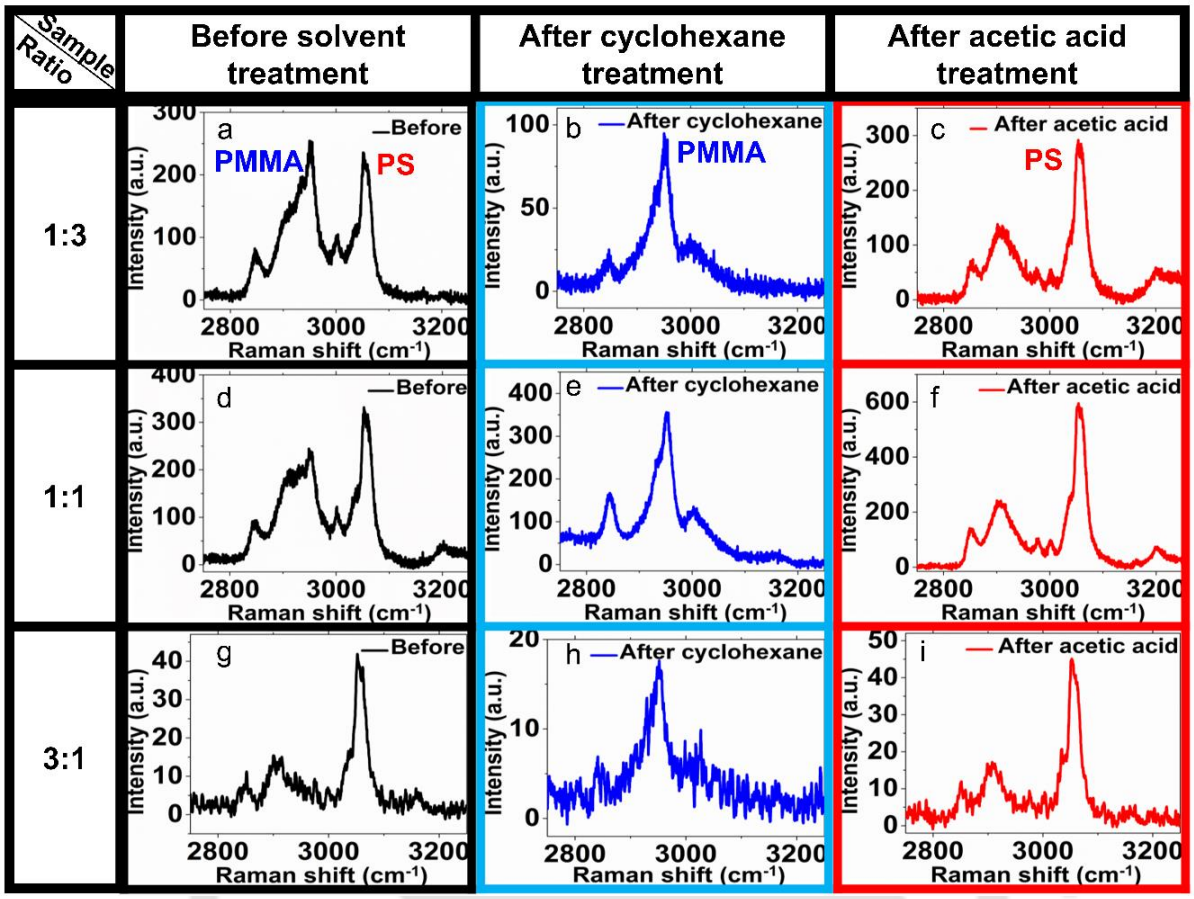

Figure 4.3. Raman spectra of the deposited micro-threads (a, d, g) and the same after selective solvent etching of the deposited morphology with cyclohexane (b, e, h) and acetic acid (c, f, i). In all the cases, the overall polymer concentration is 1 g L^{-1}.

The precise location of the component polymers and the composition of the threads or connected droplets was further confirmed at each stage by Raman spectroscopy (Figure 4.3). PMMA has the most prominent Raman peak at $2957\ cm^{-1}$ which is featured by the vibration of C-H stretching.[3] This is observed only for all the as-deposited samples (Figure 4.3 (a), (d), (g)) and the samples after washing with cyclohexane (Figure 4.3 (b), (e), (h)). On the other hand, PS demonstrates three of its characteristic peaks between $3200-2800\ cm^{-1}$. The vibrations of tertiary CH stretching and CH_2 stretching of the aliphatic group and CH stretching of the aromatic ring are observed at $2900\ cm^{-1}$, $2852\ cm^{-1}$ and $3050\ cm^{-1}$, respectively.[54,55] All these Raman bands are observed in as-deposited samples (Figure 4.3 (a), (d), (g)) and the

samples after acetic acid treatment (Figure 4.3 (c), (f), (i)). In the case of, PS/PMMA blend ratio $1:3$, it is quite evident that the PMMA peak is stronger than PS (Figure 4.3 (a)), which is expected due to the higher concentration of PMMA. As the PMMA fraction decreases (for PS: PMMA ratio of $1:1$ and $3:1$) the intensity of PMMA peak in comparison to PS decreases (Figure 4.3 (d), (g)). These results along with the AFM (Figure 4.2) images support the precise location of the component polymers.

For the blend composition of PS: PMMA :: $1:1$, the relatively smooth PS domain at the front slope is increased to width $\sim 10 \pm 1.2\ \mu m$, and PMMA labyrinth domain is decreased to width $\sim 15 \pm 1.9\ \mu m$. A schematic representation of the Janus thread deposited from DCLL is illustrated in Figure 4.1 (b). Blend compositions having a higher fraction of PMMA (PS: PMMA = $1:3$, Figure 4.2 (a)) or at least equal to PS (PS: PMMA = $1:1$, Figure 4.2 (d)) have more tendency to form a relatively straight lines/thread-like pattern compared to the blend having PS in higher fraction (PS: PMMA = $3:1$), in which case, undulated lines having nearly isolated hemispherical polymer droplets (Figure 4.2 (g)) are observed.

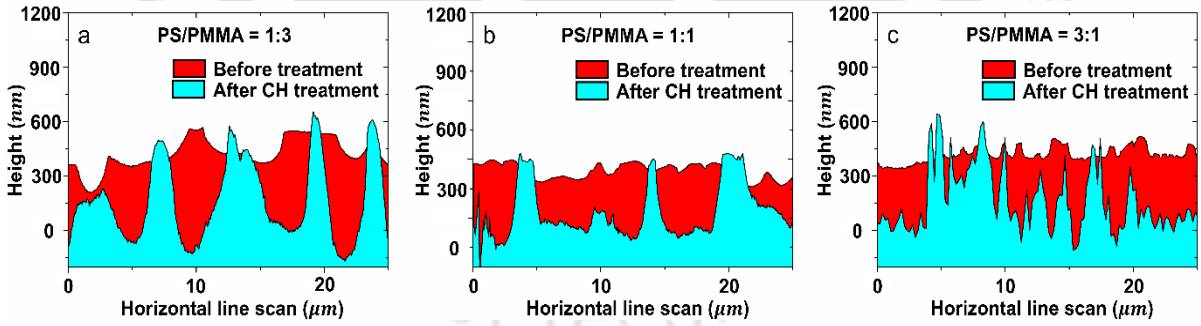

Figure 4.4. Depict the line scans of AFM images at the central region of the PMMA enriched labyrinth domain parallel to the axis of the micro-threads from PS/PMMA blend ratio 1: 3 (a) and $1:1$ (b) with an overall concentration of 1 g L^{-1}. (c) denotes the line scan of the AFM images of the hemispherical droplets formed in DCLL from PS: PMMA blend ratio $3:1$. In all three cases, before and after cyclohexane washing (CH treatment) is represented by the red and cyan colors respectively. Cyan color thus represents the morphology of the remnant PMMA on the surface.

The width of the PS rich domain and the PMMA labyrinth domain was validated from the line scan of the samples after selective etching of PS as well. Line scans from the AFM images at the middle of the labyrinth domain and parallel to the axis of the threads verify the presence of PS into the cavities of the PMMA labyrinth (Figure 4.4). The depth of the pits (Figure 4.4 (a) – (c), red area) eventually increases after cyclohexane treatment (Figure 4.4 (a) – (c), cyan area).

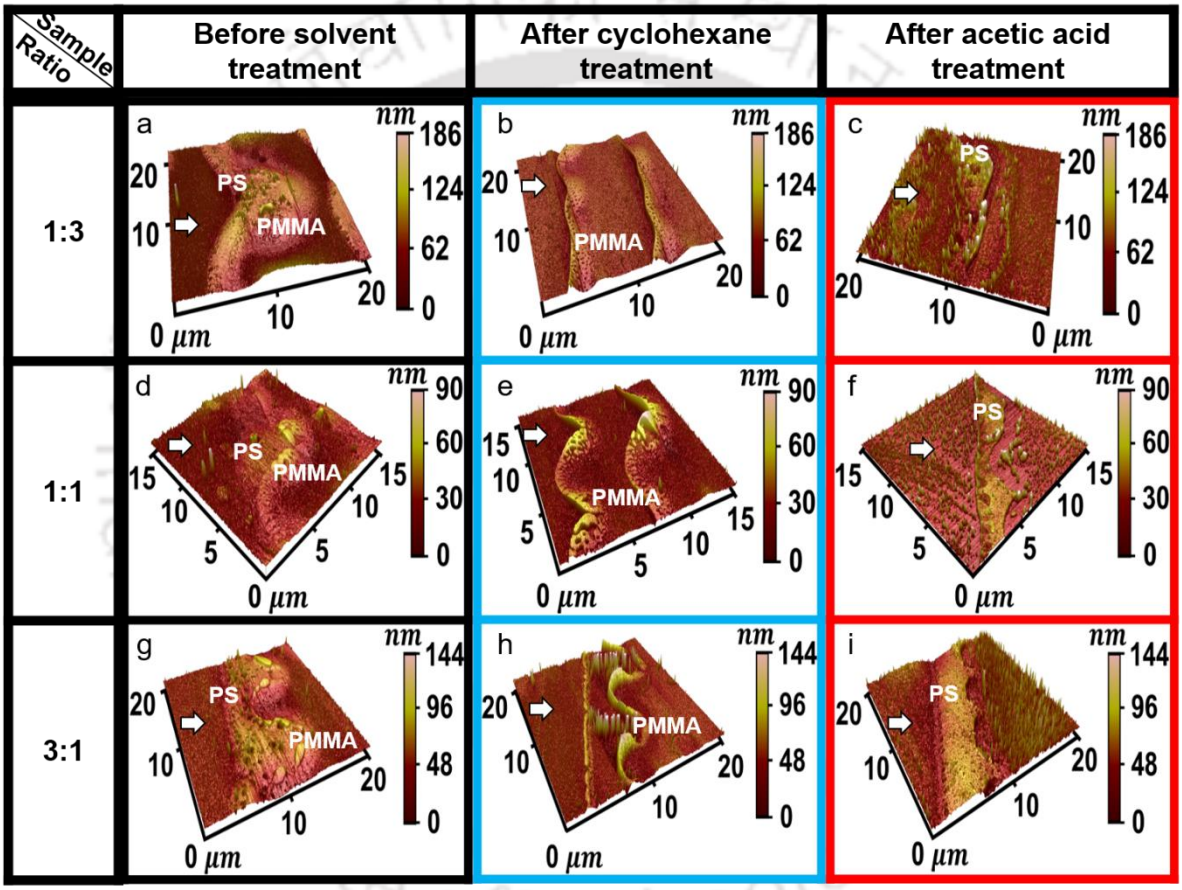

Figure 4.5. The first column represents AFM images of deposited morphology from PS/PMMA blend having compositions PS: PMMA ratio 1:3 (a), 1:1 (d), and 3:1 (g) with the overall polymer concentration of $0.1\,g\,L^{-1}$. The second (b, e, h) and the third (c, f, i) columns represent corresponding remnant PMMA and PS after washing with cyclohexane and acetic acid, respectively. The arrow represents the direction of the contact line motion.

For the overall polymer concentration of $0.1\,g\,L^{-1}$, the undulated polymer threads of PS/PMMA, deposited by DCLL, are shown in Figure 4.5. Similar to the higher concentration, for this case also, the deposition of PS and PMMA rich domains are at the front and rear slope of the undulated thread respectively. In contrast to the labyrinth of PMMA observed in the case of a higher concentration, mostly nano-threads of PMMA along with the spikes of PS were formed at low concentrations (Figure 4.5). We suspect that some patchy thin layer of PS underlayer might be formed. While washing with cyclohexane, some amount of bulk PMMA was also removed from the system due to the etching of the PS underlayer.

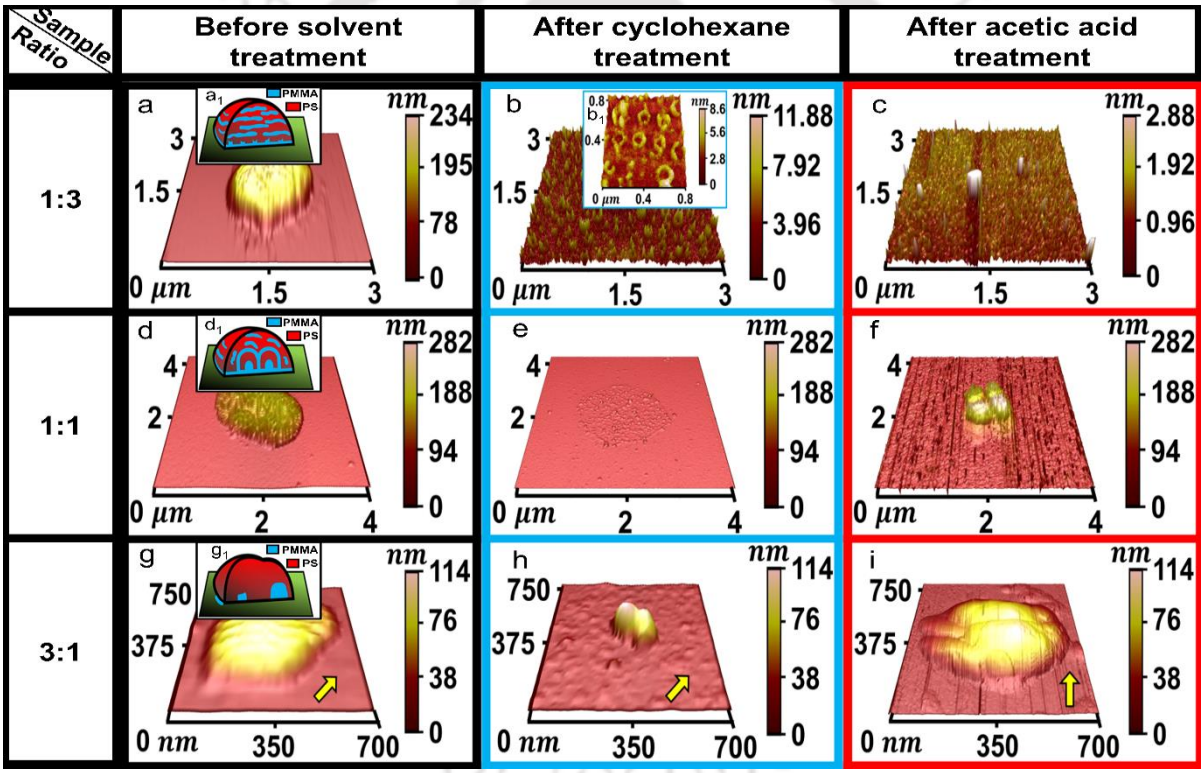

Figure 4.6. The first column represents AFM images of deposited composite micro/nanodroplets from PS/PMMA blend having compositions PS:PMMA ratio 1:3 (a), 1:1 (d), and 3:1 (g) with the overall polymer concentration of $0.01\,g\,L^{-1}$. The schematic representations of the plausible PS/PMMA arrangement inside the droplets are depicted as insets (a_1, d_1, and g_1). The second (b, e, h) and the third (c, f, i) columns represent corresponding remnant PMMA and PS after washing with cyclohexane and acetic acid, respectively. Inset Figure b_1 shows nanoring-like structures of PMMA after washing with cyclohexane. The arrows represent the direction of the contact line motion.

Further reduction of the overall concentration of PS/PMMA blend polymer to $0.01\ g\ L^{-1}$ generated micro/nano drops of size $\sim 500\ nm$ to $1.5\ \mu m$ by DCLL (Figure 4.6). After washing with cyclohexane (Figure 4.6 (b)), a cluster of finner PMMA nanodroplets having diameters of the order of $\sim 100\ nm$ was revealed. Around the periphery of the cluster, randomly distributed nanoring-like structures (Figure 4.6 (b_1)) of PMMA with an outer and inner diameter of $\sim 147\ nm$ and $\sim 75\ nm$ respectively, were found.

After washing with acetic acid (Figure 4.6 (c)), nanodroplets of PS having diameters of $\sim 54 - 79\ nm$ were observed. This suggests two things about the morphology of the polymer structures: first, there are patches of PS and PMMA rich thin layers within the droplets (as the bulk of the materials is washed off separately by cyclohexane and acetic acid), and second, the underlayer structures consist of the nanodroplets of PS surrounded by PMMA rim similar to which is reported earlier for relatively thicker films.[3] As the percentage of the PS increased to $75\ \%$, apparently a twin droplet made of one relatively bigger PS (width $\sim 472\ nm$) and one smaller PMMA droplet (width $\sim 236\ nm$) (Figure 4.6 (g) – (i)), was formed and both the droplets were covered by a thin layer of PS sheet. The PS droplet was deposited first in front of the PMMA droplet. PMMA droplet covered with PS sheet appeared as a core-shell-like structure on Si substrate.

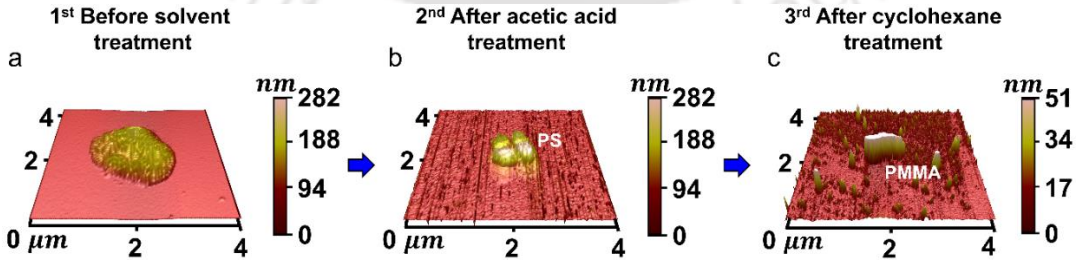

Figure 4.7. (a) AFM images of the PS/PMMA composite micro-drop deposited by DCLL from $0.01\ g\ L^{-1}$ blend solution having PS: PMMA $1:1$ (same as Figure 4.6 (d)). After washing the same droplet with acetic acid PMMA is removed (b) (same as Figure 4.6 (f)). The same acetic acid washed droplet, when subsequently treated with cyclohexane to remove the PS, the underlying nanoscale PMMA structures are revealed (c).

To confirm the patchy multilayers of PS/PMMA inside the droplet with $1:1$ PS/PMMA composition (Figure 4.6(d)), after the first washing with acetic acid, the same sample was subsequently washed with cyclohexane and it was found that the obtained structure diminished in size (both in height and in width) progressively at different stages of subsequent washing with different solvents (Figure 4.7 (a) – (c)). At the first stage, PMMA was removed from the parent droplet (height ~ 162 nm) (Figure 4.7 (a)) and multiple smaller polymer droplets of height ~ 126 nm were revealed (Figure 4.7 (b)), and at the second stage of washing with cyclohexane, PS was removed revealing the further smaller structures of PMMA (Figure 4.7 (c)) with the height of ~ 60 nm. This reveals that the patchy multilayers are covered by the PS sheets and form smaller droplets inside the bigger parent droplet (see inset of Figure 4.6 (d)). It is noticed that PMMA typically tends to form the base layer for the composition PS/PMMA having ratios $1:3$ and $1:1$, due to the higher affinity towards silicon dioxide layer[41] and above this base PMMA, multilayer formation takes place.

One interesting fact is that although the solubility of the PS in toluene ($\sim 1.1\times10^{-3}$ moles L^{-1})[3] is higher than that of PMMA ($\sim 5.8\times10^{-4}$ moles L^{-1}),[36] (see Appendix-1, Figure S1) the deposition of Janus threads or droplets starts with the phase separation and deposition of higher soluble PS rather than less soluble PMMA. This non-intuitive behavior of the deposition from a blend near a three-phase (substrate/blend solution/air) contact line differs from the usual bulk phase separation. As the rate of the evaporation of the solvent (toluene) near the contact line is higher than that of liquid meniscus away from the contact line,[56,57] the solvent from bulk, flows toward the contact line to replenish the solvent due to evaporation. It may plausible that as the PS molecules are more solvated by toluene compared to PMMA, the PS molecules are hauled along with the convective flow of toluene toward the thin liquid film formed near the contact line. Thus, the

local concentration of the PS increases near the contact line, and PS-rich polymeric domain deposits at the front slope of the thread at the beginning of droplet deposition. A schematic of this mechanism is depicted in Figure 4.8 (a) – (c).

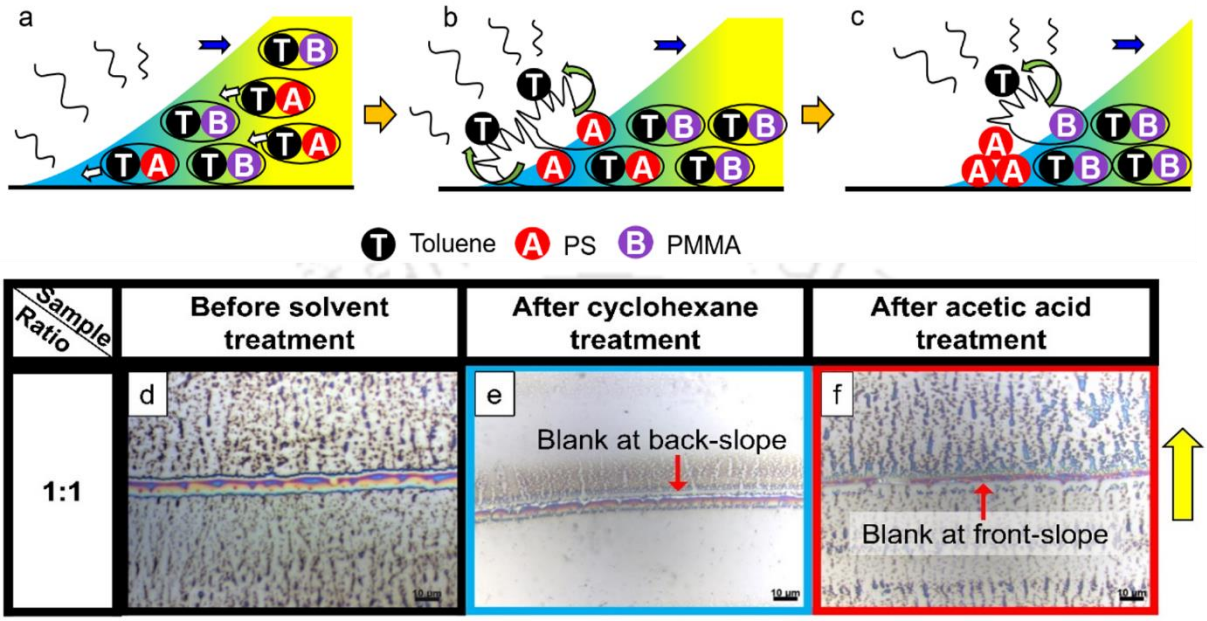

Figure 4.8. (a) Schematic of a plausible mechanism of the more soluble PS deposition at the contact line. More soluble PS (A, red) molecules are solvated in toluene (T, black) and preferentially dragged toward the contact line to replenish the evaporative loss of solvent (b). This leads to PS accumulation to the front side and the less solvated PMMA (B, purple) accumulation to the backside of the deposited features (c). (d) Optical microscope image of deposited micro-thread from PS/PMMA blend polymer solution in ethyl acetate having PS: PMMA ratio of $1:1$ and overall concentration of $1\,\mathrm{g\,L^{-1}}$. Selective solvent etching with cyclohexane and acetic acid leave remnant PMMA (e) and PS (f) respectively. PMMA being more soluble in ethyl acetate, deposits at the front slope in this case. The yellow arrow shows the direction of the contact line movement. All the scale bars represent $10\ \mu\mathrm{m}$.

To validate this hypothesis, a DCLL was performed with $1:1$ PS/PMMA blend solution in ethyl acetate (extra pure, purity: 99.5 %, CAS No.: 141-78-6, Loba Chemie) having $1\,\mathrm{g\,L^{-1}}$ overall polymer concentration at an identical condition of the other experiments. In this case, as the solubility of PS ($\sim 1.9\times10^{-3}$ moles $\mathrm{L^{-1}}$) is less than the solubility of PMMA ($\sim 2.2\times10^{-3}$ moles $\mathrm{L^{-1}}$) in ethyl acetate, the more soluble PMMA was deposited first at the

contact line, thus resulting in Janus thread with a front slope of PMMA and back slope of PS (Figure 4.8 (d)). The PMMA and PS-rich domains in the thread were confirmed by selective solvent etching of the component polymers (Figure 4.8 (e), (f)). Also, as Ethyl Acetate is more volatile than toluene (Vapor pressure of toluene and ethyl acetate are $4.27\times10^{3}\ Pa$ and $1.24\times10^{4}\ Pa$ at the temperature of $25^{\circ}C$,[58] respectively), PS does phase separate from the bulk as well thus forming random PS depositions throughout the surface, which is removed in cyclohexane treatment (Figure 4.8 (e)).

4.4 Conclusions

In summary, we have demonstrated a novel pathway for fabricating Janus micro-thread or micro/nanodroplets of PS/PMMA composite polymers by DCLL, without any physico-chemical guidance. The morphology of deposited lines differs with the variation of PS/PMMA compositions in the blend. Blend having a relatively higher fraction of PMMA ($1:3$ or $1:1$ PS/PMMA ratio) tends to form micro-threads in opposed to low PMMA fraction ($3:1$ PS/PMMA ratio) where almost isolated hemispherical composite microdroplets are found at a polymer concentration of $1\ g\ L^{-1}$. Decreasing polymer concentration tends to form more micro/nanoscale droplets of multi-layered composite polymers or Janus/core-shell microdroplets. Interestingly, it is found that from a polymer blend solution, a more soluble component polymer phase separates first at the contact line due to the higher local concentration of that polymer, which is non-intuitive.

A simple template-less technique to fabricate composite Janus polymeric structures without any sophisticated high-end expensive instrument is presented in this report. Micro-threads or lines/undulated lines generated by this technique can be used in tissue engineering.[59] Due to the larger surface-to-volume ratio, undulated microstructure and nanodroplets can be used for the enhanced yield in any surface-specific reactions or in

patterned microreactors,[60] micro-batteries,[61,62] or in optofluidic devices.[63] This technique has huge potential in surface modifications often required for multiple applications,[64,65] such as dual responsive bio-sensors,[66] organic electronics,[67] flexible displays,[68] etc. Future research in this direction with functional polymers or smart polymers will open up new pathways to revolutionize miniaturized sensor or diagnostic technology.

References

[1] F. S. Bates, *Science (80-.).* **1991**, *251*, 898.

[2] S. Roy, A. Sharma, *J. Colloid Interface Sci.* **2015**, *449*, 215.

[3] A. Pandey, K. Murmu, P. S. Gooh Pattader, *RSC Adv.* **2021**, *11*, 10183.

[4] H. Ogawa, T. Kanaya, K. Nshida, G. Matsuba, *Polymer (Guildf).* **2008**, *49*, 2553.

[5] B. Z. Newby, R. J. Composto, *Macromolecules* **2000**, *33*, 3274.

[6] L. Sung, A. Karim, J. F. Douglas, C. C. Han, *Phys. Rev. Lett.* **1996**, *76*, 4368.

[7] M. Böltau, S. Walheim, J. Mlynek, G. Krausch, U. Steiner, *Nature* **1998**, *391*, 877.

[8] T. Liu, R. Ozisik, R. W. Siegel, *Thin Solid Films* **2007**, *515*, 2965.

[9] L. Fang, M. Wei, C. Barry, J. Mead, *Macromolecules* **2010**, *43*, 9747.

[10] C. W. Wang, M. G. Moffitt, *Chem. Mater.* **2005**, *17*, 3871.

[11] D. Bandyopadhyay, A. Sharma, C. Rastogi, *Langmuir* **2008**, *24*, 14048.

[12] D. Bandyopadhyay, A. Sharma, *J. Phys. Chem. C* **2010**, *114*, 2237.

[13] S. Roy, D. Biswas, N. Salunke, A. Das, P. Vutukuri, R. Singh, R. Mukherjee, *Macromolecules* **2013**, *46*, 935.

[14] C. Ton-That, A. G. Shard, D. O. H. Teare, R. H. Bradley, *Polymer (Guildf).* **2001**, *42*, 1121.

[15] C. Ton-That, A. . Shard, R. . Bradley, *Polymer (Guildf).* **2002**, *43*, 4973.

[16] N. Bhandaru, A. Das, N. Salunke, R. Mukherjee, *Nano Lett.* **2014**, *14*, 7009.

[17] C. Tang, E. M. Lennon, G. H. Fredrickson, E. J. Kramer, C. J. Hawker, *Science (80-.).* **2008**, *322*, 429.

[18] A. Pandey, S. Maity, K. Murmu, S. Middya, D. Bandyopadhyay, P. S. Gooh Pattader, *Nanotechnology* **2021**, *32*, 285302.

[19] H. Lee, B. P. Lee, P. B. Messersmith, *Nature* **2007**, *448*, 338.

[20] X.-Q. Dou, D. Zhang, C. Feng, L. Jiang, *ACS Nano* **2015**, *9*, 10664.

[21] K.-H. Yim, W. J. Doherty, W. R. Salaneck, C. E. Murphy, R. H. Friend, J.-S. Kim, *Nano Lett.* **2010**, *10*, 385.

[22] B. D. Terris, T. Thomson, G. Hu, *Microsyst. Technol.* **2006**, *13*, 189.

[23] T. D. Minh, B.-K. Lee, M.-T. Nguyen-Le, *J. Environ. Manage.* **2018**, *209*, 452.

[24] H. T. Ha, T. D. Minh, H. M. Nguyet, A. K. Sharma, *Korean J. Chem. Eng.* **2021**, *38*, 22.

[25] T. D. Minh, B. Lee, *Environ. Sci. Pollut. Res.* **2018**, *25*, 21901.

[26] J. J. Norman, T. A. Desai, *Ann. Biomed. Eng.* **2006**, *34*, 89.

[27] T. Maitra, C. Antonini, M. Auf der Mauer, C. Stamatopoulos, M. K. Tiwari, D. Poulikakos, *Nanoscale* **2014**, *6*, 8710.

[28] J. B. Boreyko, C.-H. Chen, *Phys. Rev. Lett.* **2009**, *103*, 184501.

[29] P. Roy, R. Mukherjee, D. Bandyopadhyay, P. S. Gooh Pattader, *Nanoscale* **2019**, *11*, 16523.

[30] P. Roy, P. S. Gooh Pattader, *Bull. Mater. Sci.* **2020**, *43*, 169.

[31] M. D. Morariu, N. E. Voicu, E. Schäffer, Z. Lin, T. P. Russell, U. Steiner, *Nat. Mater.* **2003**, *2*, 48.

[32] N. Arun, A. Sharma, P. S. G. Pattader, I. Banerjee, H. M. Dixit, K. S. Narayan, *Phys. Rev. Lett.* **2009**, *102*, 254502.

[33] S. Zhang, T. Shi, J. You, Y. Li, *Polym. Chem.* **2013**, *4*, 3943.

[34] N. Bhandaru, P. S. Goohpattader, D. Faruqui, R. Mukherjee, A. Sharma, *Langmuir* **2015**, *31*, 3203.

[35] J. Aizenberg, P. V. Braun, P. Wiltzius, *Phys. Rev. Lett.* **2000**, *84*, 2997.

[36] K. Murmu, K. P. Burgula, P. S. Gooh Pattader, *J. Colloid Interface Sci.* **2021**, *601*, 156.

[37] K. Tanaka, A. Takahara, T. Kajiyama, *Macromolecules* **1996**, *29*, 3232.

[38] K. Tanaka, A. Takahara, T. Kajiyama, *Macromolecules* **1998**, *31*, 863.

[39] S. Ravati, B. D. Favis, *Polymer (Guildf).* **2010**, *51*, 4547.

[40] Y. Deng, C. Yu, P. Wongwiwattana, N. L. Thomas, *J. Polym. Environ.* **2018**, *26*, 3802.

[41] D. U. Ahn, Z. Wang, I. P. Campbell, M. P. Stoykovich, Y. Ding, *Polymer (Guildf).* **2012**, *53*, 4187.

[42] K. H. Wu, S. Y. Lu, H. L. Chen, *Langmuir* **2006**, *22*, 8029.

[43] S. Walheim, M. Böltau, J. Mlynek, G. Krausch, U. Steiner, *Macromolecules* **1997**, *30*, 4995.

[44] S. Y. Heriot, R. A. L. Jones, *Nat. Mater.* **2005**, *4*, 782.

[45] S. Reich, Y. Cohen, *J. Polym. Sci. Polym. Phys. Ed.* **1981**, *19*, 1255.

[46] X. Liu, N. Bhandaru, M. Banik, X. Wang, A. M. Al-Enizi, A. Karim, R. Mukherjee, *ACS Omega* **2018**, *3*, 2161.

[47] D. Gentili, G. Foschi, F. Valle, M. Cavallini, F. Biscarini, *Chem. Soc. Rev.* **2012**, *41*, 4430.

[48] K. Kargupta, A. Sharma, *Phys. Rev. Lett.* **2001**, *86*, 4536.

[49] A. Sehgal, V. Ferreiro, J. F. Douglas, E. J. Amis, A. Karim, *Langmuir* **2002**, *18*, 7041.

[50] R. Mukherjee, D. Bandyopadhyay, A. Sharma, *Soft Matter* **2008**, *4*, 2086.

[51] M. D. Dickey, S. Gupta, K. A. Leach, E. Collister, C. G. Willson, T. P. Russell, *Langmuir* **2006**, *22*, 4315.

[52] P. S. G. Pattader, I. Banerjee, A. Sharma, D. Bandyopadhyay, *Adv. Funct. Mater.* **2011**, *21*, 324.

[53] H. Yabu, M. Shimomura, *Adv. Funct. Mater.* **2005**, *15*, 575.

[54] A. D. Curtis, A. R. Calchera, M. C. Asplund, J. E. Patterson, *Vib. Spectrosc.* **2013**, *68*, 71.

[55] N. Brun, I. Youssef, M.-C. Chevrel, D. Chapron, C. Schrauwen, S. Hoppe, P. Bourson, A. Durand, *J. Raman Spectrosc.* **2013**, *44*, 909.

[56] R. D. Deegan, O. Bakajin, T. F. Dupont, G. Huber, S. R. Nagel, T. A. Witten, *Nature* **1997**, *389*, 827.

[57] P. Gogoi, A. Chattopadhyay, P. S. Gooh Pattader, *J. Phys. Chem. B* **2020**, *124*, 11530.

[58] M. Gonuguntla, A. Sharma, *Langmuir* **2004**, *20*, 3456.

[59] M. P. O'Brien, M. E. Carnes, R. L. Page, G. R. Gaudette, G. D. Pins, *Curr. Stem Cell Reports* **2016**, *2*, 147.

[60] K. Kusakabe, S. Morooka, H. Maeda, *Korean J. Chem. Eng.* **2001**, *18*, 271.

[61] J. Ni, A. Dai, Y. Yuan, L. Li, J. Lu, *Matter* **2020**, *2*, 1366.

[62] M. Nasreldin, R. Delattre, C. Calmes, M. Ramuz, V. A. Sugiawati, S. Maria, J.-L. de B. de la Tocnaye, T. Djenizian, *Energy Storage Mater.* **2020**, *33*, 108.

[63] W. Menz, S. Dimov, B. Fillon, Eds. , in *4M 2006 - Second Int. Conf. Multi-Material Micro Manuf.*, Elsevier, Oxford, **2006**, pp. i–iii.

[64] J. L. Wu, F. C. Chen, Y. S. Hsiao, F. C. Chien, P. Chen, C. H. Kuo, M. H. Huang, C. S. Hsu, *ACS Nano* **2011**, *5*, 959.

[65] S. Dayal, N. Kopidakis, D. C. Olson, D. S. Ginley, G. Rumbles, *Nano Lett.* **2010**, *10*, 239.

[66] H. Chen, S. Shao, Y. Yu, Y. Huang, X. Zhu, S. Zhang, J. Fan, G. Y. Yin, B. Chi, M. Wan, C. Mao, *Anal. Chim. Acta* **2020**, *1093*, 131.

[67] L. Li, C. Miesch, P. K. Sudeep, A. C. Balazs, T. Emrick, T. P. Russell, R. C. Hayward, *Nano Lett.* **2011**, *11*, 1997.

[68] K. Galatsis, K. L. Wang, M. Ozkan, C. S. Ozkan, Y. Huang, J. P. Chang, H. G. Monbouquette, Y. Chen, P. Nealey, Y. Botros, *Adv. Mater.* **2010**, *22*, 769.

Chapter 5

Solvent Assisted Dewetting of PMMA Thin Film and PS Micro-threads: Fabricated by Dynamic Contact Line Lithography

This page is left blank intentionally

Abstract

A cost-effective fabrication method is demonstrated here to fabricate ordered complex architecture in meso/microscale on a glass surface. The complex structure contains two different polymer components, polystyrene and poly (methyl methacrylate). The method is generic in nature and facilitates on-demand partial or complete dewetted structures to modify the top surface with the help of selective or common solvent vapor treatment, respectively. The dewetted structures by solvent vapor treatment (selective/common) are also compared with thermally dewetted morphology. The topography mainly comprises dewetted meso/ microdroplets of a homopolymer or multiple polymers, where multi-polymer droplets exhibit core-shell structures. The obtained morphologies by solvent and thermal treatment are characterized by optical and atomic force microscopy. A Raman spectroscopy is also performed to identify the particular locations of the polymers after treatment. Transitions of a dewetting process during thermal and solvent treatment are also reported.

5.1 Introduction

The growing demand for micro/nano featured morphology of blend polymer into various technological applications, for example, as a resist in lithography,[1,2] antireflective coating in flexible photovoltaics,[3–5] or in microelectronic industry,[6] optoelectronic industry,[7–9] structure-directing agents to fabricate highly ordered micro/nanoscale featured patterns,[10–13] bio-inspired self-cleaning surfaces,[14–18] smart adhesives,[19,20] smart skins,[21,22] magnetic media,[23–25] and substrates for preferential cell proliferation,[26] etc. are well known. Due to the polymeric phase-separated morphology in micro/nano scale, the blend polymer into various technological applications has been comprehensively investigated over the last few years.[27–32] Several important properties like enhanced roughness of a surface, or well-ordered patterned surfaces, related to the surface chemistry of polymer blend, are advantageous from a

technological point of view. The fabrication of micro/nano features such as core-shell,[33–35] hierarchical,[36–40] multilayer deposition,[12,40–42] alternative deposited structure,[42–44] or 0D, 1D, 2D, and 3D nano-gyroid featured,[45] etc. are substantially dictated by the phase separation of polymers. In general, the initial polymer film thickness, blend ratio, solvent,[46–51] annealing process,[52,53] substrates,[54–56] molecular weight of the polymers,[57] temperature, or pressure,[3,58] etc. affect the phase-separated morphology of polymer blend and can be used as tuning parameters to obtain the desired pattern. Therefore, a better understanding of phase separation in morphological evolution is important.

There are various well-established patterning methods available. Many of these are top-down approaches like photolithography,[59] E-beam lithography,[2] nanoimprinting lithography,[60] capillary force lithography,[36] etc. The bottom-up approaches include self-assembly at the nano to microscale involving dip-coating lithography,[48,59,61] physico-chemical template guided,[30,35,62–67] or template less deposition and/or dewetting,[42,68] external electric field-induced self-assembly,[69–71] etc. Although conventional photolithography and E-beam lithography are the widely used lithographic processes to fabricate micro/nano polymeric patterns, they have their own limitations in terms of resolution and the high cost of the overall fabrication process. Thus, some of the bottom-up approaches are in focus in recent years to fabricate low-cost multiscale complex micro/nanostructures which may involve multiple polymers as well, for various industrial applications.[72–74] Self-assembly is capable of producing well-ordered topographical features in the order of 10 nm using block-co-polymers.[13] Alternate deposited mesoscale features of PS-PMMA have also been generated following the self-assembly of polymers by spin coating on a patterned substrate in a sequential manner.[43] Apart from the spin dewetting,[31,36,75] phase separation of blend polymers is another important route to obtain various types of deposited micro/nano features depending on the blend compositions.[76,77] Earlier, we demonstrated the formation of various types of phase-

separated morphologies of homopolymer on a Si substrate without any physical or chemical guidance by dynamic contact line lithography (DCLL).[68] In that report, we also depicted a tentative phase diagram in terms of the tuning parameters, such as polymer concentrations, and the velocity of the contact line of the driven polymer solution meniscus. Using a polymer blend solution, in another work, we have demonstrated the fabrication of Janus polymeric structure of micro-thread to micro/nanodroplets by DCLL method.[42]

In this report, we target to develop an easy and frugal methodology for the formation of microstructures of different polymers by the combination of DCLL with selective solvent-induced dewetting. Polystyrene (PS) and Poly methyl methacrylate (PMMA) were used as the model polymers. In our earlier reports, we have demonstrated dewetted morphologies of PS/PMMA polymer blend after thermal annealing in a thin film setting,[36] and after contact line deposition.[42] In this work, the PS micro-threads were first fabricated on a PMMA thin film using the DCLL method from an appropriate solvent. On this patterned deposition of polymer, the effect of the thermal annealing, selective and common solvent-induced dewetting, and their morphological evolution were investigated. This gives rise to a myriad of micro/nano features with different polymers that might have huge applications in the smart technologies having multi-functional responses.

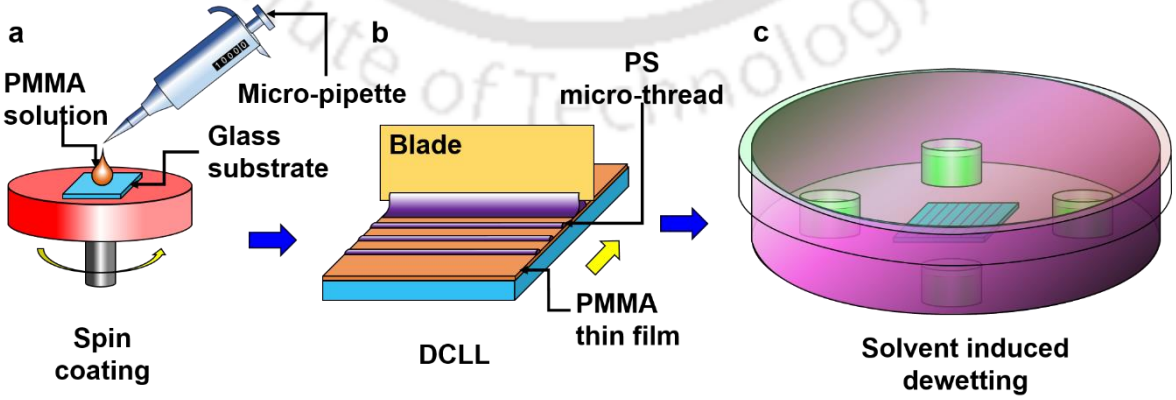

Figure 5.1. The schematic depicts the flow diagram of the experimental sequences: thin film formation – DCLL - solvent-induced dewetting of combined PMMA film and PS micro-threads.

5.2 Materials and Methods

5.2.1 Preparation of Solution

Two types of solutions were prepared: 8.5 g L^{-1} solution of poly (methyl methacrylate) (PMMA) in toluene and 2 g L^{-1} solution of polystyrene (PS) in cyclohexane. Polystyrene (MW ~ 192,000, purity: 99 %, CAS No.: 9003-53-6) and poly (methyl methacrylate) (MW ~ 120,000, purity: 99 %, CAS No.: 9011-14-7) were procured from Sigma Aldrich India and were used as received. The solvents, cyclohexane (extra pure AR, purity: 99.5 %, Cas No.: 110-82-7) and toluene (rectified, purity: 99 %, CAS No.: 108-88-3) were procured from Sisco Research Laboratory and Loba Chemie, respectively.

5.2.2 Preparation of Sample

Figure 5.1 depicts the experimental setup and procedure of solvent-induced patterning. At first, a microscope glass slide (Jain Scientific Glass Works, Ambala (India), Cat no. 597/1) was cut into small square pieces having a dimension of 1.5 cm × 1.5 cm. Next, the glass substrates were spin-coated with prepared PMMA solution, at 5000 rpm for 2 min (Figure 5.1 (a)). This formed a thin layer of PMMA having a thickness of ~ 50 nm, on the glass substrates. Apriori, glass substrates were cleaned rigorously through sonication for 15 min each in sodium dodecyl sulfate (SDS, surfactant) bath followed by acetone and isopropanol bath, sequentially. Finally, glass substrates were rinsed with a copious amount of deionized water (Model No.: Elix-3, Milli-Q; Make: M/s Millipore, USA) and were stored in deionized water. Later, the samples were dried under a flowing nitrogen stream before performing the spin-coating process (Figure 5.1 (a)). After spin coating, the PMMA-coated glass substrates were kept in a vacuum

desiccator for 12 h, to dry the samples thoroughly. These PMMA thin films on glass substrates were used for DCLL using PS solution.

Figure 5.1 (b) depicts the DCLL method, which is elaborated in chapter 3 materials and methods section.[68] Briefly, a customized unidirectional movable stage (MTSZZ-90115-RE25-01, Holmarc, India) was used for DCLL. The glass substrate, coated with PMMA, was fixed on the stage with the help of double-sided tape. A stainless-steel blade (Gilette) was firmly hung vertically above the substrate by keeping a narrow gap of 200 μm in between the lower edge of the blade and the substrate. A 20 μl of PS-cyclohexane solution was dispensed into the gap, and it held the solution perfectly due to the strong capillary force. The cyclohexane being a non-solvent for PMMA, does not affect the PMMA thin film. Next, a servo motor was used to drive the stage at a velocity of 40 μm s^{-1}. The PS solution meniscus was dragged by the vertical blade by the capillary force on the PMMA-coated substrate. The contact line of the solution meniscus was moved to the opposite direction of the stage motion. The contact line moves with an identical average speed to that of the stage, despite the stick-slip periodic fluctuation of the contact line. As the contact line moved, it deposited PS micro-threads onto the thin PMMA film. The selection of the combination of parameters such as the concentration of PS in cyclohexane, and the contact line velocity, were guided by the phase diagram, reported in our earlier study (in chapter 3, Figure 3.4).[68] Later, the final samples were kept in a desiccator for complete drying of the micro-threads, and subsequently, thermal/solvent-assisted dewetting was performed. The purpose of DCLL was to fabricate an ordered pattern of PS micro-threads without affecting the underlying PMMA thin film.

5.2.3 Solvent Assisted / Thermal Dewetting

Figure 5.1 (c) illustrates solvent-assisted dewetting. The sample containing PS micro-threads on the PMMA thin film was kept inside a glass Petri dish. In the same Petri dish, four

containers filled with 360 µl of solvent were also placed beside the test sample. The Petri dish was then covered with a lid for 12 h. This ensures the saturation of air inside the Petri dish with the solvent vapor. The solvent level inside the containers was maintained by adding some fresh solvent whenever the level was reduced by half of the initial. The solvent was chosen appropriately for selective solvent treatment or common solvent treatment, as discussed later. On the other hand, thermal dewetting was performed by placing the sample on a hot plate (Spinot, Tarsons, India), maintaining its temperature at 175℃ for 12 h, and covering it with a lid.

5.2.4 Characterization

The thickness of the thin PMMA film was measured by an ellipsometer (EP3 Nanofilm, Accurion, Germany) with the Cauchy model for fitting the data. The morphologies of the deposited polymers, before and after solvent/ thermal treatment, were captured by light-reflected microscopy (Axio Scope.A1 MAT HAL 100, Carl Zeiss Microscopy, Germany), and by atomic force microscopy (AFM, Bruker, Innova series, Germany) in tapping mode. These provided the topography of the samples at different stages of the experiments. A Raman spectroscopy (Horiba Jobin Vyon, LabRam HR, France) was also performed to identify the specific polymer locations and was supported by selective solvent washing.

5.3 Results and Discussion

5.3.1 Dewetted Morphology

Figure 5.2 depicts the morphologies of PS micro-threads and PMMA films before and after thermal and solvent treatments. The thermal annealing was performed at a temperature of 175℃, which was much higher than the glass transition temperature of PS (100℃),[36] and PMMA (105℃).[36] So, it was expected that the PS and PMMA, both morphologies would be dewetted. But, as the PMMA was much thinner, ~ 50 nm, than the PS micro-thread

(~ 100 nm), therefore, PMMA film was dewetted faster due to the heterogeneous nucleation[51,78] (Figure 5.2 (e)) and formed PMMA microdroplets with a random arrangement.

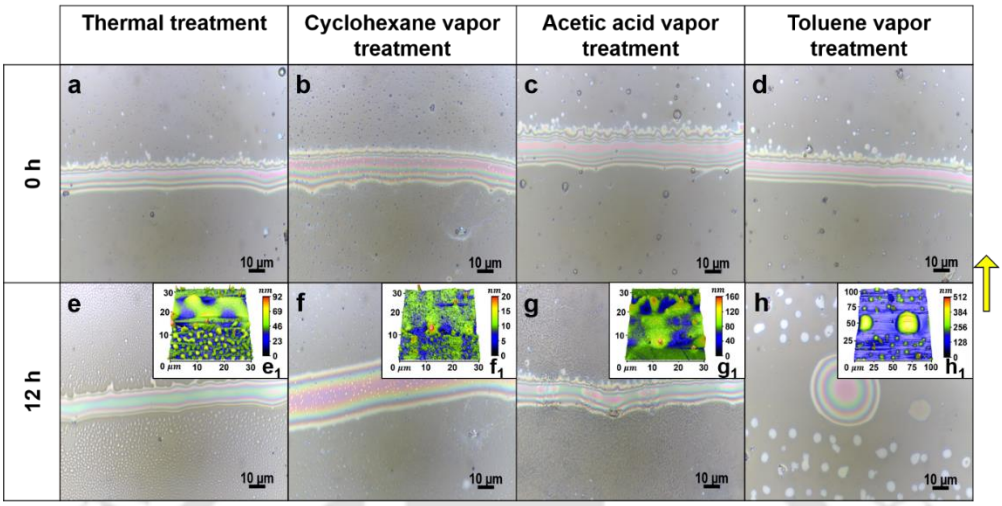

Figure 5.2. The top row (a - d) represents optical images of deposited PS micro-threads on PMMA thin films before any kind of treatment (0 h). The bottom row (e - h) represents optical images of modified morphologies of deposited PS micro-threads on PMMA thin films after treatment for 12h. Inset images (e_1 – h_1) show the AFM height scanned images of respective optical images. The arrow on the right side of the image represents the direction of the contact line motion. All scale bars represent 10 µm.

The heterogeneous nucleation occurs due to the dewetting of a very thin film of PS present near the sides of the PS micro-threads. This thin film eventually disintegrates into small droplets of PS. These small dewetted PS droplets act as nucleation sites for the subsequent dewetting of PMMA thin film. Thus, both PS and PMMA microdroplets were observed on both sides of the PS micro-thread. On the other hand, the PS micro-threads initially spread a bit and then underwent incomplete dewetting and thus formed slightly undulated PS micro-threads after 12 h of thermal annealing (Figure 5.2 (e_1)). The PS/PMMA bond strength might be responsible for this incomplete dewetted structure. In another study by Yiqiang Fan et al.[79] reported that the bond strength between PS and PMMA increased with increasing bond temperature. The authors prepared a few samples by varying the temperature from 110 ℃ *to* 125 ℃, where the samples contained PS film (thickness of 1.2 mm) and PMMA film

(thickness of 1 mm) are attached to each other. Bonding strength was characterized and the result showed that the bond strength increased with bond temperature. Therefore, this could be the reason that the PS undergoes an incomplete dewetting even at 175℃ in the present case. On other side, PMMA has a great affinity towards the Si/glass substrate, and this also makes the underneath PMMA film as an incomplete dewetted structure.

Cyclohexane vapor treatment only affected the PS micro-thread by changing the width only (Figure 5.2 (f)). As the micro-thread absorbed the solvent vapor, it started to spread, and eventually, height of the micro-thread decreased. No dewetted morphology was observed of micro-thread even after more than 12 h by cyclohexane vapor treatment. Few PS droplets were observed near the micro-thread due to the dewetting of a very thin residual PS layer on the PMMA film. The PMMA film remained unaffected by the cyclohexane vapor. Figure 2 (g) depicts the morphology of PMMA film and PS micro-thread after acetic acid vapor treatment. The PMMA thin film was dewetted by nucleation dewetting; on the other hand, the PS micro-thread remained unaffected. The dewetted features of PMMA film were random, and microdroplets to labyrinth-like structures were formed.

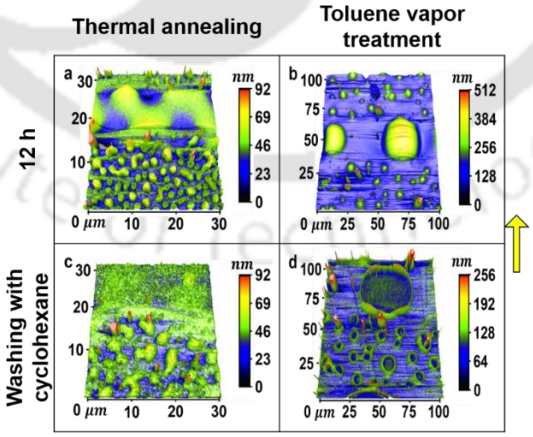

Figure 5.3. The top row shows the AFM height scanned images of (a) thermally annealed and (b) toluene vapor treated samples after 12 h. The bottom row shows the morphology after washing with cyclohexane of the previous (c) thermally annealed and (d) toluene vapor treated samples. The arrow on the right side of the image represents the direction of the contact line motion.

Treatment with common solvents like toluene induced dewetting of both the polymers by forming microdroplets (Figure 5.2 (h)) on the substrate. In that case, the PS micro-threads also underwent complete dewetting and formed big droplets of diameter ~ 35 μm arranged in a straight line. Small dewetted droplets of PS (diameter ~ 12 μm) were placed randomly on both sides of the line having the big PS droplets. As PMMA film also dewetted completely, it formed a rim surrounding all the PS droplets.

5.3.2 Cyclohexane Washing

Cyclohexane washing was performed to the samples to verify the arrangements of both the polymers in the dewetted structures after thermal annealing and toluene vapor treatment (Figure 5.3). The cyclohexane being a good solvent for PS and non-solvent for PMMA, the washing took away all the PS from the samples leaving the PMMA undisturbed. Figure 3 (c), the AFM image depicts the morphology after washing with cyclohexane of thermally annealed samples. This shows that the micro-thread is etched out due to the dissolution of PS into the cyclohexane and the dewetted features of PMMA film remain undisturbed. In that case, as the dewetting of PS and PMMA was not completed, it did not form any PS droplet surrounded by the PMMA rim. Individual PS and PMMA droplets were formed on the sides of the micro-thread due to the thermal dewetting of the thin films. The PS droplets formed by thermal dewetting were washed away by the cyclohexane treatment, and PMMA droplets remained. Thus, we can see fewer droplets in Figure 5.3 (c) than in Figure 5.3 (a). The micro-thread being sufficiently thick, it underwent incomplete thermal dewetting, thus forming a slightly undulated structure with a relatively larger width due to spreading. Xue Li and other co-authors have reported experimentally that a thicker film requires more duration to dewet than a somewhat thinner film due to the strong van der Waals interactions between the interfaces of the polymers/air and the polymer/substrate.[80] Besides this, they have also reported that the attractive nature of PMMA towards Si substrate restricts the mobility of polymer molecules

and does slow down the dewetting process of PMMA film. However, in the present scenario, the annealing temperature is relatively higher (175℃), which enables the ~ 50 nm thin PMMA film to dewet.

In the case of the toluene-vapor treated sample, it was seen that there were several ring-like structures of PMMA after washing with cyclohexane (Figure 5.3 (d)). Comparatively bigger ring-like structures of PMMA remained due to the dissolution of PS from the core of the microdroplets formed by dewetting of micro-threads. The smaller ring-like structures of PMMA were formed by the dissolution of PS from the core of the smaller polymeric droplets. This cyclohexane washing revealed that after complete dewetting by the common solvent toluene, PS-core/PMMA-rim-like microdroplets were formed. The PS cores of the small droplets were formed by dewetting the ultrathin film of PS, which was deposited on PMMA film during DCLL process. A Raman spectroscopy was also performed to locate the specific regions of PS and PMMA (Figure 5.4).

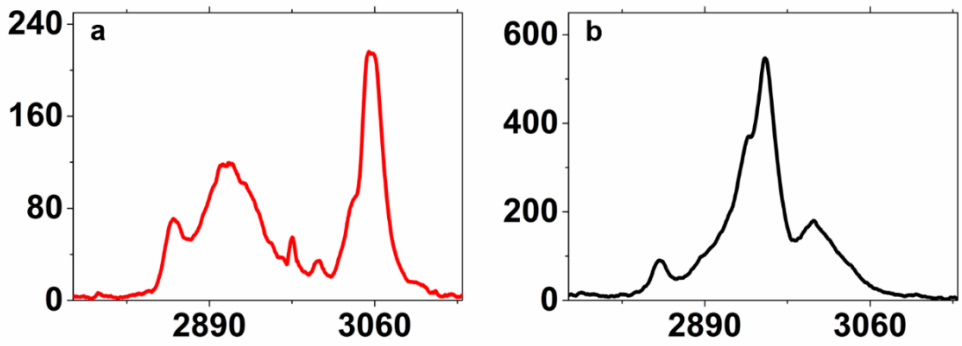

Figure 5.4. represents the Raman spectrum of (a) PS in the core and (b) PMMA as a shell of dewetted microdroplets which are formed by dewetting of PS micro-thread on PMMA thin film due to toluene vapor treatment for 12 h.

A sample, after 12 h toluene vapor treatment, was used to perform Raman spectroscopy. Figure 5.4 (a) depicts the prominent Raman peaks of PS at the core of the micro-droplet at ~ 2853 cm^{-1}, ~ 2910 cm^{-1} and ~ 3054 cm^{-1} due to the CH_2 stretching of the aliphatic

group, vibrations of tertiary CH stretching and CH stretching of the aromatic ring, respectively.[81,82] At the peripheral rim of the droplet, a notable Raman peak of PMMA at $\sim 2952\ cm^{-1}$ was observed due to the vibration of C-H stretching (Figure 5.4 (b)).[36]

5.3.3 Dewetting Transition

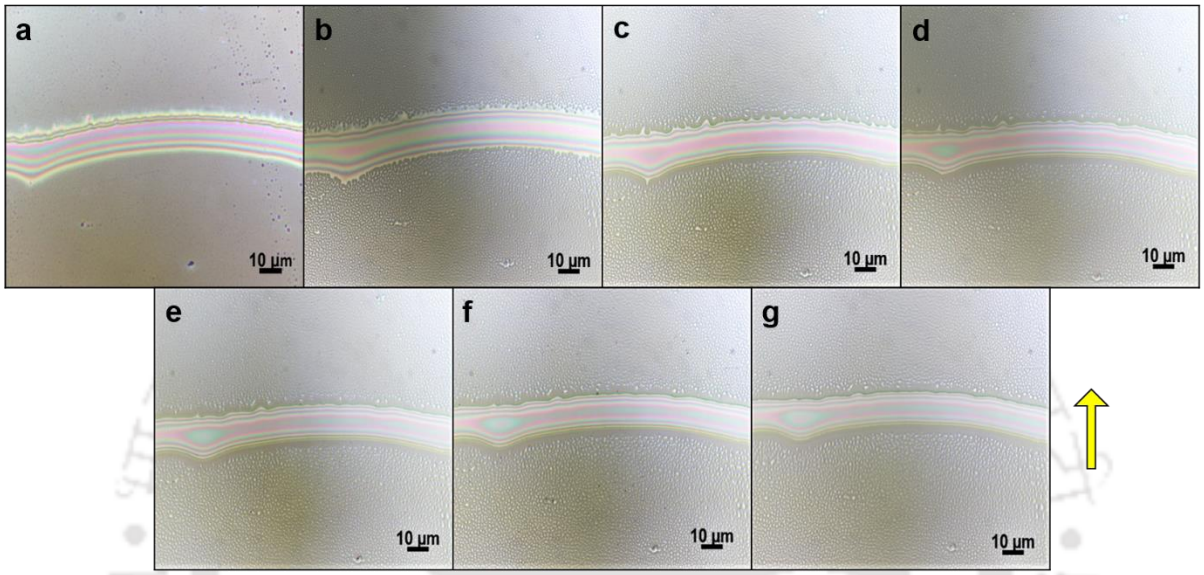

Figure 5.5. The transition of dewetted morphology of thermally annealed sample at (a) 0 min, (b) 40 min, (c) 240 min, (d) 360 min, (e) 480 min, (f) 600 min, and (g) 680 min. The arrow depicts the direction of contact line movement. All scale bars represent 10 µm.

A transition of dewetted morphology was also captured at different time scales when thermal annealing was applied (Figure 5.5). The images were captured using an optical microscope in a bright field mode. Before taking each image, the sample was taken out from the hotplate. After capturing the image of the same region, the sample was quickly placed back onto the hotplate again. This whole process took less than 30 sec to complete. After the initial rapid phase of dewetting in the first 40 min, the dewetted PMMA features try to reassemble themselves slowly into a thermodynamically more favorable condition by disintegrating a few comparatively bigger droplets and by detaching from the PS micro-thread only. And eventually, this does not change the overall morphology majorly. On the other hand, the PS

micro-thread remained not much affected. Initially, its width spread slightly (+2 μm) within the period of first 40 *min* (Figure 5.5 (b)). After that, an almost negligible decrease in width was observed (−2.5 μm), and simultaneously, an undulation of the micro-threads also started to appear after 360 min (Figure 5.5 (d)). This morphology remained nearly unchanged till 680 *min* (Figure 5.5 (g)).

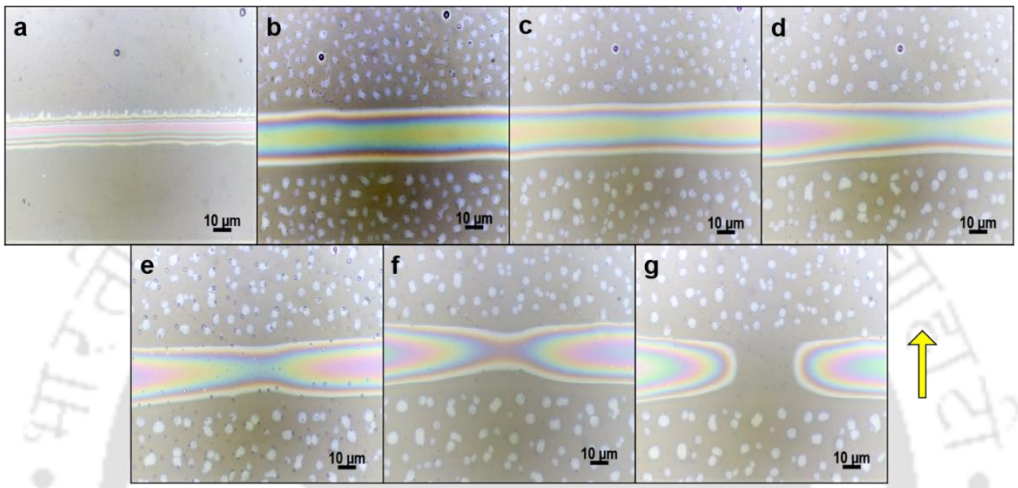

Figure 5.6. Transition of dewetted morphology of toluene vapour treated sample at (a) 0 min, (b) 40 min, (c) 240 min, (d) 360 min, (e) 480 min, (f) 600 min and (g) 680 min. The arrow depicts the direction of contact line movement. All scale bars represent 10 μm.

The evolution of the dewetted morphology was also monitored during the toluene vapor treatment (Figure 5.6). Here also, the significant dewetting of the film occurred within ~ 40 min, and the dewetted micro-droplets of PMMA and PS (due to the dewetting of the thin PS overlayer on PMMA) were formed. The coarsening of the dewetted droplets takes place as time progress, and the droplets get bigger and lesser in numbers which is evident in Figures 5.6 (b), 5.6 (e) to 5.6 (g). After an initial 40 min, the PS micro-thread started spreading, and almost got double its initial width (Figure 5.6 (b)). This initial spreading was followed by the dewetting process and initiated by narrowing down the thread at around 360 min (Figure 5.6 (c)). In the end, to reach a thermodynamically favorable state, the micro-thread disintegrated into several

microdroplets (Figure 5.6 (g)). Here, one thing should be noticed that all sizes of microdroplets (droplets from PS micro-thread and droplets from PS/PMMA thin-film region) contain both the polymers, as toluene is a suitable and common solvent for both PS and PMMA. PS forms the core and PMMA surrounds the PS with a rim formation.

5.3. Conclusions

In this article, we have reported a facile method to fabricate the semi-ordered core-shell complex meso/microstructure of PS and PMMA. The process starts with the fabrication of PS micro-thread on PMMA thin film, where PS micro-threads act as a structure-directing component when dewetting occurs. The PS thread on PMMA film was prepared by the DCLL method by selecting a suitable solvent. Here, PMMA forms a shell/rim and PS remains as a core in a single entity (meso/microdroplets) when the samples are treated with common solvent vapor, toluene. On the other hand, the thermal treatment induced incomplete dewetting that resulted in the dewetted structure of the thin film into microdroplets, but undewetted PS micro-threads remained almost as it is. If desired, one can create a complementary pattern by creating PMMA micro-threads on PS thin film. In that case, one can expect that the thermal dewetting of this sample will form PS droplets on both sides of a PMMA micro-thread. Furthermore, we have demonstrated that the selective solvent vapor treatment allows dewetting of particular regions when another component remains undisturbed. This work demonstrates that the combination of spin coating, DCLL, and solvent vapor or thermal treatment can be a frugal methodology for the fabrication of complex meso/ microstructured surfaces for dual responsive sensors,[83] energy conversion and storage devices,[84][85] fuel cell or lithium cell industry,[86][87] and perovskite structure with multi-material for photovoltaic application,[88,89] etc.

References

[1] S. Ma, C. Con, M. Yavuz, B. Cui, *Nanoscale Res. Lett.* **2011**, *6*, 1.

[2] A. Pandey, S. Maity, K. Murmu, S. Middya, D. Bandyopadhyay, P. S. Gooh Pattader, *Nanotechnology* **2021**, *32*, 285302.

[3] L. Xue, J. Zhang, Y. Han, *Prog. Polym. Sci.* **2012**, *37*, 564.

[4] X. Li, J. Gao, L. Xue, Y. Han, *Adv. Funct. Mater.* **2010**, *20*, 259.

[5] S. Walheim, E. Schäffer, J. Mlynek, U. Steiner, *Science (80-.).* **1999**, *283*, 520.

[6] Y. Li, L. Huang, M. Zhong, Z. Wei, J. Li, *Adv. Mater. Technol.* **2016**, *1*, 1600001.

[7] R. P. Tennant, D. M. Koch, T. L. Mulgrew, P. P. Gnall, *J. Vac. Sci. Technol. B Microelectron. Nanom. Struct.* **1992**, *10*, 2530.

[8] K.-H. Yim, W. J. Doherty, W. R. Salaneck, C. E. Murphy, R. H. Friend, J.-S. Kim, *Nano Lett.* **2010**, *10*, 385.

[9] P. F. Dix, C. Mckee, *J. Vac. Sci. Technol. B Microelectron. Nanom. Struct.* **1992**, *10*, 2667.

[10] T. Yanagisawa, T. Shimizu, K. Kuroda, C. Kato, *Bull. Chem. Soc. Jpn.* **1990**, *63*, 988.

[11] C. T. Kresge, M. E. Leonowicz, W. J. Roth, J. C. Vartuli, J. S. Beck, *Nature* **1992**, *359*, 710.

[12] M. Stefik, S. Mahajan, H. Sai, T. H. Epps, F. S. Bates, S. M. Gruner, F. J. DiSalvo, U. Wiesner, *Chem. Mater.* **2009**, *21*, 5466.

[13] D. Zhao, Q. Huo, J. Feng, B. F. Chmelka, G. D. Stucky, *J. Am. Chem. Soc.* **1998**, *120*, 6024.

[14] M. Ma, R. M. Hill, J. L. Lowery, S. V. Fridrikh, G. C. Rutledge, *Langmuir* **2005**, *21*, 5549.

[15] J. T. Han, X. Xu, K. Cho, *Langmuir* **2005**, *21*, 6662.

[16] K. Liu, L. Jiang, *Nano Today* **2011**, *6*, 155.

[17] D. Adak, S. Ghosh, P. Chakraborty, K. M. K. Srivatsa, A. Mondal, H. Saha, R. Mukherjee, R. Bhattacharyya, *Sol. Energy Mater. Sol. Cells* **2018**, *188*, 127.

[18] N. A. Gengec, U. Cengiz, H. Y. Erbil, *Appl. Surf. Sci.* **2016**, *383*, 33.

[19] H. Lee, B. P. Lee, P. B. Messersmith, *Nature* **2007**, *448*, 338.

[20] X.-Q. Dou, D. Zhang, C. Feng, L. Jiang, *ACS Nano* **2015**, *9*, 10664.

[21] T. Maitra, C. Antonini, M. Auf der Mauer, C. Stamatopoulos, M. K. Tiwari, D. Poulikakos, *Nanoscale* **2014**, *6*, 8710.

[22] J. B. Boreyko, C.-H. Chen, *Phys. Rev. Lett.* **2009**, *103*, 184501.

[23] B. D. Terris, T. Thomson, G. Hu, *Microsyst. Technol.* **2006**, *13*, 189.

[24] O. Hellwig, J. K. Bosworth, E. Dobisz, D. Kercher, T. Hauet, G. Zeltzer, J. D. Risner-

Jamtgaard, D. Yaney, R. Ruiz, *Appl. Phys. Lett.* **2010**, *96*, 052511.

[25] S. Xiao, X. Yang, E. W. Edwards, Y.-H. La, P. F. Nealey, *Nanotechnology* **2005**, *16*, S324.

[26] J. J. Norman, T. A. Desai, *Ann. Biomed. Eng.* **2006**, *34*, 89.

[27] H. Ogawa, T. Kanaya, K. Nshida, G. Matsuba, *Polymer (Guildf).* **2008**, *49*, 2553.

[28] B. Z. Newby, R. J. Composto, *Macromolecules* **2000**, *33*, 3274.

[29] L. Sung, A. Karim, J. F. Douglas, C. C. Han, *Phys. Rev. Lett.* **1996**, *76*, 4368.

[30] M. Böltau, S. Walheim, J. Mlynek, G. Krausch, U. Steiner, *Nature* **1998**, *391*, 877.

[31] T. Liu, R. Ozisik, R. W. Siegel, *Thin Solid Films* **2007**, *515*, 2965.

[32] L. Fang, M. Wei, C. Barry, J. Mead, *Macromolecules* **2010**, *43*, 9747.

[33] D. Bandyopadhyay, A. Sharma, C. Rastogi, *Langmuir* **2008**, *24*, 14048.

[34] D. Bandyopadhyay, A. Sharma, *J. Phys. Chem. C* **2010**, *114*, 2237.

[35] S. Roy, D. Biswas, N. Salunke, A. Das, P. Vutukuri, R. Singh, R. Mukherjee, *Macromolecules* **2013**, *46*, 935.

[36] A. Pandey, K. Murmu, P. S. Gooh Pattader, *RSC Adv.* **2021**, *11*, 10183.

[37] J. Feng, M. T. Tuominen, J. P. Rothstein, *Adv. Funct. Mater.* **2011**, *21*, 3715.

[38] Y. Chen, *Microelectron. Eng.* **2015**, *135*, 57.

[39] D. J. Carbaugh, S. Kaya, F. Rahman, *J. Vac. Sci. Technol. B, Nanotechnol. Microelectron. Mater. Process. Meas. Phenom.* **2017**, *35*, 011601.

[40] T. S. Bailey, C. M. Hardy, T. H. Epps, F. S. Bates, *Macromolecules* **2002**, *35*, 7007.

[41] C. A. Tyler, J. Qin, F. S. Bates, D. C. Morse, *Macromolecules* **2007**, *40*, 4654.

[42] K. Murmu, A. Pandey, P. Roy, A. Deb, P. S. Gooh Pattader, *J. Appl. Polym. Sci.* **2022**, *139*, 1.

[43] N. Bhandaru, A. Das, N. Salunke, R. Mukherjee, *Nano Lett.* **2014**, *14*, 7009.

[44] C. Tang, E. M. Lennon, G. H. Fredrickson, E. J. Kramer, C. J. Hawker, *Science (80-.).* **2008**, *322*, 429.

[45] B.-K. Cho, A. Jain, S. M. Gruner, U. Wiesner, *Science (80-.).* **2004**, *305*, 1598.

[46] J. S. Chiou, J. W. Barlow, D. R. Paul, *J. Polym. Sci. Part B Polym. Phys.* **1987**, *25*, 1459.

[47] J. J. Schmidt, J. A. Gardella, L. Salvati, *Macromolecules* **1989**, *22*, 4489.

[48] K. Tanaka, J.-S. Yoon, A. Takahara, T. Kajiyama, *Macromolecules* **1995**, *28*, 934.

[49] P. Cyganik, A. Budkowski, U. Steiner, J. Rysz, A. Bernasik, S. Walheim, Z. Postawa, J. Raczkowska, *Europhys. Lett.* **2003**, *62*, 855.

[50] G. Krausch, C. A. Dai, E. J. Kramer, J. F. Marko, F. S. Bates, *Macromolecules* **1993**, *26*, 5566.

[51] R. Seemann, S. Herminghaus, K. Jacobs, *Phys. Rev. Lett.* **2001**, *86*, 5534.

[52] S. Coveney, *Fundamentals of Phase Separation in Polymer Blend Thin Films*, Springer International Publishing, Cham, **2015**.

[53] D. U. Ahn, Z. Wang, I. P. Campbell, M. P. Stoykovich, Y. Ding, *Polymer (Guildf).* **2012**, *53*, 4187.

[54] Z. Shou, A. Chakrabarti, *Polymer (Guildf).* **2001**, *42*, 6141.

[55] Z. Zhang, L. Wang, Y. Ding, *Langmuir* **2013**, *29*, 3073.

[56] S. Walheim, M. Böltau, J. Mlynek, G. Krausch, U. Steiner, *Macromolecules* **1997**, *30*, 4995.

[57] X. Li, Y. Han, L. An, *Polymer (Guildf).* **2003**, *44*, 8155.

[58] Z. Zhang, Z. Wang, Y. Ding, *Polymer (Guildf).* **2014**, *55*, 4150.

[59] A. Pimpin, W. Srituravanich, *Eng. J.* **2012**, *16*, 37.

[60] Z. Wang, D. U. Ahn, Y. Ding, *Langmuir* **2010**, *26*, 14909.

[61] S. Reich, Y. Cohen, *J. Polym. Sci. Polym. Phys. Ed.* **1981**, *19*, 1255.

[62] C. Ton-That, A. . Shard, R. . Bradley, *Polymer (Guildf).* **2002**, *43*, 4973.

[63] X. Liu, N. Bhandaru, M. Banik, X. Wang, A. M. Al-Enizi, A. Karim, R. Mukherjee, *ACS Omega* **2018**, *3*, 2161.

[64] D. Gentili, G. Foschi, F. Valle, M. Cavallini, F. Biscarini, *Chem. Soc. Rev.* **2012**, *41*, 4430.

[65] K. Kargupta, A. Sharma, *Phys. Rev. Lett.* **2001**, *86*, 4536.

[66] A. Sehgal, V. Ferreiro, J. F. Douglas, E. J. Amis, A. Karim, *Langmuir* **2002**, *18*, 7041.

[67] R. Mukherjee, D. Bandyopadhyay, A. Sharma, *Soft Matter* **2008**, *4*, 2086.

[68] K. Murmu, K. P. Burgula, P. S. Gooh Pattader, *J. Colloid Interface Sci.* **2021**, *601*, 156.

[69] M. D. Morariu, N. E. Voicu, E. Schäffer, Z. Lin, T. P. Russell, U. Steiner, *Nat. Mater.* **2003**, *2*, 48.

[70] M. D. Dickey, S. Gupta, K. A. Leach, E. Collister, C. G. Willson, T. P. Russell, *Langmuir* **2006**, *22*, 4315.

[71] P. S. G. Pattader, I. Banerjee, A. Sharma, D. Bandyopadhyay, *Adv. Funct. Mater.* **2011**, *21*, 324.

[72] U. Bach, D. Lupo, P. Comte, J. E. Moser, F. Weissörtel, J. Salbeck, H. Spreitzer, M. Grätzel, *Nature* **1998**, *395*, 583.

[73] M. Grätzel, *MRS Bull.* **2005**, *30*, 23.

[74] H. J. Snaith, L. Schmidt-Mende, *Adv. Mater.* **2007**, *19*, 3187.

[75] S. Roy, A. Sharma, *J. Colloid Interface Sci.* **2015**, *449*, 215.

[76] S. Ravati, B. D. Favis, *Polymer (Guildf).* **2010**, *51*, 4547.

[77] Y. Deng, C. Yu, P. Wongwiwattana, N. L. Thomas, *J. Polym. Environ.* **2018**, *26*, 3802.

[78] S. Roy, D. Bandyopadhyay, A. Karim, R. Mukherjee, *Macromolecules* **2015**, *48*, 373.

[79] Y. Fan, H. Li, Y. Yi, I. G. Foulds, *Microsyst. Technol.* **2014**, *20*, 59.

[80] X. Li, Y. Han, L. An, *Appl. Surf. Sci.* **2004**, *230*, 115.

[81] A. D. Curtis, A. R. Calchera, M. C. Asplund, J. E. Patterson, *Vib. Spectrosc.* **2013**, *68*, 71.

[82] N. Brun, I. Youssef, M.-C. Chevrel, D. Chapron, C. Schrauwen, S. Hoppe, P. Bourson, A. Durand, *J. Raman Spectrosc.* **2013**, *44*, 909.

[83] H. Chen, S. Shao, Y. Yu, Y. Huang, X. Zhu, S. Zhang, J. Fan, G. Y. Yin, B. Chi, M. Wan, C. Mao, *Anal. Chim. Acta* **2020**, *1093*, 131.

[84] M. C. Orilall, N. M. Abrams, J. Lee, F. J. DiSalvo, U. Wiesner, *J. Am. Chem. Soc.* **2008**, *130*, 8882.

[85] G. G. Wallace, J. Chen, A. J. Mozer, M. Forsyth, D. R. MacFarlane, C. Wang, *Mater. Today* **2009**, *12*, 20.

[86] R. P. O'Hayre, S.-W. Cha, W. Colella, F. B. Prinz, *Fuel Cell Fundamentals*, John Wiley & Sons, New Jersey, **2005**.

[87] J. Lee, Y. S. Jung, S. C. Warren, M. Kamperman, S. M. Oh, F. J. DiSalvo, U. Wiesner, *Macromol. Chem. Phys.* **2011**, *212*, 383.

[88] X. Chang, J. Fang, Y. Fan, T. Luo, H. Su, Y. Zhang, J. Lu, L. Tsetseris, T. D. Anthopoulos, S. Liu, K. Zhao, *Adv. Mater.* **2020**, *2001243*, 1.

[89] K. Lee, J. Moon, J. Jeong, S. W. Hong, *Materials (Basel).* **2021**, *14*, 6824.

Chapter 6

Self-assembled PVDF micro-threads with β-phase crystallinity; induced by dynamic contact line lithography coupled with electric field

This page is left blank intentionally

Abstract

Dynamic contact line lithography (DCLL) coupled with an electric field (EF) to fabricate PVDF micro-thread with enhanced β-phase, responsible for the piezoelectric effect, is demonstrated here. The applied electric field is as low as $7\ \mathrm{V/\mu m}$, far lower than the conventional electrical poling ($\sim 2\ \mathrm{kV/\mu m}$) and electrospinning method. The micro-threads are deposited on a flexible PET substrate from a solution of polyvinylidene fluoride (PVDF) in dimethylformamide (DMF) having a concentration of $1\ \mathrm{mg\ ml^{-1}}$. The contact line velocity of the solution is $40\ \mu\mathrm{m\ s^{-1}}$. The highest applied electric field of $\sim 14\ \mathrm{V\ \mu m^{-1}}$ (1000 V) induces the maximum amount of β-phase in the deposited micro-threads. Without an electric field, α-phase is formed, which is not piezoelectric in nature. The lowest electric field intensity, that induces the piezoelectric effect is $\sim 7\ \mathrm{V\ \mu m^{-1}}$ (500 V). The amount of converted β-phase (β to α ratio) of the prepared samples from dynamic contact line lithography coupled with an electric field is compared with fabricated samples from thermal annealing (at different temperatures) and electrospinning process (at 19 kV). An FTIR and Raman spectroscopy is used to characterize the thermally annealed and electrospun samples. On the other hand, only Raman spectroscopy is used to characterize the samples fabricated from DCLL coupled with EF. Finally, the piezoelectric property of the deposited micro-threads is demonstrated by recording the output voltage against applied mechanical stress.

6.1 Introduction

Polyvinylidene difluoride (PVDF) and its copolymers have been considered as the most demanded organic dielectric materials for their excellent ferroelectric and piezoelectric properties compared to their counterparts diisopropyl ammonium bromide (DIPA-B),[1] nylon-11,[2] and croconic acid.[3] Inorganic piezoelectric materials, such as PZT (Lead-Zirconium-Titanate) and barium titanate have received massive attention among other inorganic materials

due to their remarkable energy conversion efficiency and high piezoelectric strain constants.[4–7] However, the processing of inorganic piezoelectric devices is relatively expensive and more cumbersome than polymeric piezoelectric materials, especially for flexible devices.[8,9] Furthermore, to avoid the presence of any toxic metal,[10] PVDF and its copolymer are possibly the best alternatives in this field. Due to their impressive piezoelectric properties, PVDF and its copolymer have been pioneered for more than two decades[11] in various applications such as energy harvesting,[12–16] nanogenerators,[17,18] sensing applications like pressure sensors,[19] high-sensitivity acoustic sensors,[20] biosensors,[21] motion trackers,[22,23] and accelerometers[24] etc.

Depending upon the chain conformations and packing of molecules, five different phases of crystallized PVDF have been reported.[25] There are *trans* (T) and *gauche* (G) conformations in the PVDF polymer chains. β-phase exhibits all-trans ($TTTT$) conformation, α and δ-phase show $TG^{+}TG^{-}$, while γ and ϵ-phase are $TTTG^{+}TTTG^{-}$.[16,26–29] To get the significant piezoelectric effect, the maximum phase with all-trans (β-phase) chain conformation is necessary. Thus, the fabrication of PVDF samples with a high fraction of β-phase having piezo-, pyro-, and ferroelectric properties, is the primary goal for any practical application. There are various techniques to achieve high β-phase, such as thermal annealing and crystallization, poling under a high voltage power supply, mechanical stretching, use of hydrated metal salt and doping of additives into the PVDF matrix, etc.[11,14,18,25,30–34] Among several recent approaches, the electrospinning process[18,35–39] is viral as it offers a promising and reliable outcome. The combination of high electrical poling and at the same time electromechanical stretching provides the highest possible β-phase crystallinity into the fibers matrix. Spin-coating,[17,23,30,40,41] drop-casting,[36] melting process,[32,42] printing from piezoelectric ink[43] and Langmuir-Blodgett,[40,44] etc. also have been explored for fabricating polymer films with piezoelectric effect.

Micro/nanostructures with functional properties are essential for smart miniaturized devices/sensors having multipurpose capabilities.[45,46] Fabrication of ordered micro/nanostructures is challenging and often requires high-end expensive equipment such as electron beam lithography (EBL), photolithography, mask writer, atomic layer deposition (ALD), chemical vapor deposition (CVD), etc. Recently, we have demonstrated the ordered deposition of polymer micro/nanostructures from the carefully driven contact line of a solution via phase separation.[47] The process is called dynamic contact line lithography (DCLL) that does not require any sophisticated high-end equipment, and has the potential for industrial applications.

In this article, we report the modified DCLL in the presence of electric field that allows the poling of PVDF micro-threads during the fabrication of the ordered structures from PVDF in dimethylformamide (DMF) solution. The applied electric field is much lower than that used in the conventional PVDF poling or in the electrospinning process. There are only a few reports on phase-separation-mediated PVDF crystallization.[31,48] Often, to achieve improved piezoelectric effects, either copolymers such as polyvinylidene fluoride-trifluoroethylene (PVDF-TrFE) or doping of foreign materials such as carbon nanotubes were used.[31,48] In general, copolymer PVDF-TrFE is found to have higher β-phase crystallinity due to the steric effect of TrFE,[49–51] whereas PVDF alone, without any treatment, predominantly contains α-phase. Due to this low fraction of β-phase, the piezoelectric effect of PVDF alone is not so promising. However, there are few reports suggesting the toxic effect of TrFE monomer and the difficulty in transportation and storage of this expensive monomer, making us think twice for environmentally friendly PVDF only.[52,53] Therefore, in this article, we attempt to decorate a flexible PET surface with the micro-threads of PVDF, and at the same time, we tried to improve the β-phase crystallinity of these PVDF micro-threads using a modified DCLL method. Earlier reports on mechanical stretching or electrical poling, coupled with thermal

annealing of PVDF film[54,55] suggest the increase in crystallinity due to the enhanced mobility of PVDF molecules. In this modified DCLL process, while micro-threads are being deposited from PVDF-DMF solution, a low applied electric field of 3 V/μm is found to be sufficient to align the PVDF molecules easily, compared to the electrospinning or any other electrical poling method.[56,57]

6.2 Experimental Section

6.2.1 Solution Preparation

Two different solutions having concentrations of 200 mg ml^{-1} (solution-1) and 1 mg ml^{-1} (solution-2) of PVDF into dimethylformamide (DMF) were prepared by stirring and heating the solutions at a temperature of 70℃ until the solutions were homogeneous and transparent. Solution-1 (higher concentration) was used to obtain a uniform PVDF film during spin coating, without spin dewetting. Similarly, to obtain proper microfibers using the electrospinning method, solution-1 was used. Solution-2 was used to deposit PVDF micro-threads on a flexible polyethylene terephthalate (PET) sheet using DCLL (discuss later).[47] PVDF (MW ~ 180,000) and DMF (analytical grade) were procured from Sigma Aldrich and Himedia, respectively. A stainless-steel blade (Gillette) was purchased from a local shop. ITO-coated PET sheet was purchased from Silpent-India and was used without any modification.

6.2.2 PVDF Micro-threads by DCLL Coupled with Electric Field

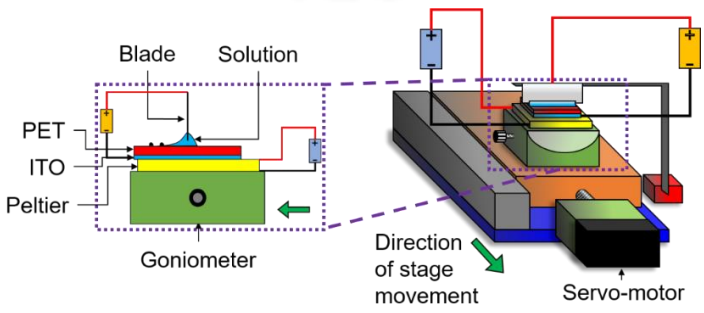

Figure 6.1. The schematic diagram depicts the experimental setup and components of DCLL coupled with electric field.

The experiment was performed at a room temperature of 25 ± 5℃ and humidity of 70 ± 5 %. Figure 6.1 depicts the experimental setup for the deposition of PVDF micro-threads by DCLL coupled with electrostatic field (EF). The DCLL has been discussed elaborately elsewhere.[47] In summary, An one-sided ITO-coated PET substrate, having a width of 1 cm, length of 2 cm and thickness of 0.17 mm, was fixed on a thermoelectric Peltier heater (Peltier-12706), keeping the ITO-coated surface facing down to the Peltier heater. The setup was positioned on a small goniometer which was placed above a customized unidirectional movable motorized stage (Holmarc motorized X-stage (servo motor) (Model no.: MTSzz-90115-RE25-01)). An electrically conductive stainless-steel blade was placed vertically right above the PET surface by keeping a narrow gap of $\sim 60 \pm 5$ μm between the blade and the PET substrate. The positive and negative terminals of a DC voltage supply were attached to the blade and to the ITO-coated side of the PET substrate, respectively (Figure 6.1), so that the applied potential can be controlled from $0 - 1000$ V. The bare side of the PET substrate was kept upside all along so that the PET substrate itself acts as the insulator to prevent short circuits while applying electric field. A 20 μl drop of the PVDF/DMF solution-2 was dispensed to the gap between the blade and the substrate, and the stage was driven at a constant velocity of 40 μm s^{-1}. The solution formed a curved meniscus and was held at the gap between the blade and the substrate due to the capillary force. As the stage moved, the contact line moved in the opposite direction relative to the substrate with an average speed the same as that of the stage. As the average speed of the contact line is equivalent to that of the stage velocity, hereafter stage velocity will be considered as contact line speed. As the contact line moved, the PVDF micro-threads started depositing from the receding side of the driven contact line. A Peltier heater was used to maintain the substrate temperature at 75℃ as the DMF has a high boiling point of ~ 153℃.[58] Substrate temperature of 75℃ induced rapid evaporation without any active boiling. The vapor pressure of DMF at room temperature (25℃) is 0.481 kPa, which is

increased upto 7.67 kPa[59] by increasing the substrate temperature upto 75℃. It was found that at the DMF vapor pressure of 7.67 kPa, and the stage velocity of 40 μm s^{-1}, the PVDF forms a continuous and relatively straight micro-thread on the PET substrate. A PVDF micro-thread without any discontinuity is very important for any efficient application of the piezoelectric device. Dimethyl sulfoxide (DMSO) is also a good solvent for PVDF but, due to its low volatility (boiling point, ~ 189℃),[60] a PVDF thin film rather than the micro-threads was deposited using DCLL. Other well-known solvents include hexamethyl phosphoramide, n-methyl-2-pyrrolidone, tetramethylurea, triethyl phosphate, trimethyl phosphate etc., but due to their relatively high boiling points, they are not suitable for the micro-thread fabrication using EF-coupled DCLL.

6.2.3 PVDF Thin Film Fabrication

A thin film of PVDF was spun coat on (2 X 2) cm^2 pieces of glass with solution-1 using a spin coater (model: spin speed: 1000 rpm, spin duration: 60 sec). The thickness of the PVDF film (~226 nm) was measured using ellipsometry (model: Nanofilm_ep3sw, Make: Accurion GmbH, Germany).

6.2.4 PVDF Nano Fiber Fabrication

PVDF nanofibers were prepared from a solution of PVDF/DMF using an electrospinning device (model: E-spin, Super ES-2 model, Make: Nanotech, India) at an applied voltage of 19 kV Average diameter of the nanofibers was ~180 nm.

6.2.5 Characterization

A light reflected-microscopy (Axio Scope.A1 MAT HAL 100) was used to capture bright field images of the deposited micro-thread on the PET sheet from DCLL coupled with EF. Field emission scanning electron microscopy (FESEM) (model: JSM-7610F, Make:

Jeol, Japan) and AFM were used to capture the topographical details of the deposited micro-threads. A high-speed camera (Phantom VEO-E 340L, U.S.) was used to investigate the deposition process at a speed of 500 fps.

Thin film PVDF samples and nanofibrous PVDF samples were further characterized by Fourier transform infrared spectroscopy (FTIR) (Model No.: IRAffinity-1; Make: M/s Shimadzu, Japan**)** and Raman spectroscopy (Horiba Jobin Vyon, LabRam HR, Japan).

The deposited micro-threads on the PET substrate were not characterized by Raman spectroscopy and FTIR due to the similar peak position of PVDF and PET.[61–64] A similar experiment was performed on a micro cover-glass (axiva, 18×18 mm, and thickness of 0.13 to 0.16 mm) by depositing aluminum (thickness of ~ 100 nm) to one side of the cover-glass by thermal evaporator (HHV, India; Model: Lab Coater Auto 500). This makes one side of the cover glass electrically conductive, and thus, on the non-conductive side, PVDF micro-threads were deposited using EF-coupled DCLL. After depositing the PVDF micro-threads, the sample was characterized using Raman spectroscopy. FTIR was not sensitive enough to provide a good signal of the deposited PVDF micro-threads on the cover glass.

6.3 Results and Discussion

Following the EF-coupled DCLL (as described in the experimental section), from solution-2, PVDF micro-threads were deposited on the bare side of the PET. Figure 6.2 shows the optical images of the deposited PVDF micro-threads at the different applied electric fields. The width of the micro-threads was found to increase with the increasing electric field and reach the maximum width of ~ 40 µm at ~ 7 V μm^{-1} (500 V). Irregularities were observed at the edges of the micro-threads at the low applied electric field, but the same became more prominent and flawless when more than ~ 7 V μm^{-1} (500 V) was applied (Figure 6.2 (d), (e), and (f)). With the applied electric field of higher than ~ 7 V μm^{-1} (500 V), the width of the

micro-threads gradually decreased and then became almost constant to ~ 20 µm at an electric field of $\sim 13\ V\ \mu m^{-1}$ (900 V) or higher. Based on these observations, for the ease of the subsequent discussion, we divide the range of the electric field applications into two regimes: Zone-I, which corresponds to the low electric field zone or development zone (electric field range $\sim 0\ V\ \mu m^{-1}$(0 V) to $\sim 7\ V\ \mu m^{-1}$ (500 V)), and Zone-II, that corresponds to the high electric field zone or relatively steady fully developed zone (electric field range $\sim 7\ V\ \mu m^{-1}$ (500 V) to $\sim 14\ V\ \mu m^{-1}$ (1000 V)). In zone-I, first, a thin liquid film of the PVDF solution was developed in between two subsequently deposited micro-threads. This thin film eventually dewetted to form micro/nanoholes. The holes then merged to form labyrinths of ribbon-like structures, and these ribbons eventually disintegrate into micro/nanodroplets due to Rayleigh-Plateau instability.[65,66] Dewetted droplets and holes are visible on the PET substrates in between two micro-threads in Figures 6.2 (a), (b), and (c).

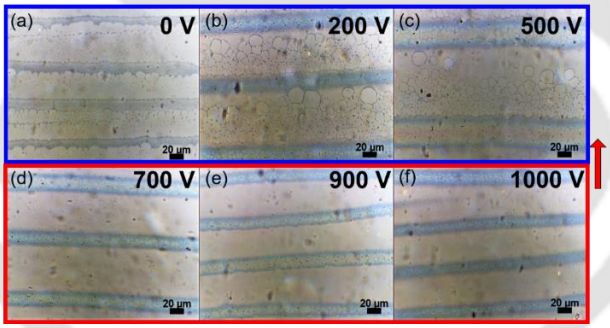

Figure 6.2. Optical microscopy images of deposited micro-threads of PVDF from DMF, on a glass substrate during EF-coupled DCLL, at an applying voltage of (a) 0 V, (b) 200 V, (c) 500 V, that corresponds to zone-I (blue box) and (d) 700 V, (e) 900 V and (f) 1000 V corresponds to zone-II (pink box). The substrate temperature is maintained at 75℃ during DCLL. The red arrow at the right side, corresponds to the direction of contact line movement. All scalebars represent as 20 µm.

At zone-II of the higher electric field, no thin film dewetted structure was noticed in the optical images (Figure 6.2 (d), (e), and (f)). However, close observation revealed the labyrinth-like structures on the micro-threads themselves. For a better understanding of the topography of the polymer deposited samples, FESEM and AFM characterizations were performed, and

typical images at applied electric field of $\sim 0\ \mathrm{V\ \mu m^{-1}}$ (0 V), $\sim 7\ \mathrm{V\ \mu m^{-1}}$ (500 V), and $\sim 14\ \mathrm{V\ \mu m^{-1}}$ (1000 V) are shown in Figure 6.3. Both the FESEM and AFM confirm the presence of labyrinth-like micro-cracks in all the micro-threads, and the depth of the micro-cracks are maximum (25 nm) at 500 V. These cracks were generated during the evaporation of the solvents from the deposited polymer matrix. Figure 6.3 (b), (e), also confirms the labyrinth-like dewetted polymeric structures in between the micro-threads at low applied electric field. However, at zone-II, nano-scale PVDF droplets were also observed in between two adjacent micro-threads on the PET substrate, which suggested the presence of precursor polymer film thinner than that observed at low applied electric field. This is plausibly due to the effect of fast electrodewetting at a high electric field, which renders the substrate with frequent depositions (as the periodicity or the length scale of the deposition decreases), leaving behind the very thin precursor film that dewetted later to nanoscale droplets. Irrespective of the electric field applications, nanoscale features were observed on the micro-threads in all the cases (Figure 6.3).

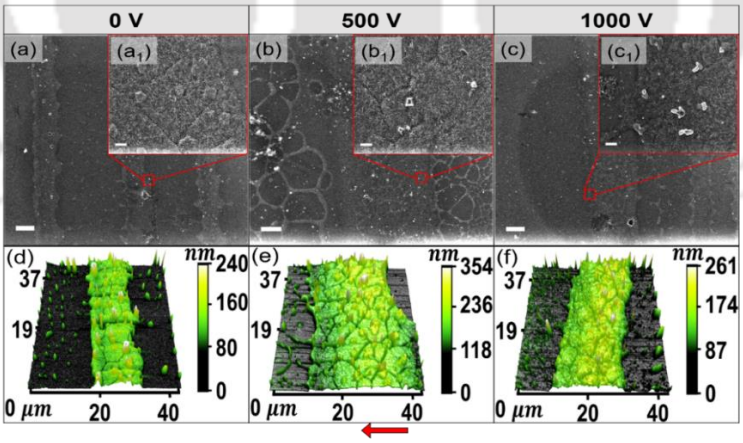

Figure 6.3. FeSEM images of deposited micro-threads of PVDF from DMF during contact line movement at an applying voltage of (a) 0 V, (b) 500 V and (c) 1000 V. Magnified FeSEM images of the respective samples are depicted in the inset images (a_1, b_1, and c_1). Scalebars of the primary images (a), (b), and (c) corresponds to 10 μm and that of the inset images represent 1 μm, respectively. Corresponding AFM images are shown in the Figures (d), (e), and (f) for the applied voltage of 0 V, 500 V, and 1000 V respectively. The red arrow corresponds to the direction of contact line movement. The red arrow at bottom corresponds to the direction of contact line movement.

In the current study, the deposition process is a bit different compared to the earlier study.[47] Despite having a similar contact angle, ~ 77°, of DMF on PET substrate as toluene exhibits on Si substrate (from the earlier study), the liquid meniscus of DMF does not really follow the way toluene meniscus follows during micro-thread deposition.

Figure 6.4 shows the time evolution of the deposition process without any applied electric field. The sequences are captured from a high-speed video. These sequences clearly evinced that after pinning to a site (Figure 6.4, 0.53 s), at first, film formation took place (Figure 6.4, 0.69 s). This liquid thin film underwent solvent evaporation (due to the high temperature of 75 °C maintained by a thermal stage), and started dewetting at the relatively thinner film sites (Figure 6.4, 0.79 s). This dewetting then led to the formation of the new micro-thread (Figure 6.4, 0.9 s). After that, both the micro-thread and the thin film retracted, leaving behind lots of dewetted nano-structures (Figure 6.4, 1.16 s) on the PET substrate and the micro-threads with irregular edges having protruded polymeric fingers. On the contrary, as the electric field was applied, the electrodewetting was rather smooth and generated micro-threads with relatively smooth edges without prominent fingers. The video revealed that slightly thick (width ~ 40 μm) and undulated micro-threads were generated while 500 V was applied. In contrast, relatively straight and thinner micro-threads (width ~ 20 μm) were developed at a high electric potential of 1000 V. Generation of electric field lines between the vertical blade edge and the ITO (coated at the back side of the PET), restrict the formation of liquid polymeric fingers and smooth edge of the micro-threads were obtained.

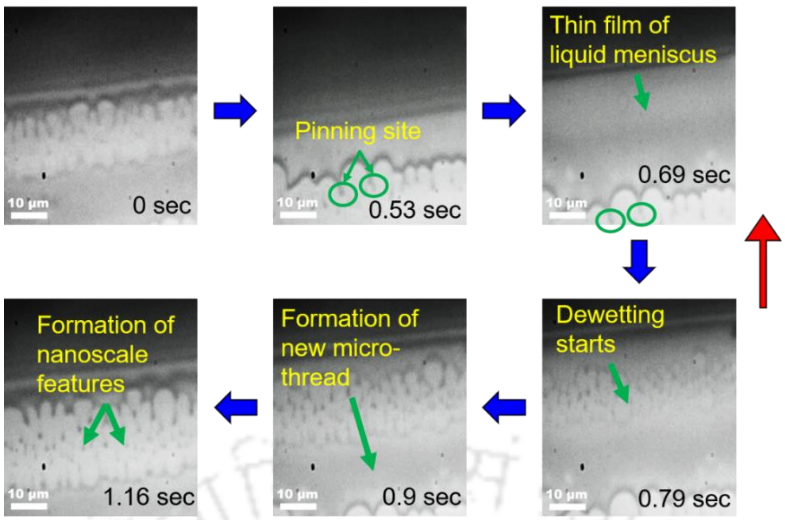

Figure 6.4. Time evolution of the dewetted structure of PVDF during DCLL at 0 V is shown in these optical images. DCLL was performed from the PVDF/DMF solution with concentration of $1\ \mathrm{mg\ ml^{-1}}$ and at a contact line speed of $40\ \mu\mathrm{m\ s^{-1}}$. The blue arrow represents the sequence of the deposition phenomena and the red arrow at the right side corresponds to the direction of contact line. All scalebars represent as 10 µm.

Figure 6.5 represents the FTIR spectrum of PVDF thermally annealed and electro-spun fiber samples. In the case of thermally annealed samples, the lower temperature shows more β and γ crystalline phases compared to higher annealing temperatures, which is reported earlier also.[67,68] It is noticed that the solitary peaks for α-phase, $763, 795, 854, 975, 1149, 1209$ and $1383\ \mathrm{cm^{-1}}$, are clearly distinguished with higher intensities in case of spin-coated sample annealed at 130℃ (S-130℃). At 110℃ (S-110℃), the intensities of earlier mentioned peaks for α-phase gradually decrease and, subsequently, they are significantly less detected at lower annealing temperatures like $70, 90$℃ (S-70℃ and S-90℃). Instead, a mixture of β- and γ-phases is seen in significant amount. The peculiar characteristic peaks responsible for β-phase are 1275 and $1431\ \mathrm{cm^{-1}}$[64,69] and the characteristic peaks for γ-phase, are 811 and $1234\ \mathrm{cm^{-1}}$,[64,69] and both crystallinities are noticed at both lower annealing temperatures, $70, 90$℃. Electro-spun fiber shows an incredible amount of β-phase with peak intensities at 1275 and $1431\ \mathrm{cm^{-1}}$. A small hump is also present at $1234\ \mathrm{cm^{-1}}$, which indicates the

presence of a small amount of γ-phase. If we look closely at Figure 6.5 (b), the sample S-70℃ shows more γ-phase than sample S-90℃ as the peak at around 840 cm^{-1} has shifted to 837 cm^{-1}. Sample S-110℃ also indicates the presence of some amount of β-phase, as there are humps at around 839, 1275 and 1431 cm^{-1}, but at around 763, 795 and 975 cm^{-1}, some prominent peaks of α-phase are also present. On the other side, electro-spun sample clearly indicates the β-phase at around 840, 1275 and 1431 cm^{-1}.

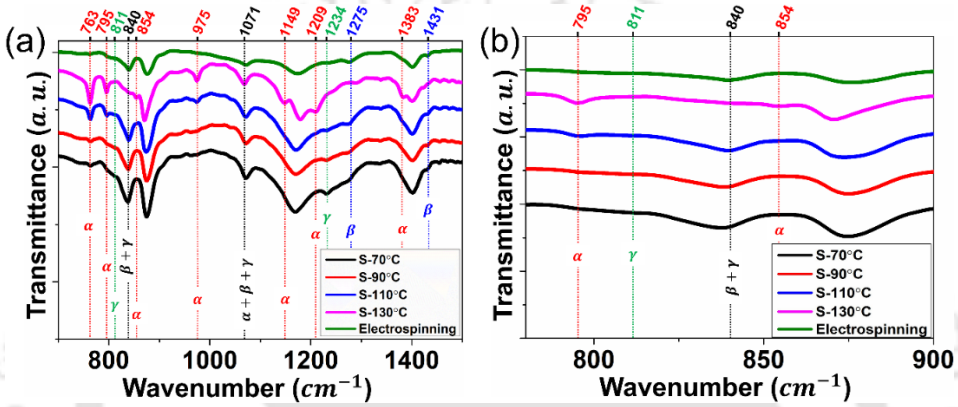

Figure 6.5. (a) FTIR spectrum in transmittance mode of PVDF thin film annealed at 70℃ (S-70℃, black), 90℃ (S-90℃, red), 110℃ (S-110℃, blue) and 130℃ (S-130℃, magenta); and also, of electro spun fiber of PVDF (electrospinning, olive) at 19 kV. (b) A short wavelength scale of the same FTIR spectrum of same samples.

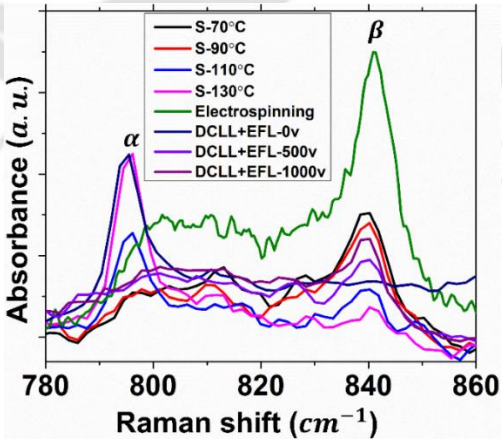

Figure 6.6. Raman spectrum of PVDF thin film annealed at 70℃ (S-70℃, black), 90℃ (S-90℃, red), 110℃ (S-110℃, blue) and 130℃ (S-130℃, magenta); and also, of electro spun fiber of PVDF (electrospinning, olive) at 19 kV, deposited PVDF micro-threads at a applying voltage of 0 V (DCLL+EFL-0 V, navy blue), 500 V (DCLL+EFL-500 V, violet) and 1000 V (DCLL+EFL-1000 V, purple).

In the focus of the Raman spectrum, the samples are characterized by a laser, wavelength of 532 nm (class 3B), at operating condition of 600 grating and 25 % allowance of the laser. There are some characteristic peaks, associated with the particular crystallinity of PVDF in the Raman spectrum. Figure 6.6 depicts similar observations as FTIR exhibits (Figure 6.5) for fabricated samples from spin-coater and electrospinning. The annealing temperatures, 70℃ and 90℃, show more prone towards β-phase (840 cm^{-1}),[6,31,33,36,68] unlike 110℃ and 130℃, which are in favour of α-phase (790 cm^{-1}) mostly.[6,31,33,36,68] The film from electro-spun nano-fiber shows a strong peak at around 840 cm^{-1}, representing the β-phase crystalline structure of PVDF. Interestingly, micro-threads of PVDF from DCLL coupled with EF also show an excellent result at operating electric field of ~ 7 V μm^{-1} (500 V) and ~ 14 V μm^{-1} (1000 V). Deposited micro-threads exhibit a suitable peak at around 840 cm^{-1} at both operating electric fields; this is a clear indication of more β-phase crystalline structure of PVDF. On the other hand, without EF, at ~ 0 V μm^{-1} (0 V), exhibits a strong peak at around 790 cm^{-1}, which indicates the presence of α-phase in rich amount.

Table 6.1. phase ratio of β- and α- of prepared samples of PVDF from thermal annealing, electrospinning and DCLL coupled with EFL

Sample	(β/α)
S-70℃	3.41
S-90℃	2.85
S-110℃	0.50
S-130℃	0.18
Electrospinning	4.21
DCLL+EFL-0 V	0.32
DCLL+EFL-500 V	1.65
DCLL+EFL-1000 V	1.92

$$\frac{\beta}{\alpha} = \frac{Raman\ shift\ at\ 840\ cm^{-1}}{Raman\ shift\ at\ 790\ cm^{-1}} \quad \ldots \quad \ldots \quad \ldots \quad \ldots \quad \ldots (6.1)$$

The ratios of β- and α-phases (equation 6.1) of respective samples are presented in table 1 and are calculated from the absorbencies at respective Raman shifts, 840 cm^{-1} (for β-phase) and 790 cm^{-1} (for α-phase). It is observed that the higher operating voltage, 1000 V, shows a significant amount of β-phase, almost double to the α-phase. This value might be progressed with a minimal increment of the magnitude of electric potential than the present case. The maximum electric field intensity used here is 14 V/μm when 1000 V is applied across the two terminals. So, there is less chance of dielectric breakdown of PVDF film during the experiment, as the dielectric strength of PVDF (MW- 180,000) is 412 MV/m.[70] The electro-spun fiber shows 4.2 times more β-phase than α-phase when applied voltage is 19 kV, much higher than the used voltage in DCLL coupled with EF.

6.3.1 Energy Harvesting by Applying Mechanical Stress

The piezoelectric property is demonstrated by applying a pressure across the sample with a gentle touch of a finger. A PET substrate containing deposited PVDF micro-threads from a moving contact line of PVDF-DMF solution while a 500 V is applied, is used as a test sample.

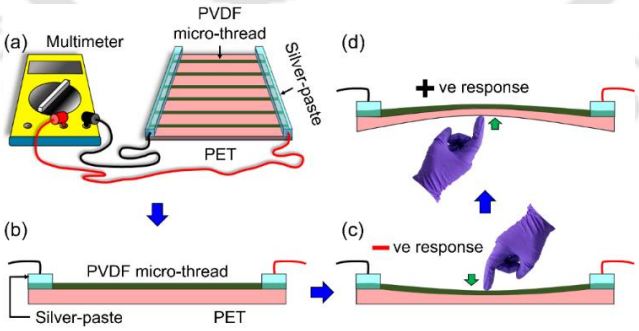

Figure 6.7. The schematics depict as (a) the setup and its accessories for energy harvesting experiment, (b) the side view of the arrangement where, PVDF micro-thread (dark green colored) is deposited on PET substrate (rose colored) and a silver-paste (light blue colored) is applied on PVDF micro-threads, (d) applied stress as a form of a gentle touch of a finger to the back side of the PET sheet and, (c) on the PVDF micro-threads.

Figure 6.7 (a) depicts the experimental setup, and its accessories for the stress applied energy harvesting experiment. At first, the micro-threads were connected to each other on the both sides of the edges by using silver conductive paste (Silverpase-001, techinstro, India).

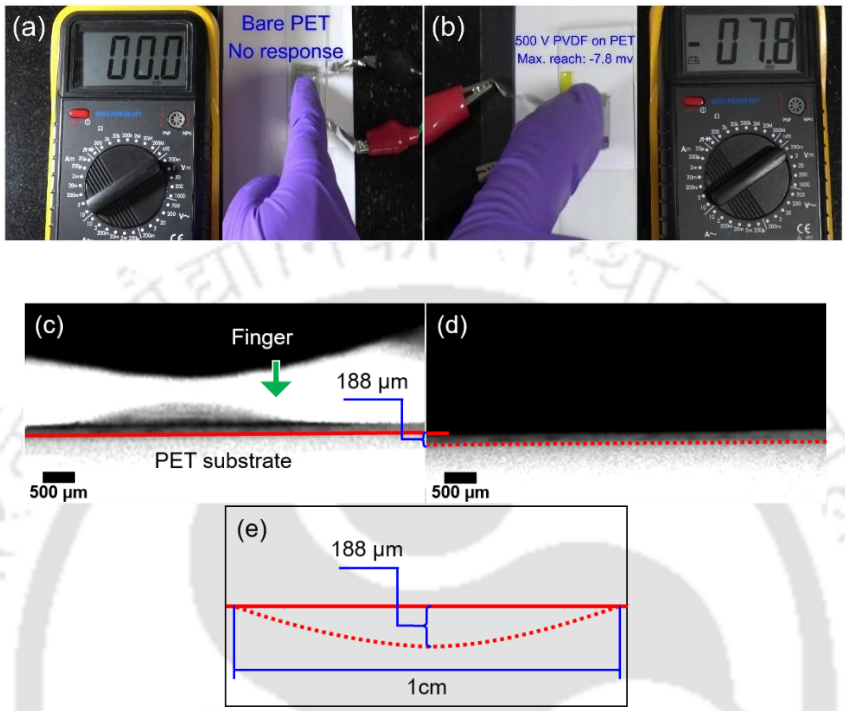

Figure 6.8. (a) A 0 V DC response against a gentle pressing on bare PET (no deposited micro-threads of PVDF on PET sheet). (b) A maximum DC voltage response of -7.8 V against a gentle pressing on PVDF micro-threads, deposited while applying voltage is 500 V. The deflection of PET sheet, (c) before and (d) after applying pressure by finger is ~ 188 µm. A (e) schematic diagram is also depicted for better understanding. The scalebars of (c) and (d) is represented as 500 µm.

These two edges, coated with silver conductive paste, acted as electrodes (Figure 6.7 (b)), which were connected to a digital multimeter (Mastech M92A(H)) for sensing the magnitude of output DC voltage against an applied mechanical stress (Figure 6.7 (d), (c)). The whole sample was firmly attached to a rigid surface for less disturbances. Here, two samples were prepared, where first sample contained a bare PET substrate without any deposited micro-thread (Figure 6.8 (a)) Another sample consisted with deposited micro-threads on the PET substrate, where deposition was done under a ~ 7 V µm^{-1} (500 V) electric field (Figure 6.9

(b)). The first sample (setup-1) responded a zero magnitude of output DC voltage against a gentle touch, where another sample (setup-2), poled under ~ 7 V μm^{-1} (500 V) electrical field, showed a comparatively good response to the output DC voltage upto − 7.8 mV against applied stress. A positive response of 0.6 mV was also recorded when the same sample was pressed gently to the back side of the PVDF micro-threads deposited region. The deflection of PET sheet by applying finger stress on it was also measured, and that was ~ 188 µm (Figure 6.8 (c), (d) and (e)).

6.3.2 Energy Harvesting: Hitting by A Falling Water Drop

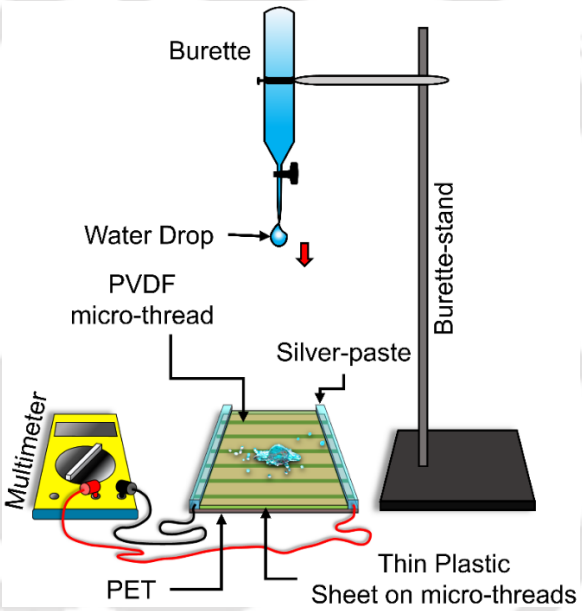

Figure 6.9. The schematic depicts the experimental setup and its accessories of energy harvesting from a PVDF micro-threads deposited PET sheet, when a stress is applied by a form of a hitting water drop.

The prepared device is also capable of harvesting energy from falling water drops (such as raindrops). Figure 6.9 shows the schematic of an experimental setup, where the device is connected to a multimeter and a water drop, diameter of ~ 0.7 mm, is dispensed from the top keeping a certain distance, ~ 50 cm. The water drop was allowed to fall and hit the surface of the PVDF micro-threads every 10 sec interval. Here, it should be noted that the water drop does not hit the surface of the PVDF micro-threads directly as these are covered by a thin layer

of PS wrapper. Once the experiment started, we noted ten readings of the output voltage magnitude after every 10 sec interval, and Figure 6.10 depicts the same. For every water drop hitting the device shows some output voltage. A maximum voltage of -3 mV is recorded from the drop-hitting experiment. We also observe a reduced output voltage at the 6th time (Figure 6.10), and again it reaches to its maximum (-3 mV) at the 9th time.

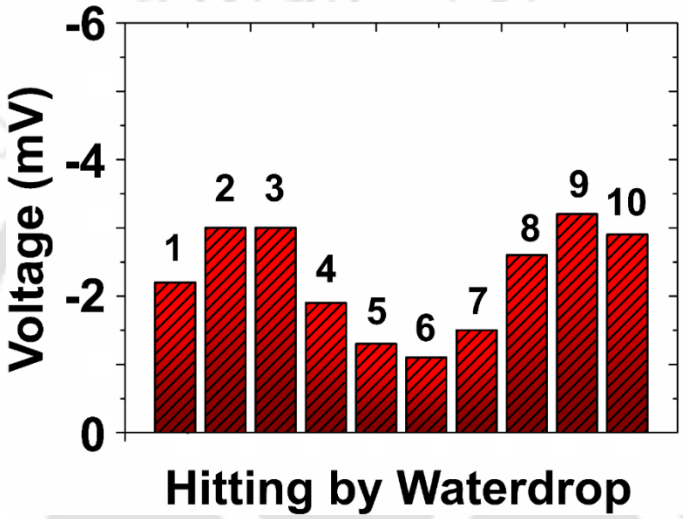

Figure 6.10. represents the output voltages by every waterdrop hitting. Ten readings are recorded and each reading is taken in every 10 sec interval when waterdrop hits.

6.4 Conclusions

We have successfully fabricated PVDF micro-threads by dynamic contact line lithography. Here, the deposited results state that the volatility of the solvent is the key factor for fabricating proper line patterns during contact line movement.[47] The effect of applying electric field on the phase transformation of PVDF is also investigated, and it is found that at a comparatively very low applied electric field than the conventional electrical poling or electrospinning method, a good amount of β-phase is achievable. It is important to notice that the gap distance between stainless-steel blade and PET substrate, plays an important role regarding intensity of the electric field. Also, it should be noted that, the effect of polarity of

solvent is not investigated while the electric field is applied. Therefore, deposition from higher polar solvent like DMSO (dielectric constant of 47.29 at 25℃),[71] instead of DMF (dielectric constant of 37.51 at 25℃),[72] might deposits PVDF micro-threads, consisting of more significant amount of β-phase. The minimum treated electric field in preparation of a sample that we have shown here for piezoelectric effect is $\sim 7\ \mathrm{V\ \mu m^{-1}}$ (500 V), and that has fairly responded against a given mechanical stress. We believe the sample poled under $\sim 2.8\ \mathrm{V\ \mu m^{-1}}$ (200 V) electric field, is also capable of showing some piezoelectric behaviour, and this is much lower than the conventional method. We also believe that these fabricated micro-threads are qualified for acting as an individual fiber in various fields like sensing, energy harvesting and, nano generators etc.

References

[1] D.-W. Fu, H.-L. Cai, Y. Liu, Q. Ye, W. Zhang, Y. Zhang, X.-Y. Chen, G. Giovannetti, M. Capone, J. Li, R.-G. Xiong, *Science* **2013**, *339*, 425.

[2] S. C. Mathur, J. I. Scheinbeim, B. A. Newman, *J. Appl. Phys.* **1984**, *56*, 2419.

[3] S. Horiuchi, Y. Tokunaga, G. Giovannetti, S. Picozzi, H. Itoh, R. Shimano, R. Kumai, Y. Tokura, *Nature* **2010**, *463*, 789.

[4] P. Muralt, *IEEE Trans. Ultrason. Ferroelectr. Freq. Control* **2000**, *47*, 903.

[5] K.-I. Park, C. K. Jeong, J. Ryu, G.-T. Hwang, K. J. Lee, *Adv. Energy Mater.* **2013**, *3*, 1539.

[6] K.-I. Park, S. Bin Bae, S. H. Yang, H. I. Lee, K. Lee, S. J. Lee, *Nanoscale* **2014**, *6*, 8962.

[7] H. J. Oh, D.-K. Kim, Y. C. Choi, S.-J. Lim, J. B. Jeong, J. H. Ko, W.-G. Hahm, S.-W. Kim, Y. Lee, H. Kim, B. J. Yeang, *Sci. Rep.* **2020**, *10*, 16339.

[8] S. Jiansirisomboon, K. Songsiri, A. Watcharapasorn, T. Tunkasiri, *Curr. Appl. Phys.* **2006**, *6*, 299.

[9] P. Martins, A. C. Lopes, S. Lanceros-Mendez, *Prog. Polym. Sci.* **2014**, *39*, 683.

[10] T. R. Shrout, S. J. Zhang, *J. Electroceramics* **2007**, *19*, 113.

[11] T. Aihara, H. Saito, T. Inoue, H.-P. Wolff, B. Stühn, *Polymer (Guildf).* **1998**, *39*, 129.

[12] P. K. Szewczyk, A. Gradys, S. K. Kim, L. Persano, M. Marzec, A. Kryshtal, T. Busolo, A. Toncelli, D. Pisignano, A. Bernasik, S. Kar-Narayan, P. Sajkiewicz, U. Stachewicz, *ACS Appl. Mater. Interfaces* **2020**, *12*, 13575.

[13] F. A. Sheikh, T. Cantu, J. Macossay, H. Kim, *Sci. Adv. Mater.* **2011**, *3*, 216.

[14] S. Mansouri, T. F. Sheikholeslami, A. Behzadmehr, *J. Mater. Res. Technol.* **2019**, *8*, 1608.

[15] J. Granstrom, J. Feenstra, H. A. Sodano, K. Farinholt, *Smart Mater. Struct.* **2007**, *16*, 1810.

[16] G. Ico, A. Showalter, W. Bosze, S. C. Gott, B. S. Kim, M. P. Rao, N. V. Myung, J. Nam, *J. Mater. Chem. A* **2016**, *4*, 2293.

[17] J. Li, C. Zhao, K. Xia, X. Liu, D. Li, J. Han, *Appl. Surf. Sci.* **2019**, *463*, 626.

[18] H. Parangusan, D. Ponnamma, M. A. A. Al-Maadeed, *Sci. Rep.* **2018**, *8*, 754.

[19] A. V. Shirinov, W. K. Schomburg, *Sensors Actuators A Phys.* **2008**, *142*, 48.

[20] C. Lang, J. Fang, H. Shao, X. Ding, T. Lin, *Nat. Commun.* **2016**, *7*, 11108.

[21] M. Li, P. Bidez, E. Guterman-Tretter, Y. Guo, A. G. MacDiarmid, P. I. Lelkes, X. Yuan, X. Yuan, J. Sheng, H. Li, C. Song, Y. Wei, *Chinese J. Polym. Sci.* **2007**, *25*, 331.

[22] T. Yamada, Y. Hayamizu, Y. Yamamoto, Y. Yomogida, A. Izadi-Najafabadi, D. N.

Futaba, K. Hata, *Nat. Nanotechnol.* **2011**, *6*, 296.

[23] L. Persano, C. Dagdeviren, Y. Su, Y. Zhang, S. Girardo, D. Pisignano, Y. Huang, J. A. Rogers, *Nat. Commun.* **2013**, *4*, 1633.

[24] R. Schulze, T. Gessner, M. Heinrich, M. Schueller, R. Forke, D. Billep, M. Sborikas, M. Wegener, in *Proc. ISAF-ECAPD-PFM 2012*, IEEE, **2012**, pp. 1–4.

[25] A. J. Lovinger, *Macromolecules* **1982**, *15*, 40.

[26] J.-C. Dubois, *Adv. Mater.* **1996**, *8*, 542.

[27] T. Lei, P. Zhu, X. Cai, L. Yang, F. Yang, *Appl. Phys. A* **2015**, *120*, 5.

[28] M. Li, H. J. Wondergem, M.-J. Spijkman, K. Asadi, I. Katsouras, P. W. M. Blom, D. M. de Leeuw, *Nat. Mater.* **2013**, *12*, 433.

[29] J. Li, Q. Meng, W. Li, Z. Zhang, *J. Appl. Polym. Sci.* **2011**, *122*, 1659.

[30] R. P. Ummer, R. B, C. Thevenot, D. Rouxel, S. Thomas, N. Kalarikkal, *RSC Adv.* **2016**, *6*, 28069.

[31] T. Huang, S. Yang, P. He, J. Sun, S. Zhang, D. Li, Y. Meng, J. Zhou, H. Tang, J. Liang, G. Ding, X. Xie, *ACS Appl. Mater. Interfaces* **2018**, *10*, 30732.

[32] A. De Neef, C. Samuel, H. Amorín, G. Stoclet, R. Jiménez, P. Dubois, J. Soulestin, J.-M. Raquez, *ACS Appl. Polym. Mater.* **2020**, *2*, 3766.

[33] P. Thakur, A. Kool, B. Bagchi, N. A. Hoque, S. Das, P. Nandy, *Phys. Chem. Chem. Phys.* **2015**, *17*, 13082.

[34] S. Jana, S. Garain, S. Sen, D. Mandal, *Phys. Chem. Chem. Phys.* **2015**, *17*, 17429.

[35] A. Sengupta, S. Das, S. Dasgupta, P. Sengupta, P. Datta, *ACS Biomater. Sci. Eng.* **2021**, *7*, 1673.

[36] A. Arrigoni, L. Brambilla, C. Bertarelli, G. Serra, M. Tommasini, C. Castiglioni, *RSC Adv.* **2020**, *10*, 37779.

[37] D. Wu, S. Huang, Z. Xu, Z. Xiao, C. Shi, J. Zhao, R. Zhu, D. Sun, L. Lin, *J. Phys. D. Appl. Phys.* **2015**, *48*, 285305.

[38] N. Chanunpanich, B. Lee, H. Byun, *Macromol. Res.* **2008**, *16*, 212.

[39] A. K. An, J. Guo, E.-J. Lee, S. Jeong, Y. Zhao, Z. Wang, T. Leiknes, *J. Memb. Sci.* **2017**, *525*, 57.

[40] Z. Yin, B. Tian, Q. Zhu, C. Duan, *Polymers (Basel).* **2019**, *11*, 2033.

[41] P.-H. Ducrot, I. Dufour, C. Ayela, *Sci. Rep.* **2016**, *6*, 19426.

[42] N. Meng, X. Zhu, R. Mao, M. J. Reece, E. Bilotti, *J. Mater. Chem. C* **2017**, *5*, 3296.

[43] S. Gonçalves, J. Serrado-Nunes, J. Oliveira, N. Pereira, L. Hilliou, C. M. Costa, S. Lanceros-Méndez, *ACS Appl. Electron. Mater.* **2019**, *1*, 1678.

[44] W. R. Lindemann, R. L. Philiph, D. W. W. Chan, C. T. Ayers, E. M. Perez, S. P. Beckman, J. Strzalka, S. Chaudhary, D. Vaknin, *Phys. Chem. Chem. Phys.* **2015**, *17*, 29335.

[45] P. Roy, R. Mukherjee, D. Bandyopadhyay, P. S. Gooh Pattader, *Nanoscale* **2019**, *11*, 16523.

[46] K. Murmu, A. Pandey, P. Roy, A. Deb, P. S. Gooh Pattader, *J. Appl. Polym. Sci.* **2022**, *139*, 1.

[47] K. Murmu, K. P. Burgula, P. S. Gooh Pattader, *J. Colloid Interface Sci.* **2021**, *601*, 156.

[48] M. Kim, S. Lee, Y. Kim, *APL Mater.* **2020**, *8*, 071109.

[49] D. Mao, B. E., M. A., in *Ferroelectr. - Phys. Eff.*, InTech, **2011**.

[50] H. S. Nalwa, in *Wildsafe BC* (Ed: H.S. Nalwa), CRC Press, Boca Raton, **1995**, p. 120.

[51] T. Furukawa, *Phase Transitions* **1989**, *18*, 143.

[52] W. Xia, Z. Zhang, *IET Nanodielectrics* **2018**, *1*, 17.

[53] P. Martins, A. C. Lopes, S. Lanceros-Mendez, *Prog. Polym. Sci.* **2014**, *39*, 683.

[54] M. Kanik, O. Aktas, H. S. Sen, E. Durgun, M. Bayindir, *ACS Nano* **2014**, *8*, 9311.

[55] A. Laudari, J. Barron, A. Pickett, S. Guha, *ACS Appl. Mater. Interfaces* **2020**, *12*, 26757.

[56] H. Dvey-Aharon, P. L. Taylor, A. J. Hopfinger, *J. Appl. Phys.* **1980**, *51*, 5184.

[57] G. T. Davis, J. E. McKinney, M. G. Broadhurst, S. C. Roth, *J. Appl. Phys.* **1978**, *49*, 4998.

[58] P. Oxychloride, *Chem. Eng. News Arch.* **1953**, *31*, 2258.

[59] X. Cui, G. Chen, X. Han, *J. Chem. Eng. Data* **2006**, *51*, 1860.

[60] H. Ding, Y. Gao, J. Li, J. Qi, H. Zhou, S. Liu, X. Han, *J. Chem. Eng. Data* **2016**, *61*, 3013.

[61] V. F. Alexiou, G. N. Mathioudakis, K. S. Andrikopoulos, A. Soto Beobide, G. A. Voyiatzis, *Polymers (Basel).* **2020**, *12*, 2626.

[62] A. P. dos S. Pereira, M. H. P. da Silva, É. P. Lima Júnior, A. dos S. Paula, F. J. Tommasini, *Mater. Res.* **2017**, *20*, 411.

[63] S. Paszkiewicz, A. Szymczyk, D. Pawlikowska, I. Irska, I. Taraghi, R. Pilawka, J. Gu, X. Li, Y. Tu, E. Piesowicz, *RSC Adv.* **2017**, *7*, 41745.

[64] X. Cai, T. Lei, D. Sun, L. Lin, *RSC Adv.* **2017**, *7*, 15382.

[65] A. Sharma, G. Reiter, *J. Colloid Interface Sci.* **1996**, *178*, 383.

[66] R. Khanna, A. Sharma, G. Reiter, *EPJ direct* **2000**, *2*, 1.

[67] M. Satthiyaraju, T. Ramesh, *Mater. Res. Express* **2019**, *6*, 105366.

[68] S. Satapathy, P. K. Gupta, S. Pawar, K. B. R. Varma, **2008**.

[69] E. Kabir, M. Khatun, L. Nasrin, M. J. Raihan, M. Rahman, *J. Phys. D. Appl. Phys.* **2017**, *50*, 163002.

[70] B. Fan, Z. Xing, F. Bedoui, J. Yuan, X. Lu, D. He, M. Zhou, C. Zhang, Z. Dang, S.

Weigand, J. Bai, *Polymer (Guildf).* **2020**, *190*, 122235.

[71] Q. Jie, J. Guo-Zhu, *J. Phys. Chem. A* **2013**, *117*, 12983.

[72] F. Corradini, L. Marcheselli, L. Tassi, G. Tosi, *Can. J. Chem.* **1992**, *70*, 2895.

Chapter 7

Summary and Future Scope

This page is left blank intentionally

7.1 Summary

In this thesis we report a frugal technique to fabricate self-assembled micro/nano featured and its plausible applications. Still, many unexplored areas are yet to be discovered to fully understand the physics behind the deposition process in order to control over the self-assembled method. Also, this thesis opens up some new avenues for further research which can lead to scientific and technological advancement in the domain of micro/nano fabrications and its interesting applications. We have discussed a few of such possibilities at the end of this chapter.

In chapter 3, We demonstrate a facile pathway to fabricate polymer micro/nano features on a flat surface by dynamic CL lithography (DCLL). The process is generic and can be used for various surfaces such as glass, Si wafer, etc. with an appropriate combination of polymer/solvent system. Based on the process parameters of concentration and CL velocity, two morphological phase diagrams are presented for two different polymer/solvent systems. The combination of the polymer and solvent has effect on the deposited morphology, but this study can provide the overall hints for the process parameters toward the desired morphology. Certain process features such as gap distance between the blade and substrate, types of blade, and substrate wettability may affect the morphological phase diagram. Tuning of the surface wettability of Si substrate (water contact angle ~15˚) is demonstrated by forming well defined PS and PMMA micro-features on it. The water contact angle of ~ 35° to ~ 98° for PS microstructure and ~ 68° to ~ 86° for PMMA micro-thread deposited on the Si surface is achieved. This vast change in wettability has the potential to serve many industrial and technological requirements. Lastly, we demonstrate the flexibility of the DCLL technique by fabricating complex multi-polymer microstructures by selecting suitable solvents and process parameters from the morphological phase diagram of the polymers presented in this report. This process can be extended further for more polymers with desired morphology such as microdroplets or threads or their combination as per the requirement.

In chapter 4, PS/PMMA blend polymer is used as a deposited material from a common solvent, toluene. Here, we study the effect of different solubilities on deposited morphology of blend polymer. As PS and PMMA have different solubilities in toluene therefore, it is noticed that higher soluble polymer (PS) deposits initially due to the higher local concentration at the contact line. This counterintuitive behavior is because of the solvent flow (along with the more soluble polymer) towards the contact line to replenish the evaporative loss of the solvent. Moreover, this phenomenon helps us in developing the novel and facile pathway to fabricate Janus micro-thread or micro/nanodroplets on a Si / glass substrate without any physico-chemical guidance by DCLL. Tuning of deposited morphologies of PS/PMMA blend polymer system by changing the composition of polymers only, are also reported. The morphologies are mainly Janus structure, random deposited structures or multilayer deposited structures of micro-thread as well as of micro/nanodroplet. Beside these, it is also noticed that the morphology of deposited micro-threads changes from thread to isolated droplets when the PMMA concentration decreases. This simple template-less technique to fabricate Janus polymeric structures, might be important in fabricating dual responsive sensors, flexible displays or patterned micro-reactors, etc.

In chapter 5, another facile method is demonstrated to fabricate complex polymeric structure. Along with the DCLL technique, selective solvent induced dewetting, and thermal dewetting of polymer features are adopted to develop interesting micro/nanostructures. The study comprises with deposition of PS micro-threads over PMMA thin film. Afterwards, selective solvent vapour treatments, common solvent vapour treatment and thermal treatment above glass transition temperatures of both the polymers, are then performed. Interestingly, the common solvent treatment shows core-shell complex structure, where PS remains as a core inside a PMMA shell. Due to the higher affinity towards Si / glass substrate of PMMA, it forms a shell around PS structure. Selective solvent treatment only dewets respective polymers, and,

a selective dewetted region is created as a result. PMMA thin film converts into disintegrated or dewetted droplets very easily, after selective solvent treatment (acetic acid vapour treatment) due to the spinodal dewetting of thin film. The method which is reported here is simple and affordable compare to high end instrument which is not capable of fabricating complex structure easily.

In chapter 6, an energy harvesting device is developed where, the device is a flexible PET sheet on which PVDF micro-threads are deposited in presence of an electrical bias. Dynamic contact line lithography is used here to deposit PVDF micro-threads from a PVDF/DMF solution. The morphological phase diagram from chapter 3 has guided us to deposit proper micro-threads on the PET sheet. Moreover. a low voltage of electrical bias, $\sim 8\ \mathrm{V\ \mu m^{-1}}$ is able to arrange the crystalline phase of PVDF into β- phase from α- phase. In this chapter, we also have witnessed the increment of β- phase content when the magnitude of the electric field has been increased. A Raman spectroscopy is performed to characterize the crystallinity of each samples. Later, the fabricated device is tested as an energy harvester as it produces electrical potential of ~ -7 mV, when a gentle touch of a finger is applied as a form of a stress. We also have demonstrated that it can be used as an energy harvester from the rain drops. An experiment is performed where water drop hits the device from a certain distance above in order to apply a stress, and the device produces electrical potential of ~ -3 mV.

Briefly, this thesis has covered both the domain of scientific findings and its potential application. Along with the scientific findings elaborated above, the thesis also discloses various aspects of research works, which could be extended for future study.

7.2 Future Scope

The work in the present thesis can be extended in the following ways:

- In chapter 3, the variable parameters were velocity of contact line and the concentration of polymer. So, this research can be extended by varying the combination of parameters like various substrates with different concentrated solution or contact line velocities.
- We have demonstrated fabrication process of complex patterning, this can be extended by fabricating 3D complex micro-sculptures of polymer as bio-mimicking structural color by DCLL method.
- More than two polymers also, can be deposited separately to fabricate complex structure by this DCLL method and a morphological study cane be carried out.
- As the DCLL method is generic, therefore, for every polymeric system with respect to solvent, it is possible to generate separate morphological phase diagram, which can guide to fabricate predefined structures.
- We have seen how the blend polymeric system generates Janus micro-threads and micro/nanodroplets, this research can be extended by introducing blend polymeric system of three polymers.
- A solution of two miscible polymer solutions can be used in DCLL method and, a morphological study can be performed after depositing the polymers.
- In DCLL method, functional polymers also can be used to deposit on the solid surface, and this can be applied directly in respective applications.

Appendix - 1

S1: Percentage weight loss of PS and PMMA in toluene

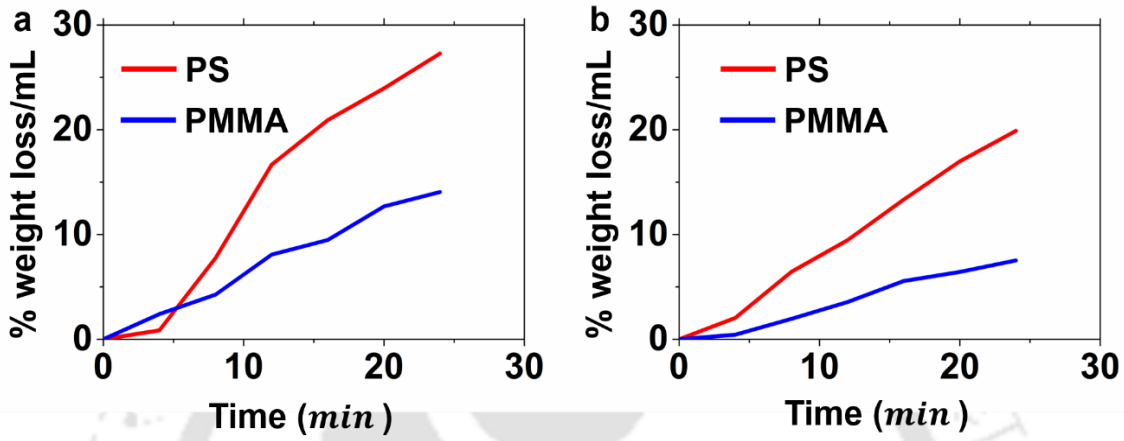

Figure S1: Percentage weight loss of PS and PMMA, per mL of toluene (a) with stirring and (b) without stirring.

At first, a known amount of PS or PMMA pallets of approximately equal size were dipped into 3 ml of toluene in separate beakers. At every 4 min of the interval, the pellets were taken out of the solvent and were dried completely in a vacuum desiccator for 10 min and then measured the weight again. After measurement, the dried pallet was dipped in the same solvent. The percentage of weight loss was then calculated at each step. The dissolution process for individual polymer was performed with stirring at 400 rpm and (b) without stirring.

Publications and Conferences

A1.1 International Publications (From Thesis Work):

1. Kaniska Murmu, Krishna Pradeep Burgula, Partho Sarathi Gooh Pattader, *Dynamic Contact Line Lithography: Template-less Complex Meso-Patterning with Polystyrene and Poly(methyl methacrylate)*, Journal of Colloid and Interface Science 601 (2021) 156–166. https://doi.org/10.1016/j.jcis.2021.05.100

2. Kaniska Murmu, Ankur Pandey, Pritam Roy, Aniruddha Deb, Partho Sarathi Gooh Pattader, *Janus Micro-thread to Micro-nanodroplets Using Dynamic Contact Line Lithography***,** Journal of Applied Polymer Science (2022) 1-11. https://doi.org/10.1002/app.52490

3. Kaniska Murmu, Sunil Kumar Singh, Partho Sarathi Gooh Pattader, *Solvent Assisted Dewetting of PMMA Thin Film and PS Micro-thread: Fabricated by Dynamic Contact Line Lithography*. **(Manuscript under preparation)**

4. Kaniska Murmu, Sunil Kumar Singh, Ankur Pandey, Partho Sarathi Gooh Pattader, *Self-assembled PVDF micro-threads with β-phase crystallinity; induced by dynamic contact line lithography coupled with electric field*. **(Submitted for patent)**

A1.2 International Publications (In Collaboration):

1. Ankur Pandey, **Kaniska Murmu**, Partho Sarathi Gooh Pattader, *Non-equilibrium thermal annealing of a polymer blend in bilayer settings for complex micro/nano-patterning*, RSC Adv. 11 (2021) 10183–10193. https://doi.org/10.1039/d1ra00017a

2. Ankur Pandey, Surjendu Maity, **Kaniska Murmu**, Sagnik Middya, Dipankar Bandyopadhyay, Partho Sarathi Gooh Pattader, *Self-organization of random copolymers to nanopatterns by localized e-beam dosing*, Nanotechnology. 32 (2021) 285302. https://doi.org/10.1088/1361-6528/abf197

7. Sunil Kumar Singh, Aniruddha Deb, **Kaniska Murmu**, Prerona Gogoi, Partho Sarathi Gooh Pattader, *Separation of Anionic and Cationic Surfactant in a Microchannel Using Ultra-Low Electric Field*. **(Manuscript Under Preparation)**

8. Sunil Kumar Singh**, Kaniska Murmu,** Prerona Gogoi, Aniruddha Deb, Tamal Banerjee, Partho Sarathi Gooh Pattader, *Liquid-Liquid Efficient Micro Extraction of Dye in a Microfluidic Platform by creating Electric Field Induced Instability at the Interface of fluids*. (**Manuscript Under Preparation**)

A1.3 Conferences proceeding:

1. Kaniska Murmu, Krishna Pradeep Burgula, Partho Sarathi Gooh Pattader**,** *Phase separation mediated templateless contact line lithography for meso-patterning***,** Proceedings of CUChE Alumni Symposium 2021 On "Diverse Applications of Chemical Engineering", ISBN: 978-81-954649-0-6, 1, 1 (2021) 22-28

A1.4 Conference / Workshop:

1. Kaniska Murmu, Pradeep Krishna, Partho Sarathi Gooh Pattader, Polymer Patterning from Dynamic Contact Lines, International Conference on Functional Materials 2020, IIT KHARAGPUR

2. Kaniska Murmu, Pradeep Krishna, Partho Sarathi Gooh Pattader, Template-less Dynamic Contact Line Lithography, International Coference on Advances in Chemical Engineering (AdChE-2020), UPES DEHRADUN

3. Kaniska Murmu, Partho Sarathi Gooh Pattader, Patterning of Polymer Micro-Threads by Dynamic Contact Line Lithography; Guided by Chemically Patterned Surface, 7th International Conference on Advanced Nanomaterials and Nanotechnology (ICANN2021), IIT GUWAHATI

4. Kaniska Murmu, Pradeep Krishna, Pritam Roy, Prerona Gogoi, Ankur Pandey, Himanshu Raturi, Sunil Kumar Singh, Aniruddha Deb, Partho S. Goohpattader, Patterning and Stochastic Dynamics Laboratory, National Workshop on NEMS/MEMS & Theranostic Devices (NWNTD-2019), IIT GUWAHATI

5. Kaniska Murmu, Deep Eutectic Solvents for Environmental Remediation and Energy Storage, Scheme for Promotion of Academic and Research Collaboration (SPARC-2020)

6. Kaniska Murmu, Recent Advancements in Thermal Analyzers for Materials Characterization, 2020, Gulbarga University